SANDIA REPORT
SAND2005- 7067
Unlimited Release
Printed October 2005

Novel In Situ Mechanical Testers to Enable Integrated Metal Surface Micro-Machines

Sean J. Hearne, Maarten P. de Boer, Paul G. Kotula, Chris W. Dyck, Stephen M. Foiles, David M. Follstaedt, Thomas E. Buchheit

Prepared by
Sandia National Laboratories
Albuquerque, New Mexico 87185 and Livermore, California 94550

Sandia is a multiprogram laboratory operated by Sandia Corporation,
a Lockheed Martin Company, for the United States Department of Energy's
National Nuclear Security Administration under Contract DE-AC04-94AL85000.

Approved for public release; further dissemination unlimited.

Sandia National Laboratories

Issued by Sandia National Laboratories, operated for the United States Department of Energy by Sandia Corporation.

NOTICE: This report was prepared as an account of work sponsored by an agency of the United States Government. Neither the United States Government, nor any agency thereof, nor any of their employees, nor any of their contractors, subcontractors, or their employees, make any warranty, express or implied, or assume any legal liability or responsibility for the accuracy, completeness, or usefulness of any information, apparatus, product, or process disclosed, or represent that its use would not infringe privately owned rights. Reference herein to any specific commercial product, process, or service by trade name, trademark, manufacturer, or otherwise, does not necessarily constitute or imply its endorsement, recommendation, or favoring by the United States Government, any agency thereof, or any of their contractors or subcontractors. The views and opinions expressed herein do not necessarily state or reflect those of the United States Government, any agency thereof, or any of their contractors.

Printed in the United States of America. This report has been reproduced directly from the best available copy.

Available to DOE and DOE contractors from
U.S. Department of Energy
Office of Scientific and Technical Information
P.O. Box 62
Oak Ridge, TN 37831

Telephone: (865) 576-8401
Facsimile: (865) 576-5728
E-Mail: reports@adonis.osti.gov
Online ordering: http://www.osti.gov/bridge

Available to the public from
U.S. Department of Commerce
National Technical Information Service
5285 Port Royal Rd.
Springfield, VA 22161

Telephone: (800) 553-6847
Facsimile: (703) 605-6900
E-Mail: orders@ntis.fedworld.gov
Online order: http://www.ntis.gov/help/ordermethods.asp?loc=7-4-0#online

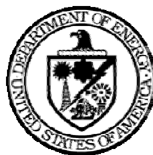

SAND2005-7067
Unlimited Release
October 2005

Novel In Situ Mechanical Testers to Enable Integrated Metal Surface Micro-machines

Sean J. Hearne, Maarten P. de Boer, Paul G. Kotula, Chris W. Dyck,
Stephen M. Foiles, David M. Follstaedt, Thomas E. Buchheit
Semiconductor and Nano-structure Physics
Sandia National Laboratories
P.O. Box 5800
Albuquerque, New Mexico 87185-MS1415

Abstract

The ability to integrate metal and semiconductor micro-systems to perform highly complex functions, such as RF-MEMS, will depend on developing freestanding metal structures that offer improved conductivity, reflectivity, and mechanical properties. Three issues have prevented the proliferation of these systems: 1) warpage of active components due to through-thickness stress gradients, 2) limited component lifetimes due to fatigue, and 3) low yield strength. To address these issues, we focus on developing and implementing techniques to enable the direct study of the stress and microstructural evolution during electrodeposition and mechanical loading. The study of stress during electrodeposition of metal thin films is being accomplished by integrating a multi-beam optical stress sensor into an electrodeposition chamber. By coupling the *in-situ* stress information with *ex-situ* microstructural analysis, a scientific understanding of the sources of stress during electrodeposition will be obtained. These results are providing a foundation upon which to develop a stress-gradient-free thin film directly applicable to the production of freestanding metal structures. The issues of fatigue and yield strength are being addressed by developing novel surface micromachined tensile and bend testers, by interferometry, and by TEM analysis. The MEMS tensile tester has a “Bosch” etched hole to allow for direct viewing of the microstructure in a TEM before, during, and after loading. This approach allows for the quantitative measurements of stress-strain relations while imaging dislocation motion, and determination of fracture nucleation in samples with well-known fatigue/strain histories. This technique facilitates the determination of the limits for classical deformation mechanisms and helps to formulate a new understanding of the mechanical response as the grain sizes are refined to a nanometer scale. Together, these studies will result in a science-based infrastructure to enhance the production of integrated metal – semiconductor systems and will directly impact RF MEMS and LIGA technologies at Sandia.

ACKNOWLEDGMENTS

The authors would like to acknowledge Jerry Floro, Mark Rodriguez, Bonnie McKenzie, Jim Stevens, Peggy Clews, Joe Michael, Michael Rye, Gary Zender, Charles Barbour, Craig Johnson, W. Graham Yelton, and Luke Brewer for their contributions. Sandia is a multiprogram laboratory operated by Sandia Corporation, a Lockheed Martin Company, for the United States Department of Energy's National Nuclear Security Administration under contract DE-AC04-94AL85000.

CONTENTS

1. Introduction 8

2. On-chip laboratory kit for freestanding metal film mechanical property testing 8
    2.1 Part I - Analysis 8
        2.1.1 Introduction 8
        2.1.2 Thin film mechanical test structure suite 9
        2.1.3 Modeling 12
        2.1.4 Fracture toughness assessment 21
        2.1.5 Summary and Conclusions: 21
        2.1.6 References for Section 2.1 23
    2.2 Part II – Experiments 25
        2.2.1 Introduction 25
        2.2.2 Sample fabrication, measurement procedures and analysis methods 27
        2.2.3 Elastic properties 29
        2.2.4 Load-induced plastic deformation and fatigue 35
        2.2.6 Summary & Conclusions 40
        2.2.7 References for section 2.2 42

3. Stress during island coalescence 45
    3.1 Introduction 45
    3.2 Background and Experiment 46
    3.3 Conclusion 53
    3.4 References for Section 3 54

4. Stress During Electrodeposition 55
    4.1 Stress during Ni electrodeposition 55
        4.1.1 Introduction 55
        4.1.2 In-situ stress measurements 56
        4.1.3 Compressive stress generation mechanism / discussion 59
        4.1.4 Conclusions 66
        4.1.5 References for Section 4.1 67
    4.2 Stress during NiMn electrodeposition 69
        4.2.2 Experimental set-up 69
        4.2.3 Results / Discussion 70
        4.2.4 Conclusions 76
        4.2.5 References for Section 4.2 77

5. Atomistic simulations 78
    5.1 Mechanical response of thin film nanoscale materials 78
    5.2 Atomistic simulations of stress in NiMn 82
    5.3 References for section 5 85

6. Conclusions 86

7. Appendix 87
7.1 Appendix A 87
7.2 Appendix B - Progress toward tuning the residual stress 87
7.3 Appendix C - Actuation of cracked structures 89

Distribution 92

NOMENCLATURE

DOE	Department of Energy
SNL	Sandia National Laboratories
RF	Radio Frequency
CMP	Chemical Mechanical Polishing
MEMS	Micro electro-mechanical systems
FIB	Focused Ion Beam
TEM	Transmission electron microscope
STEM	Scanning transmission electron microscope
SEM	Scanning electron microscope
STM	Scanning tunneling microscope
RBS	Rutherford back-scattering
AFM	Atomic force microscope
MOSS	Multi-beam optical stress sensor
UV	Ultra violate
FCC	face center cubic
ERD	Elastic recoil detection
SIMS	Secondary ion mass spectroscopy

1. INTRODUCTION

Predictable performance, reliability, and manufacturability are required to introduce new devices into DOE technologies. This is particularly important when the technology is required to satisfy congressionally mandated stockpile surety requirements. One such technology that could impact many of Sandia's defense customers is integrated metal–semiconductor micromechanical systems for use in RF MEMS and LIGA. Metals are of interest because of their improved conductivity and reflectivity over polysilicon. For example, metal-based RF MEMS technology could replace the bulky RF system presently used in communications, navigation, and avionics systems[1]. Additionally, the increases in yield strength observed with nano-grained materials will greatly enhance the available applications of this technology. However, stress gradients[2,3] and unknown fatigue lifetimes[4] have prevented the implementation of this technology. To address these issues we have implemented a multi-pronged program: First, we developed multiple MEMS based tensile testers to study the yield and fatigue properties of nano-grained metal films. Second, we used a wafer curvature based stress sensor *in situ* of an electrodeposition system to study the sources of stress during electrodeposition of Ni, NiMn, and geometrically restricted films. Third, we developed atomistic models to study dislocation motion in nano-grained thin films.

2. ON-CHIP LABORATORY KIT FOR FREESTANDING METAL FILM MECHANICAL PROPERTY TESTING

2.1 Part I - Analysis

In part I, we propose and analyze a notched free-standing thin film structure for *in-situ* mechanical testing of thin films subject to pure tension. Coupled with adjacent cantilevers and fixed-fixed beams, the structure enables a platform for evaluating linear properties such as Young's modulus and residual stress, as well as permanent deformation processes such as plasticity, crack propagation, creep, damping and fatigue. The experimental space that can be tested and the sensitivity of the structure to residual stress and to the pull-in instability are discussed.

2.1.1 Introduction

Polycrystalline silicon (polysilicon) is the most widely used structural material in surface micromachining and serves very well in applications such as inertial sensing [1,2]. While polysilicon is brittle, it has a high fracture strength of ~3 GPa [3] and exhibits no fatigue in applications where contact between structures is not allowed [4,5]. However, metals are of interest in micro-optics applications [6-8] because of their high reflectivity and also in radio-frequency microelectromechanical systems (RF-MEMS) [9-12] and microswitches [13,14] because of their high conductivity. Metals such as aluminum-based alloys [6,15] and gold [13,14] have been considered for application. Engineering the mechanical properties of such face-centered cubic-based metals at the microscale offer a substantial challenge. For example, the yield strengths of gold (σ_{ys} ~200 MPa), copper (σ_{ys} ~350 MPa) and aluminum (σ_{ys} ~200 MPa) metal thin films studied [16] are substantially lower than the fracture strength of polysilicon. From bulk materials studies, it is expected that metals in thin film form will be

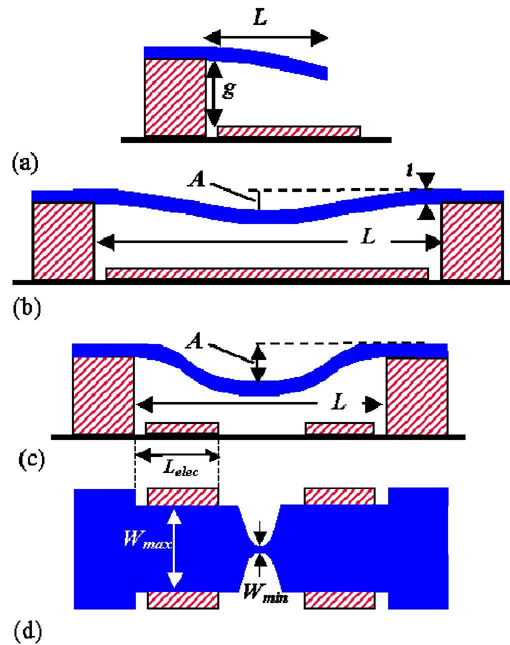

Figure 2.1 - Thin film metal test structure suite. The structures are actuated electrostatically by applying a potential between the structure and the underlying electrode. (a) cantilever (b) fixed-fixed beam (constant width) (c) notched fixed-fixed beam (side view) and (d) notched fixed-fixed beam (top view).

susceptible to fatigue. It is the object of this study to propose and investigate a suite of simple on-chip test structures that enable the measurement and understanding of elastic and permanent deformation processes associated with thin metal films. In particular, the notched structure, when combined with electrostatic actuation, is effective for high-cycle fatigue studies. This is directly relevant to MEMS applications, where billions or trillions of cycles are often expected from discrete structures.

2.1.2 Thin film mechanical test structure suite

The structures we propose for testing of thin film metal mechanical properties are represented schematically in Fig. 2.1. They are adjacent to each other on the test chip, are fabricated simultaneously and include a cantilever, a fixed-fixed beam and a notched fixed-fixed beam. They are actuated electrostatically by applying a potential between the structure and the underlying electrode. Dimensions of interest include the length of the structure L, the film thickness t and the gap between the structure and the electrode g. The width of a particular structure is denoted by w and the amplitude of actuation is A.

From the cantilevers in Fig. 2.1(a) we obtain properties such as curvature κ (due to residual strain gradient through the thickness of the film) and Young's modulus, E. The latter is obtained by actuating the structure, measuring the flexures by interferometry, and comparing to a

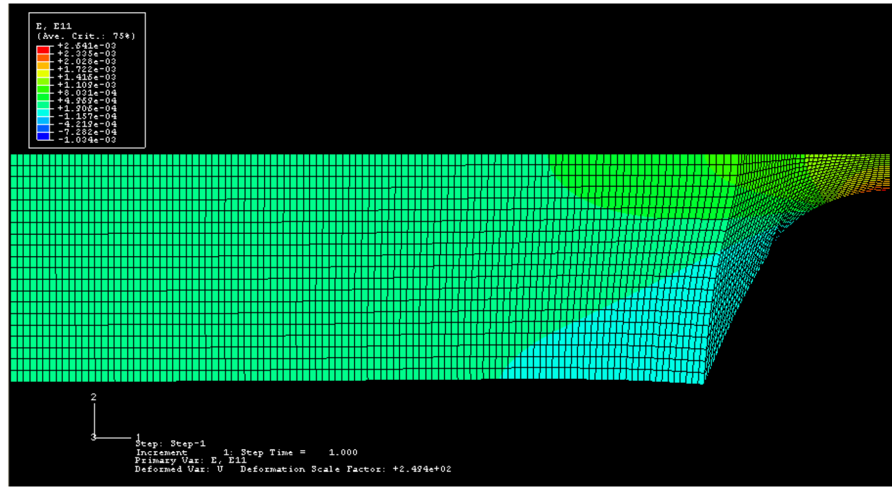

(a)

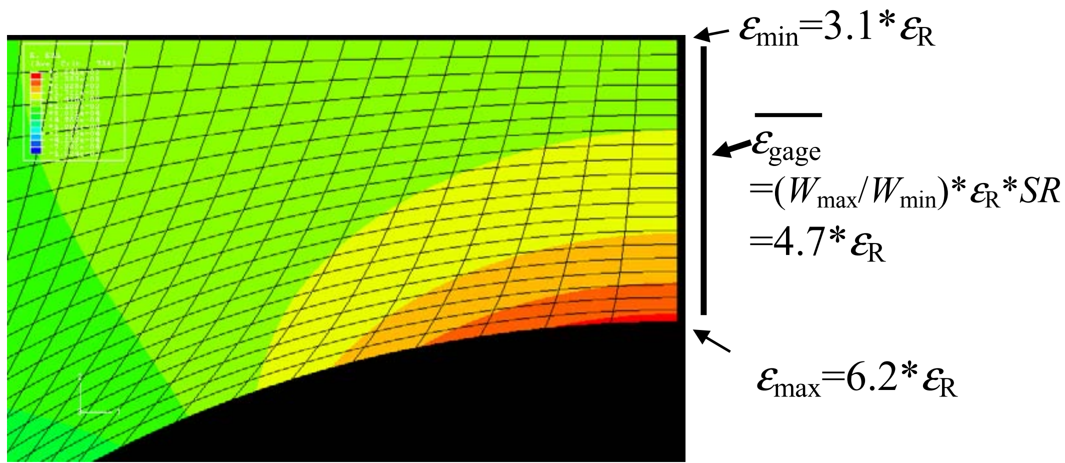

(b)

Figure 2.2 - Two-dimensional linear elastic finite element analysis in the notch section with W_{max}/W_{min}=5.8 (W_{max}=47.2 μm, W_{min}=8.2 μm). For this geometry, *SR*=0.873. (a) Quarter-section model (b) Local strains in notch section.

model that takes the curvature and the electrostatic loading into account [17]. In the model, we iterate on the value of E until the best agreement with the measured deflections are found. The width w of the cantilevers is nominally chosen to be w=25 μm. This is narrow enough that the films are nearly flat in the width direction, making parameter extraction more accurate. The fixed-fixed beams in Fig. 2.1(b) are also of width w=25 μm. From these, we measure the uniaxial residual strain in the film. The measurement methodology is similar to that of the

cantilevers. Knowing the Young's modulus and using a model that takes strain stiffening and the electrostatic loading into account, we obtain the residual strain ε_R [18].

The notched fixed-fixed beam structure is shown in Figs. 2.1(c) and (d) and can in principle be used to obtain information on non-linear properties such as yield, fracture toughness, fatigue, creep, viscoelasticity, and stress relaxation. Tensile strain is strongly enhanced in the gage section if there is residual tension in the film. The structure can be actuated to further enhance the strain. The maximum deflection $A_{\max}$ of these structures is approximately $g/3$, and is limited by an electrostatic instability known as pull-in [19].

There are several important differences between the notched structure and the fixed-fixed beam. First, its width is not uniform. Because force is transferred through the structure, strain in the gage section is strongly enhanced. Second, the actuating electrode does not span the full length of the structure. This configuration is known as leveraged bending [20], which extends the pull-in limit so that $A_{\max} > g/3$ can be achieved. To first order, applied residual strain is proportional to $(A/L)^2$. For a given L, as L_{elec} decreases, $A_{\max}$ increases. The limitation to this strategy is that the maximum voltage must be increased. Although the air dielectric breakdown field for small gaps is enhanced by the Paschen effect [21], arcing due to field enhancement generally limits the maximum safe voltage to $V_{\max}$=300 V in our experiments.

In the leveraged-bending configuration the film experiences only a small moment in the central area where there is no electrode. Hence the gage section is nearly flat when an actuation voltage is applied. Therefore, nearly pure tension due to stretching is applied to the central notched section as the beam deflects out-of-plane. Also, stiff support posts are required maximize the strain in the gage section in the notched structure. It is crucial in this test structure that stiff posts be realized experimentally. This has the added benefit of simplifying the modeling. We shall fix post compliance to be zero in our analysis below, and justify this assumption in the experimental section.

In principle, considering the known limitations of voltage, the test structure geometry can be optimized to maximize the strain range. However, the optimum parameters including L, L_{elec} and shape depend strongly on the residual strain, which is usually not known in advance. In view of this, it is best to include a number of geometry variations on the chip. Regarding the shape, earlier design work indicated that it was difficult to maximize the stress in a gage region of constant width. Rather, stress tended to be maximum and localized in the adjacent fillet [22]. Therefore, the notch was defined by an angled cut from the wide section, and the gage region was defined by an arc of constant radius. Stress in this structure is maximized locally at a position known to be at x-position=$L/2$. Table I shows the layout variations explored in this work. Devices 1-3 have L=360 μm, while Devices 4-6 have L=160 μm. The gap height g=12 μm is set by the height of the metal layer, which is on the fourth polysilicon layer and is intended for bonding purposes. Although this entails using high voltages, $A_{\max}$ is large and therefore large strains can be induced.

2.1.3 Modeling

We develop models of increasing complexity. The first model allows us to estimate the strains that can be found in the gage section based on experimental measurement of A. Then, we improve this model using a computer-based iterative solution that takes into account the electrostatic loading and the strain stiffening of the notched structure. Finally, we compare results to a full 3-D model.

Table I Geometric Variations and Stiffness Ratios

Device #	L (μm)	L_{elec} (μm)	W_{min}* (μm)	WR	SR (analytic)	SR (FEM)
1	360	150	2.2	21.91	0.696	0.588
2	360	150	8.2	5.88	0.873	0.773
3	360	150	18.2	2.65	0.947	0.889
ff	500	250	22.2	1	1	1
4	160	50	2.2	21.91	0.518	0.387
5	160	50	8.2	5.88	0.753	0.601
6	160	50	18.2	2.65	0.906	0.780

Also, W_{max} *=47.2 μm, t=0.6 μm and g=12 μm.
*W values account for line width loss $2 \cdot \Delta W$ =2.8 μm.

2.1.3.1 First-order model

Let us consider the strain in the gage section due to residual strain only. Residual strain commonly exists in thin film samples due to either intrinsic (recrystallization, grain growth, vacancy annihilation or extrinsic (thermal coefficient of expansion difference) mechanisms [23]. Before release, residual stress is sustained by adhesion of the film to the substrate, which consists of a sacrificial oxide and support posts. These are at identical heights so that there is no step at the oxide to post interface. The oxide is removed in a sacrificial etch, and the stress that remains in notched structures is analyzed next.

Consider a film of uniform width W_{max} initially attached to only one post. We stretch the film a distance Δ, such that $\Delta / L = \varepsilon_R$. To maintain the strain in the film, we attach it to the other post. This defines the amount Δ by which a notched structure of non-uniform width is also stretched, but in that case we apply less force to get the same displacement. We define the stiffness ratio SR as the ratio of force to stretch the notched sample relative to the force to stretch a sample of uniform width by Δ. Although the force in the notched sample is somewhat less than the uniform width sample, the strain at the gage section is amplified by the width ratio $WR = W_{max} / W_{min}$. The average strain in the gage section of a notched structure is then (see Appendix 1)

$$\overline{\varepsilon_{gage}} = \varepsilon_R (SR) WR \quad \text{(eq. 2.1)}$$

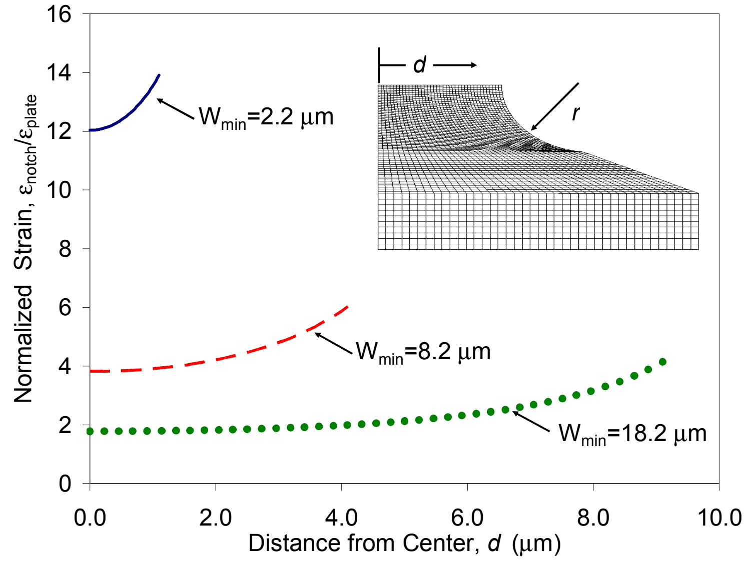

Figure 2.3 - 2-d FEM results of strain amplification across the gage section with L=360 μm. As WR increases, the strain is amplified but also becomes more uniform.

For notched devices, $0 < SR \leq 1$. However, the product $\{SR\,(W_{\max}/W_{\min})\}$ is greater than 1, and can be 10 or more. The in-plane film stiffness can be approximated as N springs in series. Each spring has length ΔL and average width W_{av}. The analytic result for the stiffness ratio is

$$SR = \left(\frac{L}{W_{\max}}\right)\left(\sum_{i=1}^{N}\frac{\Delta L}{W_{av,i}}\right)^{-1} \qquad \text{(eq. 2.2)}$$

The analytic stiffness ratio is tabulated for the notched geometries in Table I.

The analytic calculation of SR gives an approximate value that overestimates the true SR because strain is not uniform across each width element. Linear elastic two-dimensional finite element analysis accurately determines the stiffness ratio as well as the local strains. It is important to consider the stress state when carrying out this analysis. Before the release of the structure, the film is in a biaxial stress state. Upon release, the edges of the film are free to contract except at the support posts. Because $L/W_{\max}$=7 (for L=360 μm), we do not expect a full uniaxial state to be realized. The finite element analysis was carried out using a coefficient of thermal expansion analysis to best estimate the true stress state in the film. The more accurate SR values are given in Table I.

In Fig. 2.2, we show the 2-D FEM results for Device 2 (L=360 μm and WR=6). For this geometry, which we focus on in the experimental section, we find more accurately that SR is

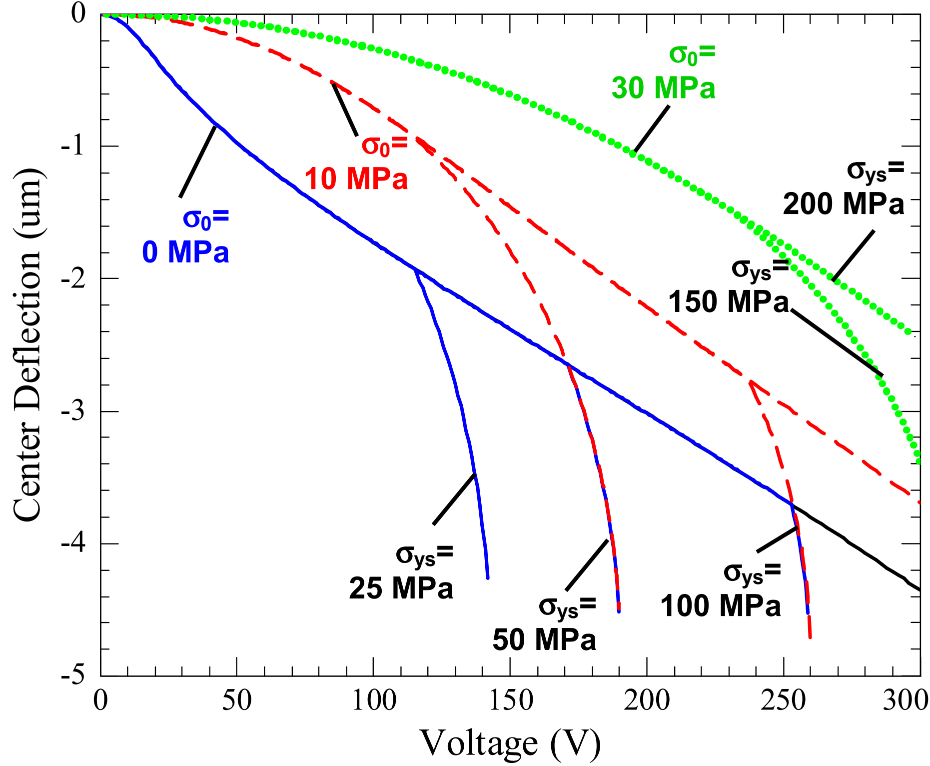

Figure 2.4 - Quasi 3-d elastic-plastic simulation of notched structure center deflection versus applied voltage. Assumed parameters include W_{max}=47.2 μm, W_{min}=8.2 μm, L=360 μm, SR=0.773, L_{elec}=150 μm, g=12 μm, t=0.6 μm, υ=0.33, E=70 GPa, V_{step}=1 V.

0.89 instead of 0.95 as obtained analytically. This accordingly reduces the value of $\overline{\varepsilon_{gage}}$ by 6%. Due to the stress concentration in the notch, we see that the maximum strain is $6.2\,\varepsilon_R$, while the minimum value at the center of the gage is $3.1\,\varepsilon_R$. In Fig. 2.3, we plot the strain amplification across the gage section for the three different width ratios with L=360 μm. We see that as WR increases, the strain in the gage becomes more uniform. For WR=2.65, the strain varies by ~105%, while for WR=22, the strain varies by only ~13%.

Upon actuation of the notched beam, the film lengthens and the enhanced gage section strain remains very nearly in pure tension. Using a simple triangle approximation for the deflection shape, the average gage section strain, $\overline{\varepsilon_{gage}}$, can be calculated as

$$\overline{\varepsilon_{gage}} \approx \left(\varepsilon_R + c\left(\frac{A}{L}\right)^2 \right)(SR)\ WR \qquad \text{(eq. 2.3)}$$

The constant c takes the shape into account. This model does not take plasticity into account. However, with $A_{\max}$=4 μm, simple calculations demonstrate that significant strains can be achieved in the gage section, and justify a more accurate model, which we develop next.

2.1.3.2 Quasi 3-D model

We next report results from a beam model that takes residual strain, strain stiffening, electrostatic actuation (with fringing field), the geometry of the notched structure, and an elastic perfectly-plastic transition into account. We model the out-of-plane flexures as a function of the applied voltage and quantify the degree of bending versus tension. The model is an extension of the finite difference previously reported [18]. Because the strain stiffening effect is due to membrane stretching, we use the FEM value for SR from section 2.1.3.1. The model calculates the average strain in the gage section. Because the stress state is predominantly tensile, the stress distribution across the gage section as in Fig. 2.3 adequately represents the local stresses. We incorporate plasticity in the model by assuming an elastic, perfectly plastic response. Once σ_{ys} is attained in the gage section, the in-plane force remains constant. It is assumed that the plastic zone is one micron in length. This length is on the order of the size of regions of high dislocation density once plastic straining occurs.

This quasi 3-D model will allow us to more closely simulate the true beam behavior. A full 3-D model would more accurately predict the notched structure behavior. In particular, it would take bending across the width of the "wing tips" of the notch structure into account. However, this is computationally intensive; the quasi-3-D model converges in less than a second for each voltage-loading value. Also, given that we lack detailed knowledge of the plastic zone behavior, a full 3-D model would also be imperfect. From the experiments, we shall see that the wing tip deflection is not large in comparison with the gap, and therefore the model presented in this section is expected to capture the most significant effects.

With the effect of plasticity included, we now explore results from the quasi-3D model in more detail. In Fig. 2.4, the center deflection is plotted for a structure with WR=6 and L=360 μm. For σ_R=0 MPa, as voltage increases, the center deflection is approximately linear if a yield limitation is not reached. This behavior is due to strain stiffening in the beam. Deviations from the elastic curve for σ_{ys}=25, 50 and 100 MPa are seen. It is important to note that although the change to plasticity represents a softening of the structure, the structure is not immediately subject to pull-in. This observation enables us to study fatigue of the metal over a rather wide amplitude range. Similar behavior is observed for σ_R=10 MPa. For a given σ_{ys}, deviation from the elastic response occurs at a lower voltage than for σ_R=0 MPa, but as V_a increases, the deflections converge because the force in the gage section is the same. Again, qualitatively similar results are observed for σ_R=30 MPa. It should be noted that for this value of σ_R=30 MPa, yield has already occurred for an un-notched beam for $\sigma_{ys} \leq$100 MPa.

In examining Fig. 2.4, it is important to keep in mind that the quasi-3D model treats each element as having the same strain across its width. As shown in Fig. 2.2, the maximum strain in the gage section is actually about 50% higher than the average for this WR. Therefore, we

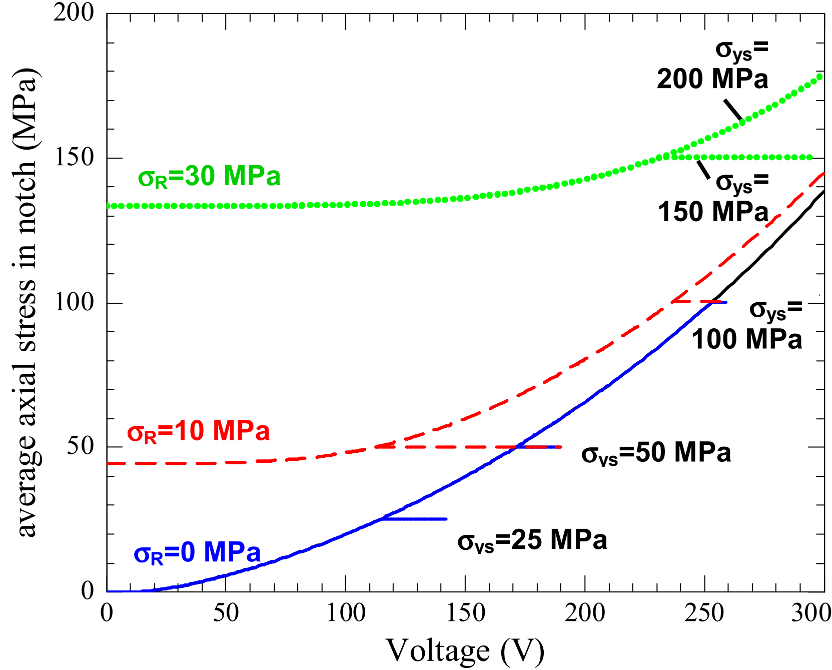

Figure 2.5 - Quasi 3-d elastic-plastic simulation of notched structure average gage stress versus applied voltage. Assumed parameters same as Fig. 2.5. Local elastic stresses can be obtained in conjunction with Fig. 2.3.

expect that yielding would occur sooner than represented in Fig. 2.5, and that the detailed behavior in the plastic region would be different from that represented there. The deflections in Fig. 2.5 were calculated at 1 V increments (V_{step}=1 V). Therefore, the maximum deflection at a given yield stress, as limited by the pull-in instability, is a lower bound and accurate to within 1 V within the limitations of the model.

The relative contributions of σ_R and applied loading to the average gage section stress can be seen from Fig. 2.5. For σ_R=0 MPa, the stress increases monotonically with applied voltage until the yield stress is reached. For σ_R=10 MPa., the gage stress is dominated by σ_R for low voltages. The region of σ_R dominance increases as σ_R increases.

Another parameter of interest is the average strain that is experienced in the gage section. Keeping in mind that the plastic deformation is assumed to occur over a 1 μm-long region, this is shown in Fig. 2.6. Although pull-in limits our ability to examine material response at very large strains, the calculated plastic strain range of ~10% is substantial.

Using example values of L=360 μm, A=0 and 4 μm, ε_R=0.008% and 0.040%, Eq. (2.eq. 2.3) is plotted in Fig. 2.7 using a value of c=3. The value of A used in Eq. (2.3) is obtained from the quasi 3-D model at 300 V. In experiments, it can be taken directly from measurements. Good agreement between the quasi 3-D model is seen. Taking E=70 GPa (the bulk value for Al), these values of ε_R correspond to residual stress values of σ_R=6 and 30 MPa, respectively. For

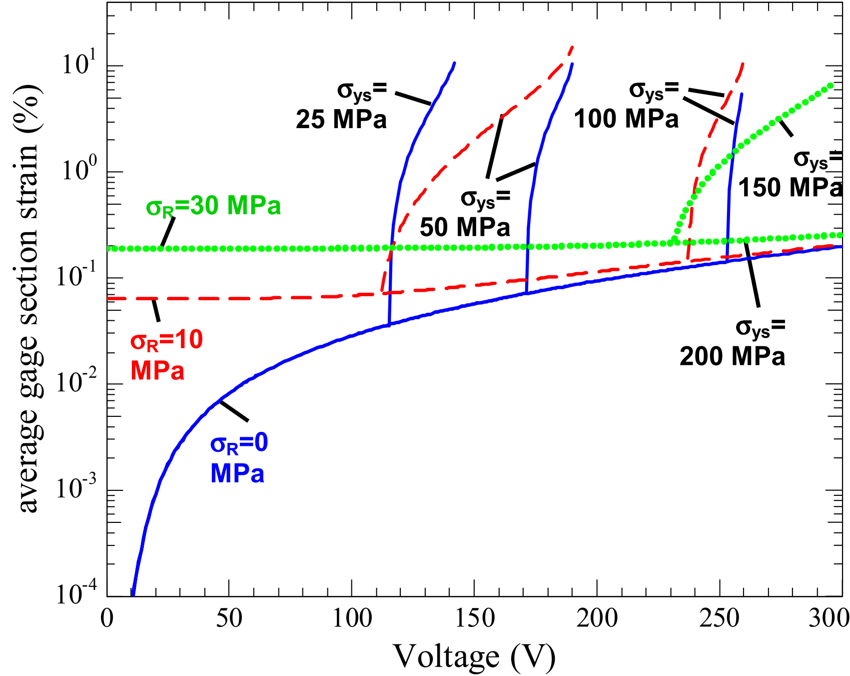

Figure 2.6 - Quasi 3-d elastic-plastic simulation of notched structure average gage strain versus applied voltage. Assumed parameters same as Fig. 5. If the structure yields, we can expect up to ~10% strain in the gage section before pull-in.

reference, a typical yield strain for thin film metals of ε_{ys} ~0.22 % corresponds to σ_{ys} =154 MPa. From Fig. 2.7 we see that the strain range of the structures depends strongly on ε_R. If ε_R is small, the strain range is large for WR=22. That width ratio would then be the most useful. On the other hand, if ε_R is large, the structure with WR=22 is likely to yield or perhaps fracture even for A=0 μm. A structure with a smaller width ratio, such as WR=6 may have already yielded, but will allow us to examine effect of plasticity in the notch zone. However, the smallest width ratio structure with WR=2.7 may not activate plasticity even upon actuation. Hence, a low residual strain, if it can be achieved, is most effective for this test structure geometry. If the residual strain is large, however, we can expect to access all the interesting regions if a sufficient number of layout variations exist.

In Section 2.2, it was argued that the state of stress in the gage section is nearly pure tension. This is motivated by two considerations. First, the films are thin and hence the stretching contribution should dominate over the bending contribution. Second, in the leveraged bending configuration, there is no loading in the center portion of the structure. From a free-body diagram as seen in Fig. 2.8, the internal moment M_c enforces the boundary condition of zero slope at the beam center. As the quantity ($L/2 - L_{elec}$) increases, M_c decreases and the bending contribution to the gage section stress tends towards zero.

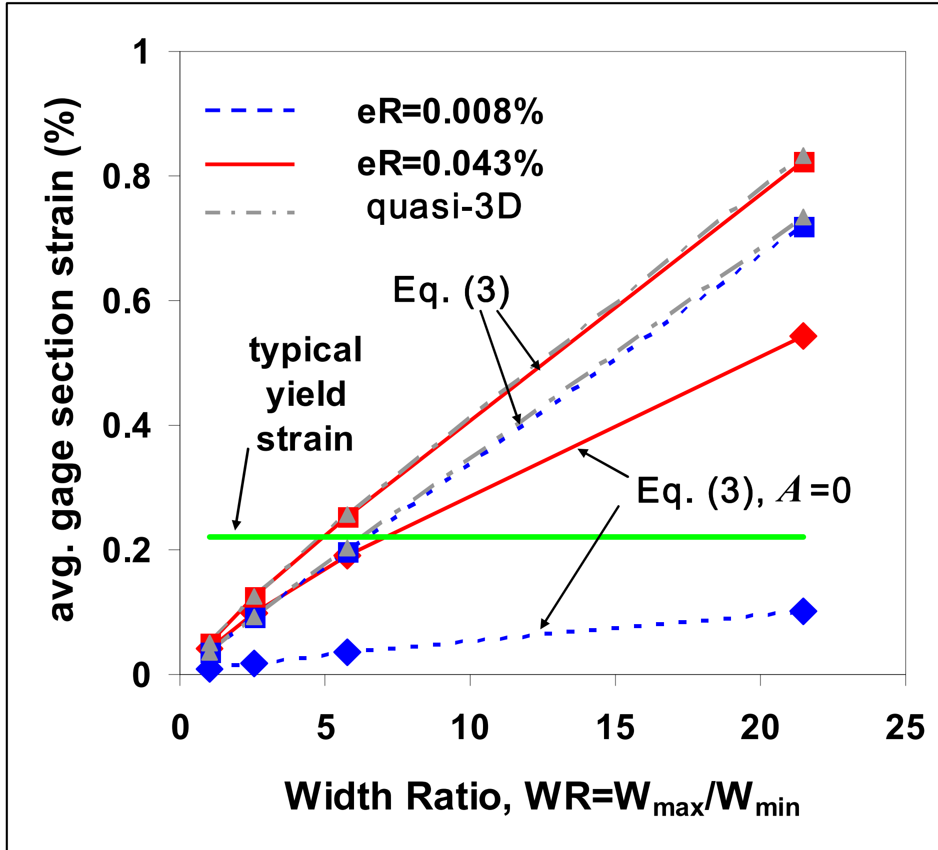

Figure 2.7 - Elastic analyses. Eqs. (3) (with A=0 μm) and Eq. (3) (with A as taken from quasi 3-D results) plotted versus WR. (WR values are indicated by the symbols and are taken from Table I). Also includes more accurate quasi-3D simulation, with a maximum "safe" applied voltage V_{app}=300 V.

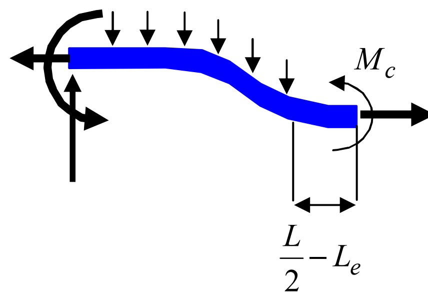

Figure 2.8 - Schematic free body diagram. The moment at the center of the beam, M_c, is applied internally to enforce the zero slope center boundary condition.

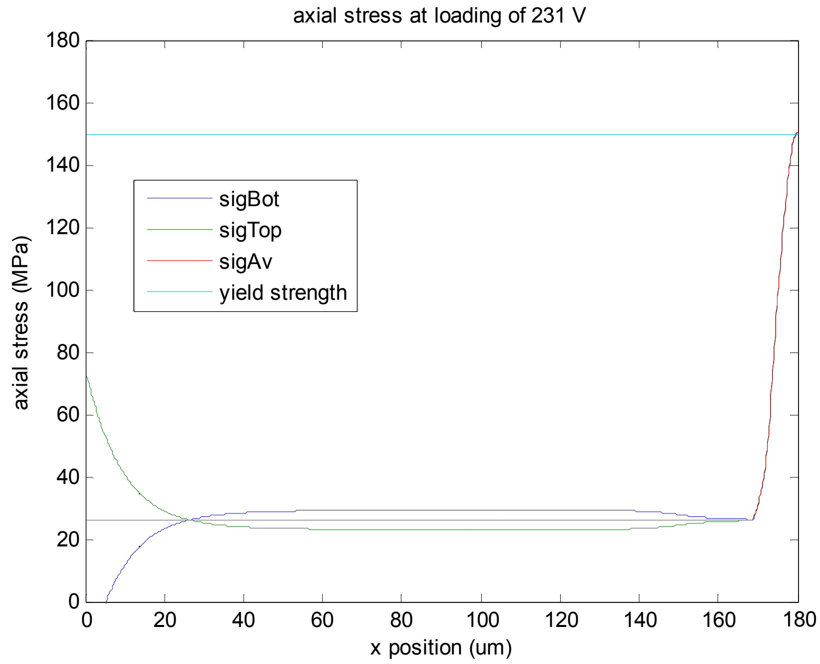

(a)

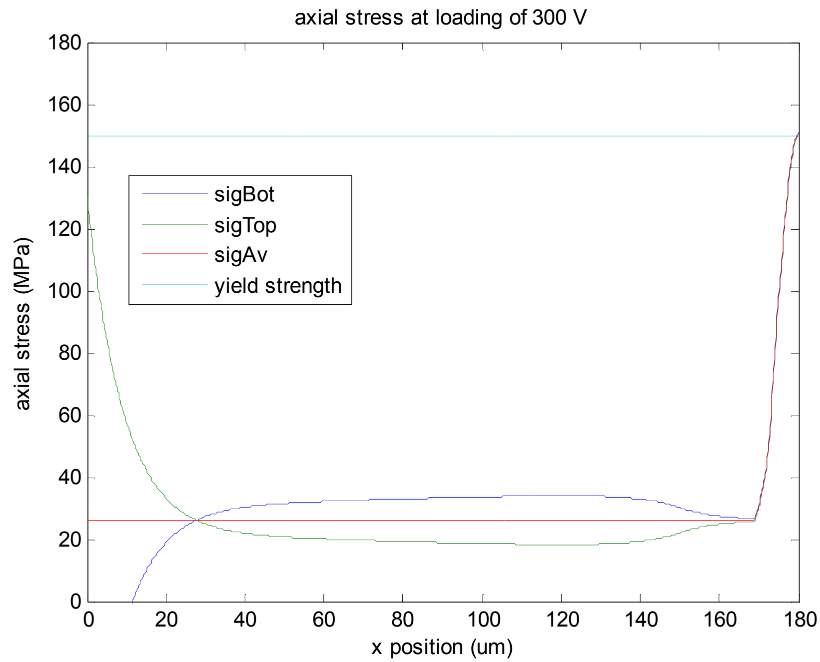

(b)

Figure 2.9 - Axial stress versus position at maximum voltage loading for Device 2. Parameters the same as in Figs. 2.4-2.6, with σ_R=30 MPa, σ_{ys}=150 MPa (a) at onset of yield (b) at maximum voltage.

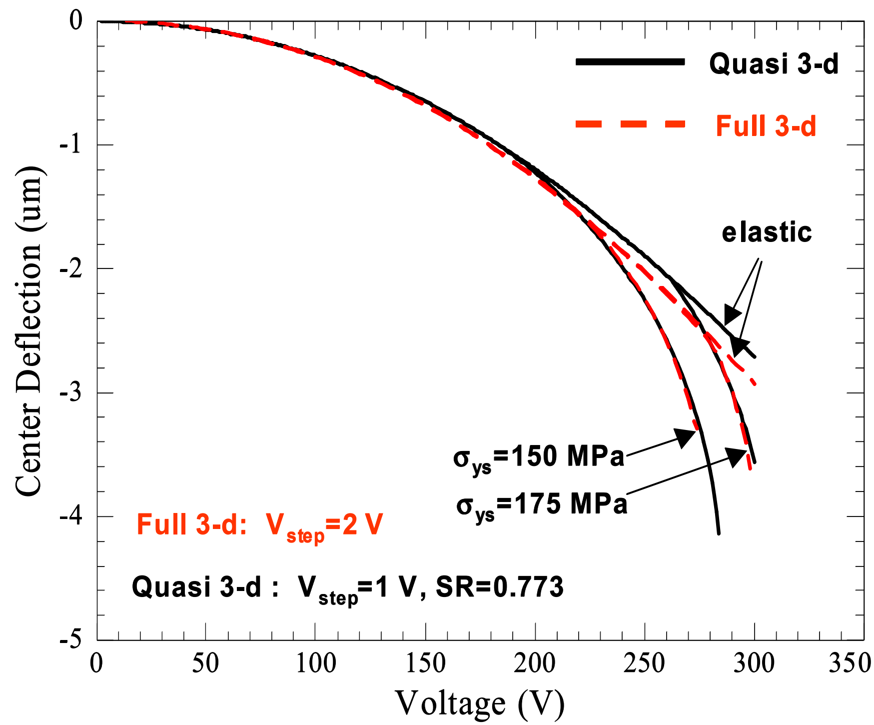

Figure 2.10 - Deflection comparison between Quasi 3-d and full 3-d results for Device 2 with σ_R=32 MPa. Excellent agreement is observed in both the elastic and the plastic regimes.

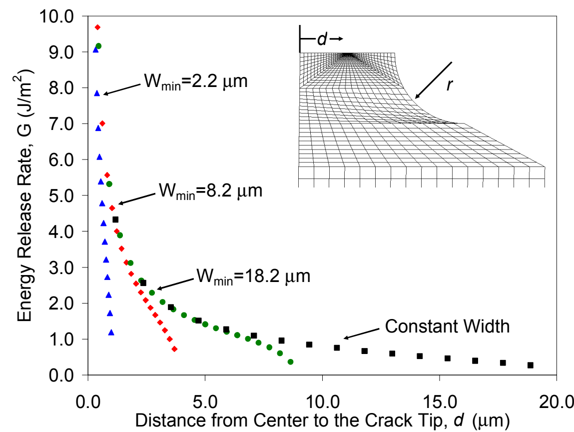

Figure 2.11 - J-integral results assuming σ_R=32 MPa. If cracks initiate on both sides, they will grow in an unstable fashion. However, if the cracks initiate on only one side, growth can be stable.

The exact moment in the gage section depends on the details of the geometry, loading and residual strain. An example of the axial loading versus position in the notch structure is shown in Fig. 2.9. The parameters here are the same as in Figs. 2.4-2.6, and furthermore σ_R=30 MPa and σ_{ys}=150 MPa. At the onset of yield at V_a=231 V as in Fig. 9(a), we see that in the gage section the stress at the top and the bottom of the film are virtually identical. This remains true at V_a=300 V in Fig. 2.9(b), the maximum load. For a given loading due to V_a, the state of stress in the gage section tends towards pure tension as σ_R, WR and $(L/2 - L_{elec})$ increase. However, it should be noted that beyond yield, the bending strain at the edge of the film (x-position=0 μm) increases with loading while the stress in the notch remains the same. This is seen by comparing Figs. 2.9(a) and 2.9(b), and should be kept in mind when analyzing experiments. Of course, this issue is minimized if t can be reduced.

2.1.3.3 Validation of Quasi 3-D model

The advantage of the Quasi 3-D is that the analysis time is short – it converges in less than one second at each applied voltage. However, given its shortcomings, our confidence in it can be enhanced by a full 3-D model. Therefore, we implemented a full 3-D model for Devices 2 and 3 using the coupled electromechanical module in ANSYS. The convergence time for this model is approximately 2000 times longer than the Quasi 3-D model. The local stresses were implemented in terms of an elastic-perfectly plastic constitutive law. Example results for Device 2 for an elastic model and for two values of σ_{ys} shown in Fig. 2.10. The elastic flexures of the full 3-D model are slightly larger than the quasi 3-D model. This is likely due to the greater force at the wing tips. Even though the onset of plasticity occurs sooner in the 3-D model because the notch stress concentration is now properly modeled, the deflection curve does not deviate strongly from the elastic curve until the plastic zone has spread across the entire notch. Of course, upon unloading a plastically deformed structure would display larger deflections for the same voltage than upon the previous loading. Another important observation is that the deflections in the plastic region agree very well with those predicted by the Quasi 3-D model.

2.1.4 Fracture toughness assessment

We also consider briefly the ability to use this structure to assess the fracture toughness of the thin film. Figure 2.11 shows J-integral results if cracks initiate on both sides of the notch. Although the sample is unstable with respect to crack growth, if cracks initiate an upper bound for the fracture toughness can be determined. If cracks initiate on one side only, crack growth can be stable, as previously found [24].

2.1.5 Summary and Conclusions:

We have proposed and analyzed a simple laboratory kit for extracting elastic and plastic properties of thin film metals. The kit features on-chip, self-loading test structures whose full-field deflections can routinely be measured by interferometry at the nanometer scale. The cantilever and fixed-fixed beam are already very well known structures. They compliment the notched structure, from which we can extract non-linear properties. Elastic analysis of the notched structure indicates that very large strains are possible, and therefore that the structure is likely to yield in the gage section. The strains can be induced by residual stresses in the film, by

actuation, or by a combination of these. A simple model (Eq. (2.eq. 2.3)) is useful for estimating elastic strains if the center deflection amplitude is measured. The quasi 3-D model indicates that the notched structure is stable with respect to pull-in up to about 10% straining in the gage section. It also shows that the state of stress in the gauge section is very nearly pure tension. The departure from elastic behavior is distinct and the range over which non-linear behavior is expected is reasonably large. A full 3-D analysis agrees very well with the predictions of the Quasi 3-D model. In Part II, we shall examine this structure experimentally.

2.1.6 References for Section 2.1

[1] A. A. Seshia, M. Palaniapan, T. A. Roessig, R. T. Howe, R. W. Gooch, T. R. Schimert and S. Montague, *A vacuum packaged surface micromachined resonant accelerometer*, J. Microelectromech. Syst. **11** (6), 784 (2002).

[2] V. Annovazzi-Lodi, S. Merlo, M. Norgia, G. Spinola, B. Vigna and S. Zerbini, *Optical detection of the coriolis force on a silicon micromachined gyroscope*, J. Microelectromech. Syst. **12** (5), 540 (2003).

[3] D. A. LaVan, B. L. Boyce and T. E. Buchheit, *Size and frequency of defects in silicon MEMS*, Int. J. Dam. Mech. **12**, 357 (2003).

[4] S.L. Miller, M.S. Rodgers, G. La Vigne, J. J. Sniegowski, P. J. Clews, D.M. Tanner and K.A. Peterson, *Failure modes in surface micromachined microelectromechanical actuation systems*, Microelectronics Reliability **39** (8), 1229 (1999).

[5] A. D. Romig, M. T. Dugger and P. J. McWhorter, *Materials issues in microelectromechanical devices: science, engineering, manufacturability and reliability*, Acta Mater. **51** (19), 5837 (2003).

[6] P. F. van Kessel, L. J. Hornbeck, R. E. Meier and M. R. Douglass, *MEMS-based projection display*, Proc. IEEE **86** (8), 1687 (1998).

[7] D. Hah, S. T. Y. Huang, J. C. Tsai, H. Toshiyoshi and M. C. Wu, *Low-voltage, large-scan angle MEMS analog micromirror arrays with hidden vertical comb-drive actuators*, J. Microelectromech. Syst. **13** (2), 279 (2004).

[8] M. B. Sinclair, K. B**.** Pfeifer, M. A. Butler, S. D. Senturia, E. R. Deutsch, D. Youngner, E. Cabuz and G. B. Hocker, *A MEMS-based correlation radiometer*, Proceedings of the SPIE, Vol. 5346, edited by Ayman El-Fatatry, San Jose, CA, USA 2004), pp. 37-47.

[9] H.C. Nathanson, W. E. Newell, R. A. Wickstrom and J. R. Davis Jr., *The resonant gate transistor*, IEEE Trans. Elec. Dev. **ED-14** (3), 117 (1967).

[10] C. T. C. Nguyen, L. P. B. Katehi and G. M. Rebeiz, *Micromachined devices for wireless communications*, Proc. IEEE **86** (8), 1756 (1998).

[11] J. J. Yao, *RF MEMS from a device perspective*, J. Micromech. Microeng. **10** (4), R9 (2000).

[12] S. Lucyszyn, *Review of radio frequency microelectromechanical systems technology*, IEE Proc.-Sci. Meas. Technol. **151** (2), 93 (2004).

[13] S. Majumder, N. E. McGruer, G. G. Adams, P. M. Zavracky, R. H. Morrison and J. Krim, *Study of contacts in an electrostatically actuated microswitch*, Sensors and Actuators A **93** (1), 19 (2001).

[14] B. D. Jensen, K. W. Huang, L. L. W. Chow and K. Kurabayashi, *Adhesion effects on contact opening dynamics in micromachined switches*, J. Appl. Phys. **97** (10), 103535-1-9 (2005).

[15] Z. J. Yao, S. Chen, S. Eshelman, D. Denniston and C. Goldsmith, *Micromachined low-loss microwave switches*, J. Microelectromech. Syst. **8** (2), 129 (1999).

[16] H. D. Espinosa, B. C. Prorok and B. Peng, *Plasticity size effects in free-standing submicron polycrystalline FCC -films subjected to pure tension*, J. Mech. Phys. Sol. **52**, 667 (2004).

[17] B. D. Jensen, M. P. de Boer, N. D. Masters, F. Bitsie and D. A. LaVan, *Interferometry of actuated cantilevers to determine material properties and test structure non-idealities in MEMS*, J. Microelectromech. Syst. **10** (3), 336 (2001).

[18] M. S. Baker, M. P. de Boer, N. F. Smith, L. K. Warne and M. B. Sinclair, *Integrated measurement-modeling approaches for evaluating residual stress using micromachined fixed-fixed beams*, J. Microelectromech. Syst. **11** (6), 743 (2002).

[19] P. M. Osterberg and S. D. Senturia, *M-TEST: A test chip for MEMS material property measurement using electrostatically actuated test structures*, J. Microelectromech. Syst. **6** (2), 107 (1997).
[20] E. S. Hung and S. D. Senturia, *Extending the travel range of analog-tuned electrostatic actuators*, J. Microelectromech. Syst. **8** (4), 497 (1999).
[21] F. Paschen, *Ueber die zum Funkenuebergang in Luft, Wasserstoff und Kohlensauere bei verschiedenen Drucken erforderliche Potentialdifferenz*, 69-96 **37**, 69 (1889).
[22] M. P. de Boer, B. D. Jensen and F. Bitsie, *A small area in-situ MEMS test structure to measure fracture strength by electrostatic probing*, Proceedings of the SPIE, Vol. 3875, edited by Y. Vladimiirsky and C. R. Friederich, Santa Clara, CA (Sept. 20-21 1999), pp. 97-103.
[23] W. D. Nix, *Mechanical properties of thin films*, Metall Trans. A **20** (11), 2217 (1989).
[24] H. Kahn, R. Ballarini, J. J. Bellante and A. H. Heuer, *Fatigue failure in polysilicon not due to simple stress corrosion cracking*, Science **298** (5596), 1215 (2002).

2.2 Part II – Experiments

In part II, we demonstrate the fabrication of free-standing 0.6 μm thick Al/ 0.5 wt. % Cu thin film samples, successfully realizing a near zero compliance support post. We accurately measure Young's modulus and residual stress using cantilevers and fixed-fixed beams, respectively. Using the notched fixed-fixed beams, we demonstrate permanent deformation processes including plasticity and fatigue. We show that high cycle fatigue strength of this alloy is half of the material strength. We compare deformation processes on the samples deformed by yield and fatigue by ex-situ TEM.

2.2.1 Introduction

In Part I, a thin film mechanical laboratory kit including electrostatically actuated microcantilevers, fixed-fixed beams and a notched beam were proposed. The notched beam was analyzed in detail. Of particular interest, calculations indicated that even though electrostatic forces are weak, large and purely tensile strains can be applied in the gage section in this geometry. This is because axial forces are much larger than transverse forces in beams provided that the ends are truly fixed. Therefore, we can hope to measure thin film material limits such as strength and fatigue with this sample.

With electrostatic loading, several advantages over other loading techniques are anticipated. The first is that the handling and metrology issues of the pure mechanical methods are essentially eliminated. For example, for some gripper-type testers, the film must first removed from the substrate [1-6] and attached to a loading apparatus. In other cases, one end remains attached to the substrate [7-9]. Then, the top side of the free end is attached electrostaticly or adhesively to a fixed support and subsequently gripped by the loading apparatus. Besides the issue of installing the test specimen in the apparatus without damage, these procedures are time consuming. Also, during the loading process, sample misalignment is difficult to detect. In these procedures, sample handling may become more difficult as film thickness or width is reduced [10]. In our proposed method, handling is trivial because no sample gripping is required. We have tested films as thin as 0.2 μm and as narrow as 2.2 μm with no difficulty.

The second advantage is that the structures here are quite small, ~0.05 mm^2 each (including support posts and probing pads), and hence in principle can serve as diagnostic structures that are processed side-by-side with real MEMS devices. Because the gripper tests typically use very large test samples (several mm^2), placing them adjacent to MEMS devices is not practical in a production setting. Electrostatic actuation by comb drive actuation has been used successfully to test failure of thin films [11,12], but such actuators are also large because their force per unit area is small. For example a comb drive requiring an area of ~1.5 mm^2 was used to fracture polysilicon [11]. A small area device (~0.03 mm^2) has been successfully used to evaluate fatigue in polycrystalline silicon (polysilicon) [13]. However, resonance is required to obtain sufficiently high stresses, and therefore fatigue cannot be studied versus frequency. With the notched geometry, very high stresses can be applied without resorting to resonance for amplitude amplification. Therefore, fatigue can be studied as a function of frequency, which could be important due to localized heating effects.

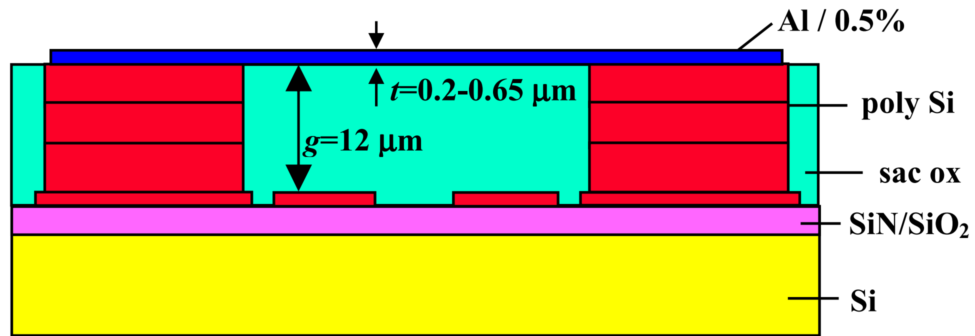

(a)

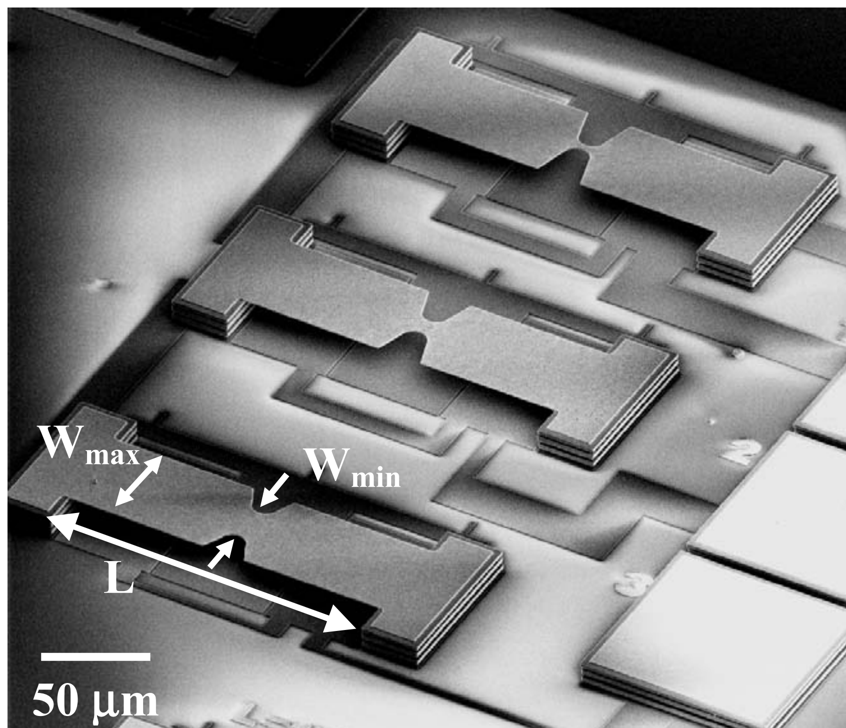

(b)

Figure 2.12 - (a) Schematic cross-section of process flow (b) SEM of released notched structure devices 4-6 (with L=160 µm, and W_{min}=18.2, 8.2, 2.2 µm)

The third advantage is that by using interferometry, full-field nanometer-scale information of the device flexures were obtained. Misalignment is a common concern with gripping apparatus tests, and difficult to characterize. With the present method, misalignment is unlikely because the structure is made by common surface micromachining methods. It can occur if for example the posts are not at the same height, but interferometry can easily detect post height differences

greater than ~20 nanometers. Interferometry enables us to closely compare measured and model values to obtain multiple measurements on a single structure.

Among the techniques reported in the literature, our structure and methodology is perhaps most similar to that demonstrated by Zhang [14] and Espinosa and coworkers [15,16]. They place fixed-fixed beams over a hole, stretch them by nanoindentation and measure deflections with interferometry. While fabrication of our proposed samples requires more processing steps, electrostatic testing gives us the ability to easily apply cyclic loading at tens of kHz. Because the fatigue strength of metallized MEMS may be significantly lower than the yield strength, this property deserves more attention than it has received thus far.

In the following, we will show that the laboratory tool kit can successfully be made. By measuring properties we shall assess the information that can be gained from these structures. Careful analysis reveals that although processing artifacts render the structure less than ideal, information on modulus, residual stress, yield strength and fatigue performance can be obtained.

2.2.2 Sample fabrication, measurement procedures and analysis methods

A schematic cross-section of the process sequence used to fabricate the structures is shown in Fig. 2.12(a). Beginning with a silicon wafer, a thermal oxide (0.6 μm) is grown and a low-stress SiN is deposited. This stack provides insulation between adjacent electrodes held at a different potential. Next, five levels of polysilicon are deposited, defined by photolithography and etched. The first layer, called Poly0, is 0.3 μm thick and in this mask level we make the actuating electrodes. The remaining polysilicon levels, each making contact through an underlying sacrificial oxide layer ("sac ox" in Fig. 2.12(a)), give a total nominal thickness of 12.4 μm (individual sac ox layers are not shown in Fig. 2.12(a)). Up to this point, fabrication follows the standard SUMMiT V^{TM} process flow [17].

The topmost polysilicon, Poly4, lies over the highest sacrificial oxide layer. If metal is deposited at this point, it will have to cover a step height approximately equal to the thickness of the polysilicon. This will result in a hinge-like overhang, which significantly increases the effective post compliance. The effective residual strain will be much less than the as-deposited residual strain, and the boundary compliance also makes any applied strain much less than the calculated strain. To solve this problem, we deposited another layer of sacrificial layer oxide, thicker than the Poly4 level, and then chemo-mechanically polished the oxide until a small amount of Poly4 was removed. The result was a smooth surface with no step perceived by interferometry (i.e., less than 10 nm) when crossing the polysilicon to oxide boundary.

A 0.7-μm thick Al / 0.5 wt. % Cu layer was now dc-magnetron sputter-deposited at 175 ºC and was followed by a 50 nm TiN sputter deposition. During subsequent processing, the highest temperature the sample experienced was 250 ºC for 3 minutes. The latter layer protects the topside of the Al/0.5% Cu film during the subsequent release etch. The Al/0.5% Cu film was then wet etched using a standard commercial reagent chemistry. The release agent, which dissolves the sacrificial oxide, but not the polysilicon, is an HF acid-based chemistry that has been modified to minimize etching of the Al/0.5% Cu film. After release, the overlying TiN film is removed by a selective wet etchant. An SEM of the resulting notched structures (Devices 4-6

per Table I of Part I) is shown in Fig. 2.12(b), where it is observed that the flatness of the films is good. Pads, where the potential difference V_a is applied, are adjacent to the structures and can be seen on the right hand side of Fig. 2.12(b). No physical contact, which could potentially damage these delicate films, is made to the structures during these measurements.

Cantilevers (L=50, 150, 300 and 420 μm, W=25 μm) and fixed-fixed beams (L=150, 300 & 500 μm, W=25 μm) were laid out adjacent to the notched structures. Including probing pads, the layout occupied by the 13 electrically probe-able structures is 0.83 mm^2. The area of a SUMMiT V^{TM} module is 17.9 mm^2, and eight such modules are available on a reticle. The structures thus occupy 0.6% of the available area, and are repeated some sixty times across a wafer.

We measured the thickness t and gap height g by mechanical profilometry. The longer cantilevers (L=300 and 420 μm) were used in these measurements. The gap measurement could be checked by interferometry, and agreement within ±20 nm was observed. Thickness t ranged from 0.43 to 0.65 μm and depended on wafer location as well as on the particular release. This is less than the deposited thickness because selectivity of the release agent to the Al/0.5% Cu film is finite. The gap g ranged from 11.25 to 12.5 μm and likewise depended on wafer position. As a result of the Al/0.5% Cu film wet etchant, the linewidth loss ΔW=1.4 μm per edge as measured by SEM is somewhat greater than the film thickness

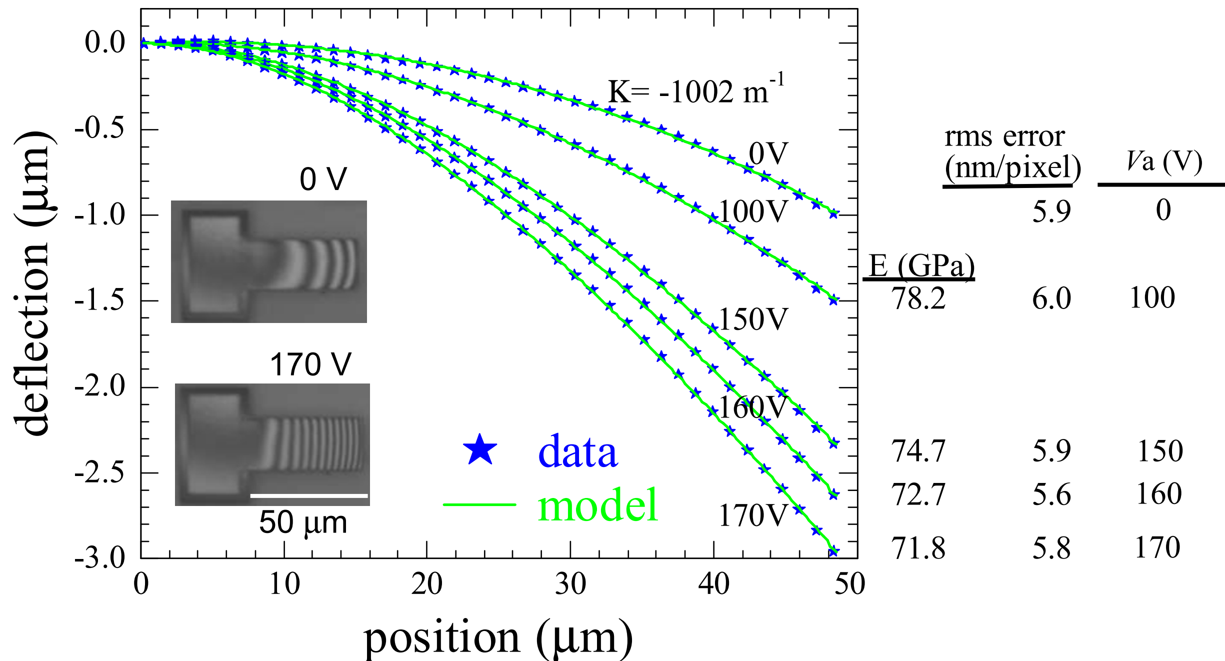

Figure 2.13 - Curvature and Young's modulus data are obtained from electrostatically-actuated microcantilevers. The inset shows interferograms of unactuated and actuated cantilevers, respectively.

Electrostatic loading was applied to the samples while deflection curves were measured. The interferograms for these measurements were obtained using a long-working distance interferometer [18]. A Hariharan phase-stepping interferometry (PSI) algorithm [19] was applied to obtain deflection versus position curves at a given applied loading V_a. For the notched structures, these were taken through the centerline. The curves are accurate to ±10 nm. A convenient feature of these structures is that the top of the support posts are flat due to the CMP. Therefore, the interferometry data there is valid, and can be used to establish the point of zero deflection. (Polysilicon support posts often have much topography on a local scale, and therefore, it is difficult to obtain good deflection data and so establish a reference point with them).

Custom scripting software was written to measure deflection curves as a function of applied loading. For tests in which only monotonic loading was applied, a Keithley 487 picoammeter was used. The time required for a PSI measurement at a given voltage is one second. The scripting software was also used to take the fatigue data. In that case, a digital to analog signal was generated by the software (1 μsec time base), and fed into a 40 X gain amplifier with 400 Volt maximum output and a rolloff frequency of 500 kHz.

Scanning electron microscopy was performed using with both a Hitachi S4500 field emission SEM or an FEI DB235 focused ion beam (FIB) tool. The latter instrument is equipped with both a field emission SEM column and a focused ion beam column. Grain orientation analysis was obtained by SEM from backscattered electron Kikuchi patterns [20]. TEM was performed using an FEI Company Tecnai F30-ST tool operated at 300kV. A number of the images we acquired were collected in scanning TEM mode (STEM) with an Annular Dark Field (ADF) detector. Thin samples for TEM analysis were prepared in the DB235 FIB instrument by the external lift-out technique [21]. A statistical software package known as AXSIA (automated analysis of X-ray spectral images) was used to generate best fits to spectroscopic X-ray data [22].

2.2.3 Elastic properties

We measure curvature K on unactuated microcantilevers by comparing deflection data to model fits in which the curvature is varied. The measured value is taken from the best fit to the data. Integrating measurements and modeling in a similar fashion, Young's modulus E is obtained from electrostatically-actuated microcantilevers [23]. Because bending stiffness of beams depends on t^3 and electrostatic forces depend on g^2, measurement of both t and g on adjacent structures is important when properties such as E are quantified. Results for K and E, as extracted from the best fit models, are shown in Fig. 2.13. The film bends downward due to curvature K=-1002 m^{-1}, which is caused by the stress gradient through the film thickness. The Young's modulus is 74.4 ±2.8 GPa.. The relatively small variations in E demonstrate that the values for t and g have been reasonably well measured.

Given the <111> texture of the film (as will be shown below), the expected value of E is 68 GPa. The agreement is within 10%. This methodology was previously validated using

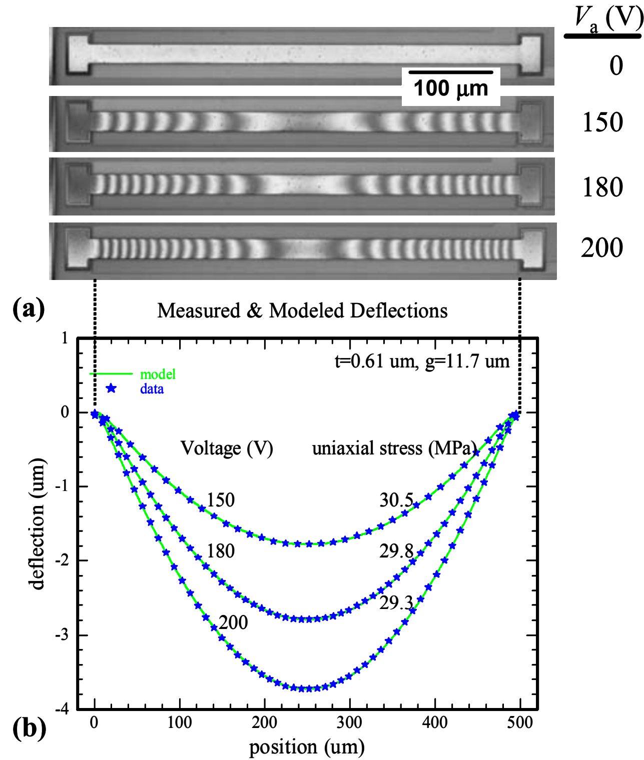

Figure 2.14 - Fixed-fixed beam residual stress measurement. (a) interferograms at various applied voltages and (b) Model fit with best residual value for different loadings indicated.

polysilicon cantilevers, where we measured E =164 GPa, which was within 2% from the value predicted from texture measurements [23]. In comparison to other methods on Al films, a value 65-70 GPa has been measured on the initial loading curve for e-beam-deposited, <111> textured Al films, using nanoindentation of fixed-fixed beams [16]. On the other hand, a value of only 30 GPa was reported for e-beam-evaporated Al that did not experience any temperature excursion using tensile loading [2]. A value of 57 ±3 GPa was measured on e-beam-deposited <111> Al films that were patterned photolithographically, and presumably experienced a short bake at ~100 ºC [4]. In both these tests, the modulus is measured by unloading after plastically deforming the film, and in fact the lower-than-expected modulus was attributed to microcracking [4]. We interpret our measurement to be very near the expected value because the grain structure in our film was stabilized, and the applied strains in the electrostatic method are miniscule. We will assume E =70 GPa, the bulk value for Al [24], in subsequent analysis.

Using a similar measurement and modeling procedure, we determine the residual stress σ_R on fixed-fixed beams. Details on the methodology are given in [25] and results are given Fig. 2.14. Note that the topmost interferogram in Fig. 2.14(a) shows no contrast – the beam is very nearly flat. Very likely, the beams are in tension, and the modeling verifies this initial judgment. For different loading values, we see that there is good reproducibility for σ_R in this measurement (30.5, 29.8 & 29.3 MPa). The value of σ_R represents the uniaxial stress state, and the technique allows us to find the local σ_R on each chip. Significant variation was observed with σ_R

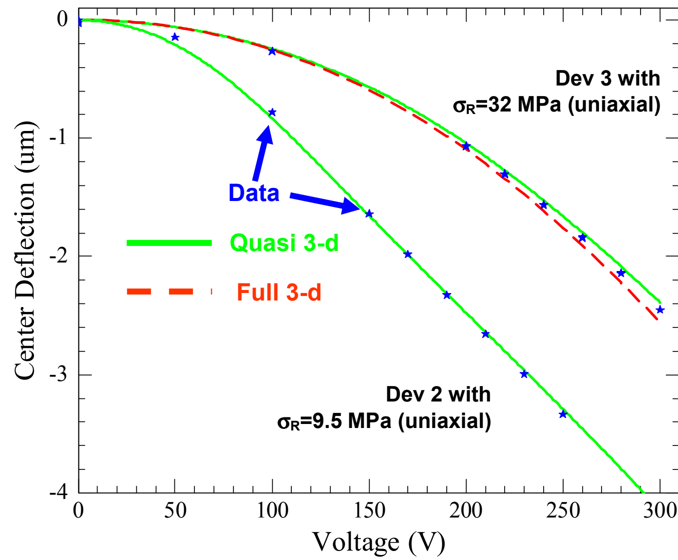

(a)

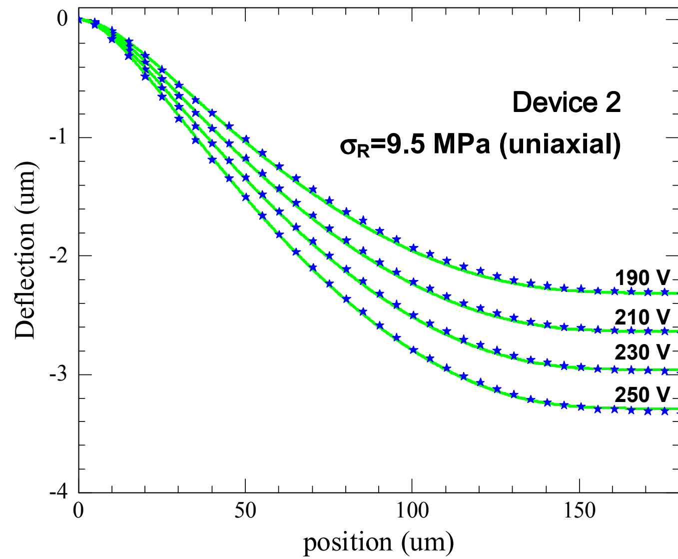

Figure 2.15 - (a) Center deflection curves. Data versus Quasi 3-d and Full 3-d models. (b) Device 2 deflections follow an elastic model but with reduced residual stress with σ_R=9.5 MPa (adjacent to aff beam with σ_R=32 MPa) .

ranging from 30 to 60 MPa. This variation was large from one release to the next, but much smaller within a release. The notched structures were now actuated. For the particular

measurements to be discussed here, σ_R=32 MPa was found on the adjacent fixed-fixed beams. Unloading curves were identical to loading curves for Device 3, indicating that no yielding is taking place due to the electrostatic loading. Other Device 3 structures with similar residual stress values were fatigued up to 10^9 cycles at 290 ± 10 V according to the procedure to be described below; no change in the loading curve was observed. Also, the center-point deflections were matched very well with the quasi 3-D model using σ_R=32 MPa, as seen in Fig. 2.15(a). They also matched the deflections predicted by the full 3-D model, as indicated by the dashed line in Fig. 2.15(a).

Given that σ_R=32 MPa, Device 3 has a notch stress of

$$\sigma_{notch} \approx 32 \text{ MPa}*(SR=0.889)*(WR=2.6)*(1.8)=133 \text{ MPa}. \qquad \text{(eq. 1a)}$$

The value of 1.8 comes from Fig. 2.7, Part I, and is the ratio of the maximum notch section stress to the average notch section stress. Upon actuation, the notch stress is enhanced by the factor $(1+2(A_{max}/L)^2)/\varepsilon_R$, according to Eq. (3), Part I. At 300 V, A_{max}=2.45 μm. Hence, the notch stress is increased by 47%, or $\sigma_{notch} \approx$196 MPa. This value is then a lower bound for the yield stress of this material, i.e., $\sigma_{ys} \geq$196 MPa.

Deflection curves for Device 2 also were reversible. Likewise, they were also matched very well by the quasi 3-D model, but now the best fit value of σ_R was much lower at 9.5 MPa as seen in Fig. 2.15(a). The measured deflection curves confirm that the applied stress in the gage section is nearly purely tensile. Fig. 2.15(b) shows Device 2 actuated at V_a=190 to 250 V by 20 V increments. Then center section is very flat and matches the model very well, as discussed in Part I, indicating that the gage section loading is purely tensile.

The excellent agreement between the measured and model curves in Fig. 2.15(b) is good evidence that σ_R is lower in Device 2 than in Device 3. This can be due to residual stress-induced yielding in the gage section, as described in Part I. However, we would then expect that actuation would induce further yielding of these devices, and that the unloading curve would not be the same as the loading curve. In fact, there is another important discrepancy that must also be addressed. That is, after deposition the measured value of biaxial residual stress is 300 MPa on monitor wafers. The uniaxial stress expected from the fixed-fixed beam measurements is $(1-\upsilon)$ times lower, or 200 MPa. Subsequent heating will likely increase this stress [26-28]. Device 2 reproducibly showed a line defect both optically and in SEM in the gage section, but Device 3 appeared to be undamaged. This helps explain why σ_R is lower in Device 2 than in Device 3, but does not explain why Device 2 behaves elastically in the first loading cycle.

To comprehend the data so far, it is imperative to more closely examine the sample processing. The TiN film remains on the Al/0.5% Cu film during release. This chemically protects the top side of the film, but its stress is very high and compressive, -1.2 GPa. Although this lowers the average tension in the film, it also induces bending. For further insight, samples were released and critically-point dried without first stripping the TiN. In Fig. 2.16(a), we see interferograms

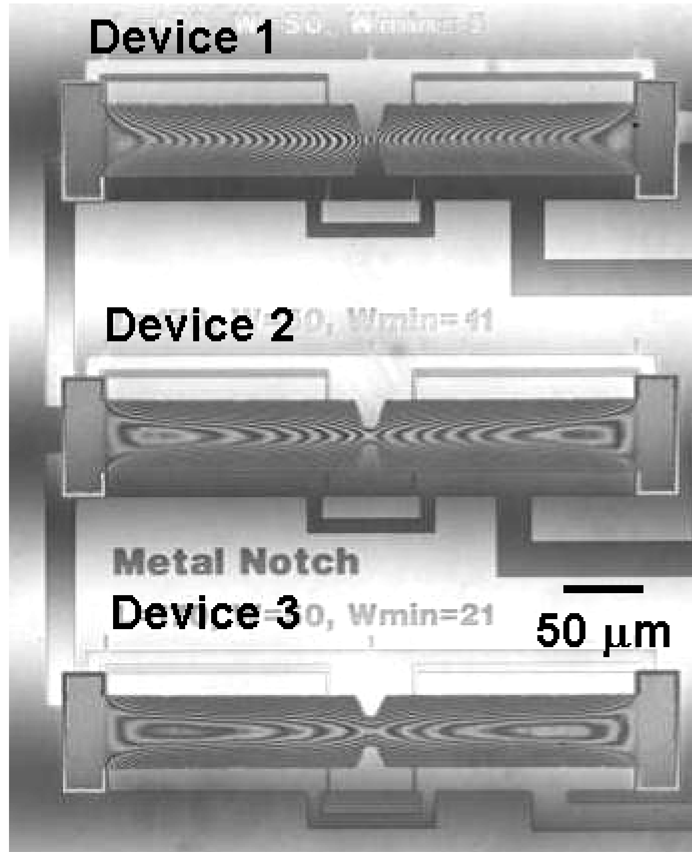

(a)

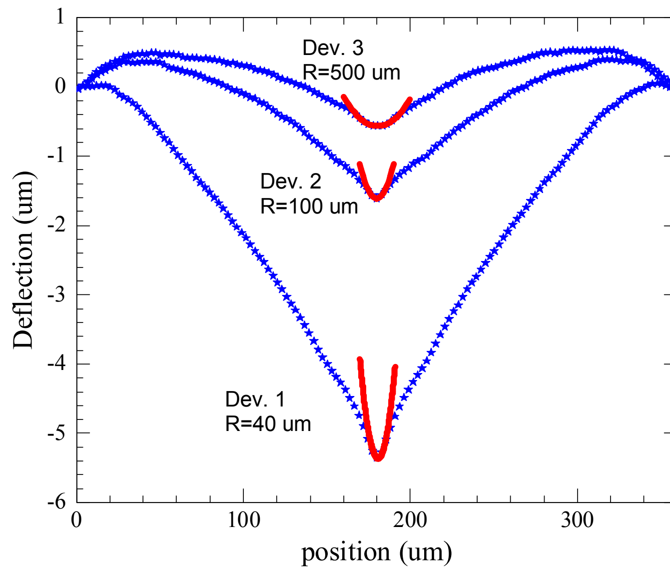

(b)

Figure 2.16 - (a) Interferogram of released notched devices *with* -1.2 GPa TiN *remaining* on top of film. (b) Notched device center-line flexures of structures with TiN remaining, along with curvature fits in notch sections. The TiN likely induces a bending stress that plastically deforms the notch region in Device 2. Removal of the TiN prior to release chemically attacked the film.

of Devices 1-3. Compared to samples shown so far which were virtually flat (with the TiN stripped), the deflected shape is complex. In Fig. 2.16(b), we see center-line deflection curves of these samples (along the x-direction) as obtained from PSI. Starting from the ends, we see that the deflections are first upwards and then downwards. At the center, the bending is severe, as indicated by best-fit solid lines. In the y-direction, the bending is downwards, as would be expected for a compressive film on top of a tensile film.

At R=100 μm as in Device 2, the bending stress is $\sigma_B = Et/2R$=210 MPa at the bottom of the film. This is only one contribution to the total stress, of course. To more fully understand the stresses, we implemented a finite element shell model in ANSYS to simulate the flexures of these complex unactuated bilayer structures. We are in the process of conducting a parametric study to match the measured flexures. In the model, we assume σ_R=-1.2 GPa as measured for the TiN film (we also use E=600 GPa for TiN), and allow σ_R and σ_{ys} to vary for the Al/0.5% Cu film. With σ_R=32 MPa, we could not begin to match the flexures of Device 3 or the fixed-fixed beam, independent of the value of σ_{ys}. However, with σ_R=125 MPa and σ_{ys}=125 MPa, we could approximate the behavior of both of these.

While more parametric study is clearly needed, we believe that even though the fixed-fixed beam and Device 3 behave elastically with the same residual stress, both were deformed plastically by the TiN. The plastic deformation is due primarily due to curvature in the y-direction. This is understood by considering the flexures of the fixed-fixed beam when TiN remains on top. It is nearly flat in the x-direction, but highly curved in the y-direction. The measured radius of curvature in the y-direction is R=62 μm. With $Et/2R$, σ_B=340 MPa if the flexure is purely elastic. However, from wafer curvature measurements for a film processed under similar conditions, the expected value for σ_{ys} is ~230 MPa for Al/0.5% Cu [28] at room temperature. We infer that the film yielded due to bending in the y-direction. Greater x-direction notch section bending will determine the degree to which stress is further relieved in Devices 2 and 3.

The bending due to the TiN during the stripping process helps us understand why Device 2 has a lower residual stress than Device 3. However, the reason why σ_R=30 MPa is not clear. As mentioned, we expect σ_R=200 MPa after deposition. There is good evidence that σ_R remains high, ~125 MPa, in the films with the TiN remaining. The Al/0.5% Cu film may have lower residual stress due to stress relaxation processes.

We have attempted making structures in which we stripped TiN from the Al/0.5% Cu film before release. One time, these samples broke through the notch section. A second time, they survived, but "pock marks" decorated the notch section, apparently due to stress-enhanced chemical etching there. Ideally, we would use a metal that is not attacked by the sacrificial etch, gold for example. We have also worked on a process with a polymeric sacrificial material that can easily be removed, but have found it difficult to successfully fabricate samples. Keeping in mind the difficulty of fabricating these samples, we continued testing to further assess the technique. The likelihood that these samples have already been subjected to plastic bending should be kept in mind in the following. The result of further study to keep the residual stress low is shown is discussed in the Appendix.

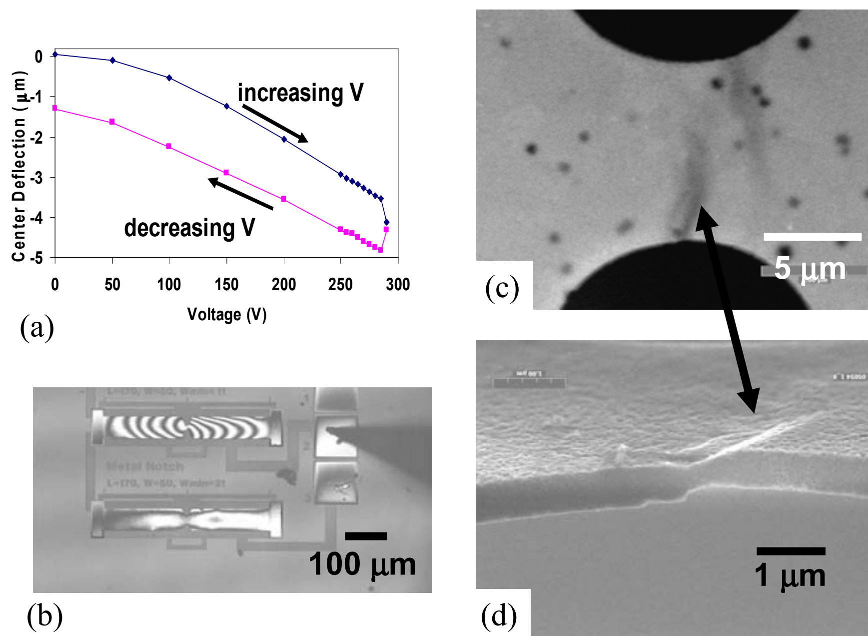

Figure 2.17 - Plastic deformation at V_a=290 V. (Device 2, σ_R=30 MPa). (a) Hysteretic center deflection. (b) Interferogram showing Devices 2 and 3 with at V_a=0 V. Device 3 exhibits minimal deflection while Device 2 exhibits permanent deformation. (c) SEM backscatter image indicating thinned regions. (d) Tilted SEM image (45°) indicating region thinned due to plastic deformation.

2.2.4 Load-induced plastic deformation and fatigue

In detail, the unloading curve of Device 2 had a deflection ~10 nm greater than the loading curve, but the following loading curve was the same as the previous if the maximum voltage was not too high. Assuming there is a high dislocation density in the notch region, this is consistent with dislocations bowing out when stress is applied, but then recovering reversibly as the stress is relaxed, as described by an anelastic Zener model [29].

If the applied voltage can be made large enough, we would expect a critical applied stress to induce an irreversible avalanche of dislocation motion. Usually, the limitation of keeping $V_a \le V_{max}$=300 V prevented the observation of such behavior. However, one such instance did occur, as illustrated in Fig. 2.17. A previous loading cycle up to 280 V exhibited the small hysteresis just described. For the cycle in Fig. 2.17(a), the loading continued up to V_a=290V. At this voltage, a large change in deflection was observed, and the unloading curve maximum deflection was over 1000 nm greater than the loading deflection. In Fig. 2.17(b), we see the interferogram of the unloaded device, where the residual fringes indicate permanent downwards deflection of the unloaded device, as well as a small twist of one side relative to the other. For comparison, the notched device just below in Fig. 2.17(b) shows how this device appeared

before this loading cycle. Darker areas extending across the width of the notch in the top view SEM of Fig. 2.17(c) indicate local thinning of this device in the gage section. In this image, small dark circles are also seen. They are locally thin areas that are not caused by this deformation as they are uniformly distributed throughout the film. These are perhaps caused by local attack during the release etch on the bottom of the film. Because the upper thin region runs between these circles and not through them, they do not necessarily play an important role in the deformation processes. A tilted view of the same sample in Fig. 2.17(d) shows that this area is indeed locally thinner and twisted in response to the plastic deformation.

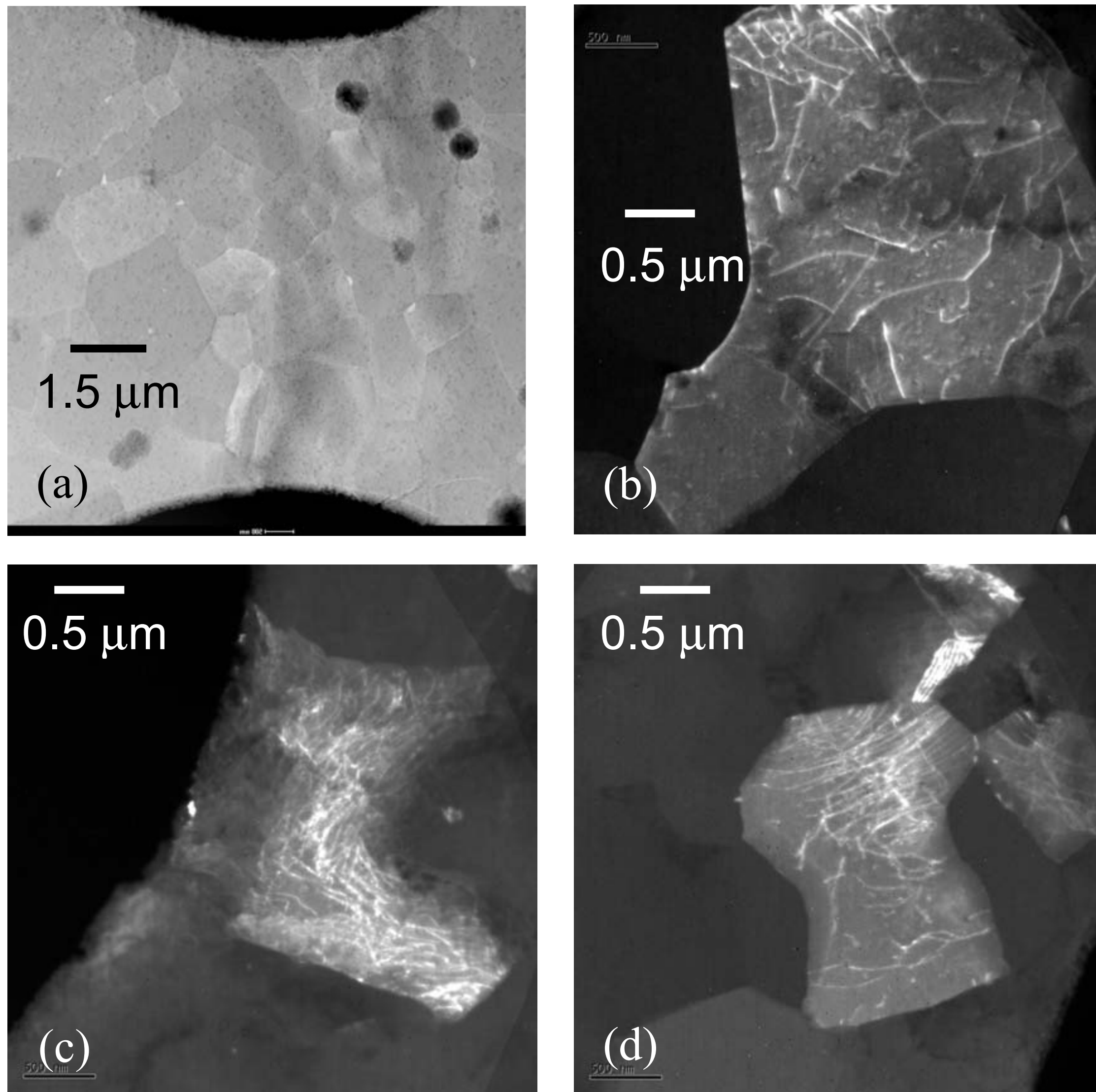

Figure 2.18 - TEM of notched region (a) Z-diffraction contrast (annular dark field STEM) showing darker areas corresponding to local thinning. (b) background dislocation density ~20 µm away from the notch region. (c) Grain at the notch edge (conventional dark field image). (d) grain away from edge in gage section

In Part I, Fig. 2.4 it is seen that once plastic deformation occurs, deflection curves overlap even if the residual stress was initially different. Furthermore, from Fig. 2.10 in Part I, we see that the

value of σ_{ys} used in the Quasi 3-D model is reasonable once significant deflection has occurred. From Fig. 2.17 in Part II, we indeed see that the plastic deformation extends across the notch region. Therefore, we can estimate for this particular structure, σ_{ys}=140 MPa. Other structures did not deform up to 300 V, and therefore typically σ_{ys}>150 MPa. It should be kept in mind that this value may be affected by the previous bending of the film due to the TiN. The observation that σ_{ys} is lower for Device 2 (~150 MPa) than Device 3 (>200 MPa) implies some strain softening has occurred in the gage section.

This same notched structure was removed from the substrate and placed on a TEM grid, and images are presented in Fig. 2.18. The Z-diffraction contrast (annular dark field STEM) of Fig. 2.18(a) shows that the grain size varies from about 0.5 to 1.5 μm, and also shows copper precipitates at the grain boundaries. Figs. 2.18(b)-(d) are conventional dark field images with a grain of interest illuminated by the imaging conditions. A region ~20 μm away from the gage section is shown in Fig 2.18(b). A background dislocation density of ~10^{13}/m^2 is seen there. At the gage section edge where the highest stresses and strains are expected, we see a far higher dislocation density. Somewhat further inside the gage section as in Fig. 2.18(d), the density remains very high. These images make it clear that dislocation motion is an important deformation mechanism in these samples.

Grain orientation mapping [20] showed a strong <111> preferred orientation with only a small in-plane orientation preference. Fig. 8 shows TEM results of energy dispersive X-ray (EDX) spectral imaging using multivariate statistical analysis [22]. Fig. 2.19(a) shows an area of interest, Fig. 2.19(b) shows the counts from the EDX analysis, and Fig. 2.19(c) shows the energy mapping according to the statistical analysis. $CuAl_2$ precipitates are seen at the grain boundaries, and Cu also remains in solid solution in the Al matrix. The distance between the hard $CuAl_2$ precipitates is large, on the order of the grain size, so it is not clear that there is any strengthening due to them. On the other hand, they may pin the grain boundary growth, and so keep the strength high due to a Hall-Petch effect. Fig. 2.19(a) shows a dappled-type appearance which may be due to local differences in the film thickness resulting from the growth process. These features are also visible in Fig. 2.17(d). Fig. 2.19(c) shows that some of these areas are associated with excess fluorine content, which may be a residual from the HF-based release etch.

When actuated repetitively, Device 2 always displayed fatigue. One can imagine many different fatigue tests. The thin film fatigue procedure we used is as follows. A large DC voltage V_{DC} was chosen (significantly below 300 V) and much smaller AC amplitude V_{AC}=10 V was superimposed. A fatigue operating frequency f, typically 10 or 20 kHz, was chosen. The resonant frequency is expected to be significantly above f. To guarantee that the fatigue loading was quasistatic, we performed stroboscopic measurements at some loading significantly below V_{DC}. The observed flexures were the same as in the case of static loading. For the first fatigue cycle, V_a was slowly ramped from 0 V to ($V_{DC}+V_{AC}$) V and back down to 0 V, and at selected voltages along the ramping cycle, the centerline deflection curve was measured. Next,

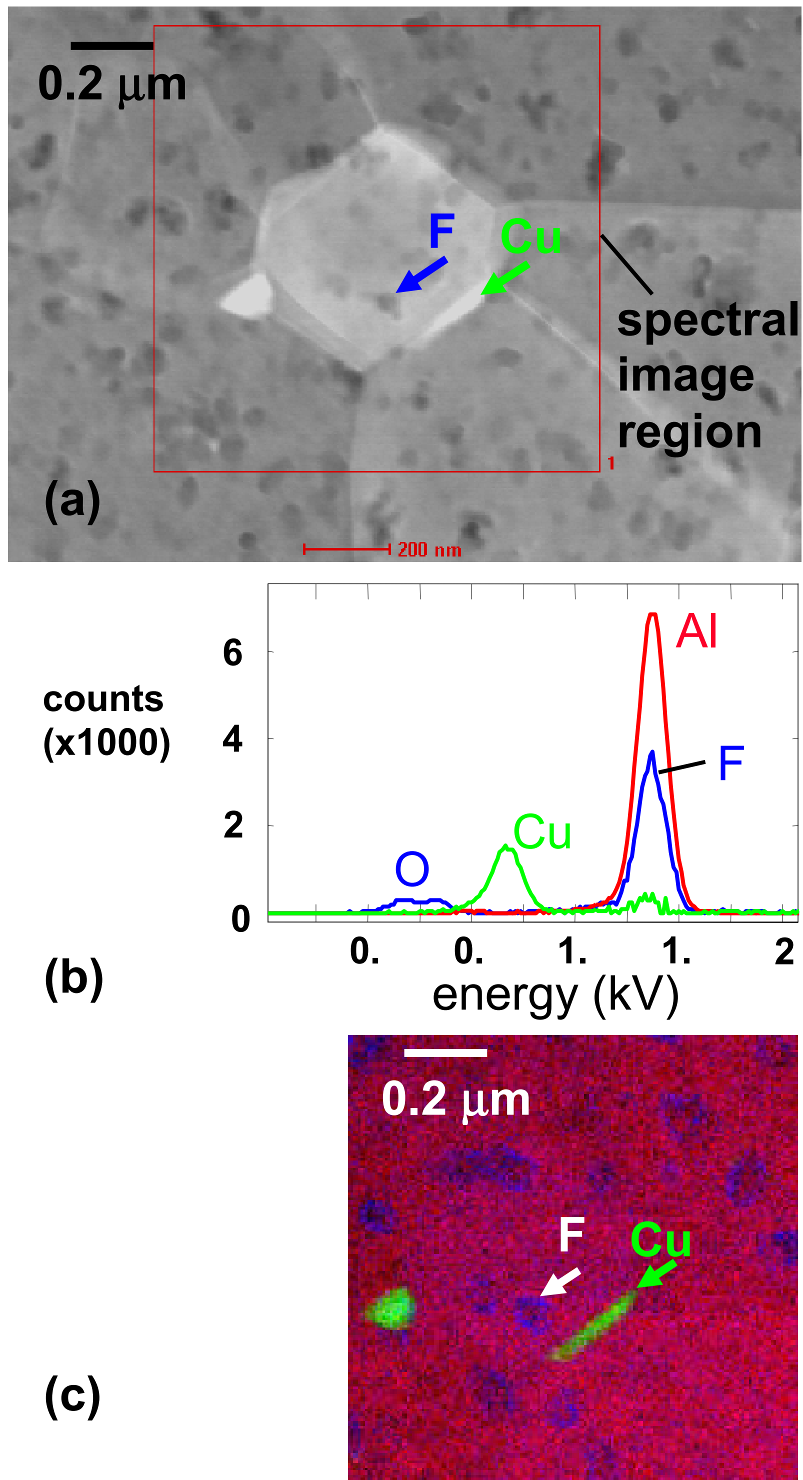

Figure 2.19 - TEM spectral analysis of Al film (a) STEM annular dark field image (b) Energy dispersive spectrum from region indicated in (a). (c) Energy map from spectral region in (a).

V_{DC} was applied, and then a sinusoidal signal at frequency f and amplitude V_{AC} was applied for 8 cycles. The ramping procedure, representing the 10th cycle, was again used to measure the deflections. Fatiguing was now repeated for 89 cycles and then the 100th cycle was measured. This procedure was continued up to 10^7 cycles. We shall call a fatigue test at a given value of V_{DC} a "V_{DC} fatigue test". At 10 kHz, each V_{DC} fatigue test was completed in approximately 20 minutes. Given that there was sample to sample variation, different V_{DC} fatigue tests were applied to the same sample.

As mentioned earlier, when this fatigue test was applied to Device 3, no change in deflections occurred even for $V_{DC}+V_{AC}=V_{\max}$=300 V. This is important not only because it sets a lower bound for the fatigue and yield strengths of the Al/0.5% Cu film, but also because it validates the test procedure. If there is fatigue, it must be due to the mechanical cycling and not due to a peculiar electrostatic charging or arcing mechanism. Typical results are shown in Fig. 2.20. For each value of V_{DC}, the center deflection data reported as relative to the first cycle of the particular V_{DC} test. The value of V_{DC} was changed randomly between V_{DC} fatigue tests, although the largest value of V_{DC} (250 V here) was run last. Hence, even though the test at V_{DC}=200 V was run after the test at V_{DC}=230 V, the fatigue mechanism had not saturated and some change in the relative deflection was still observed at the lower voltage. Of course, if the higher voltage is much greater than the lower voltage, no subsequent change was observed at the lower voltage.

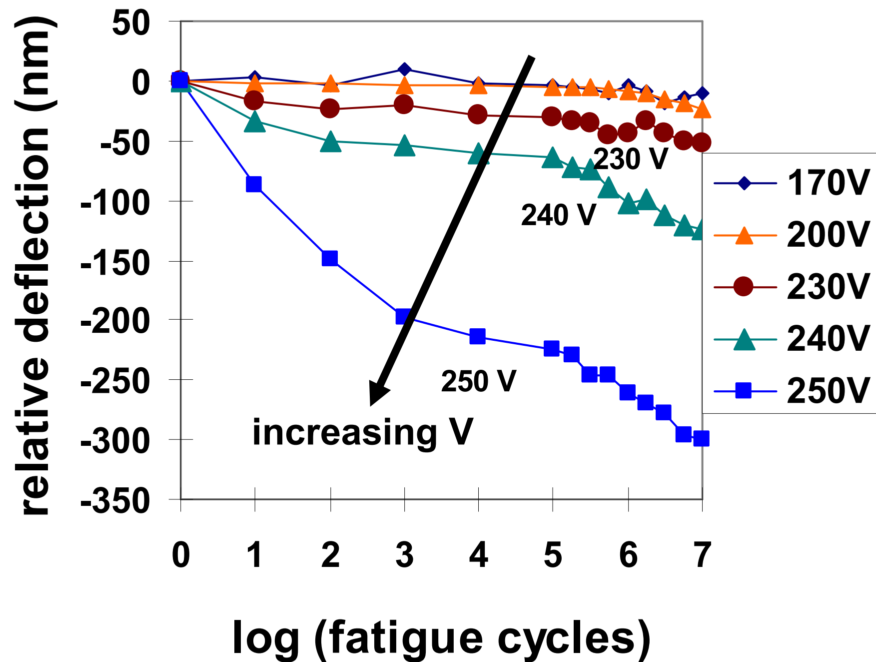

Figure 2.20 - Fatigue results

For comparable devices, if only one cycle is applied, there is no large hysteresis up to 280 V for a single cycle. Given that there is some fatigue even at 200 V, we see that the fatigue strength is significantly lower than the yield strength for this material. Referring to Fig. 2.4 of Part I, the average axial stress at 200 V is approximately 80 MPa, while it is 150 MPa at 300 V. Hence, the fatigue strength is approximately half of the yield strength for this Al/0.5% Cu film. In comparison, the fatigue strength of bulk Al is also lower than the yield strength by approximately a factor of 2 [30].

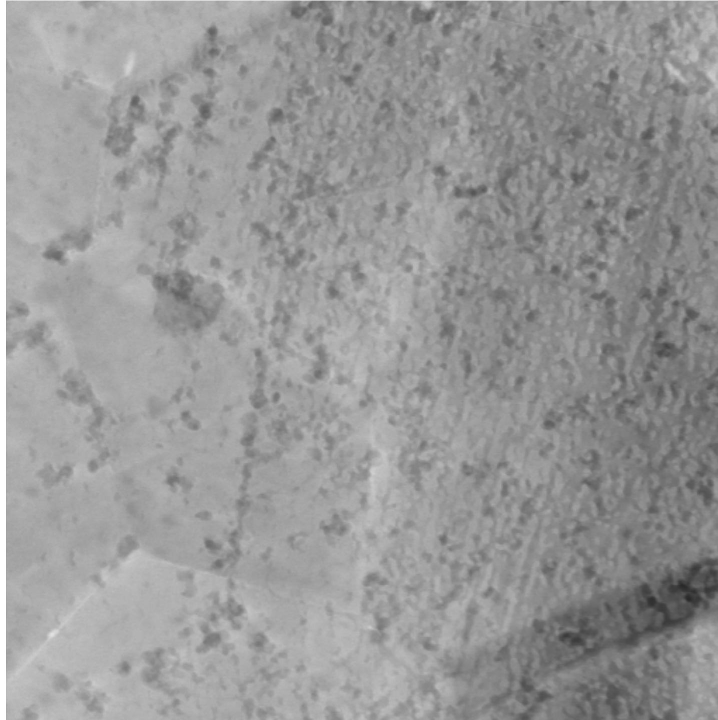

Figure 2.21 - Striations in STEM image of fatigued sample in notched regions.

TEM also revealed a high dislocation density in the notched region of a fatigued sample. STEM imaging showed distinct striations in the deformed region, as shown in Fig. 2.21.

Actuation of more severely damaged structures is discussed in Appendix C.

2.2.6 Summary & Conclusions

We have demonstrated a laboratory kit to directly and routinely apply large and controlled tensile strains to freestanding thin films. The samples we fabricated were simulated well by models developed in Part I, which considered flexures due to residual stress and electrostatic loading. By actuating microcantilevers, we found a value for Young's modulus E =73 GPa, in good agreement with the <111> texture of the Al/0.5% Cu film. For structures constrained at both ends, the experimental results indicated a third means for applying load that was not considered in Part I. This was due to the compressive TiN film, which induced complex bending

deformations in the structures. Processing methods to eliminate this bending were attempted but did not give good samples. This is an area that deserves further attention. Monotonic and fatigue loading were applied to notched samples that had been subjected to this one-time loading cycle. From this testing, we determined $\sigma_{ys} > 196$ MPa from Device 3 and $\sigma_{ys} \approx 150$ MPa from Device 2. For Device 2, the fatigue strength was about half the yield strength. TEM analysis indicated that deformation was dominated by dislocation interaction within the grains.

2.2.7 References for section 2.2

[1] D. T. Read and J. W. Dally, *A new method for measuring the strength and ductility of thin-films*, J. Mater. Res. **8** (7), 1542 (1993).

[2] D. T. Read, Y. W. Cheng, R. R. Keller and J. D. McColskey, *Tensile properties of free-standing aluminum thin films*, Scripta Mat. **45**, 583 (2001).

[3] W. N. Sharpe, B. Yuan and R. L. Edwards, *A new technique for measuring the mechanical properties of thin-films*, J. Microelectromech. Syst. **6** (3), 193 (1997).

[4] H. B. Huang and F. Spaepen, *Tensile testing of free-standing Cu, Ag and Al thin films and Ag/Cu multilayers*, Acta Mater. **48** (12), 3261 (2000).

[5] M. A. Haque and M. T. A. Saif, *In-situ tensile testing of nano-scale specimens in SEM and TEM*, Experimental Mechanics **42** (1), 123 (2002).

[6] H. J. Lee, P. Zhang and J. C. Bravman, *Tensile failure by grain thinning in micromachined aluminum thin films*, J. Appl. Phys. **93** (3), 1443 (2003).

[7] T. Tsuchiya, O. Tabata, J. Sakata and Y. Taga, *Specimen size effect of tensile strength of surface-micromachined polycrystalline silicon thin films*, J. Micromech. Microeng. **7** (1), 106 (1998).

[8] W. N. Sharpe, K. T. Turner and R. L. Edwards, *Tensile testing of polysilicon*, Experimental Mechanics **39** (3), 162 (1999).

[9] I. Chasiotis and W. G. Knauss, *A new microtensile tester for the study of MEMS materials with the aid of atomic force microscopy*, Experimental Mechanics **42** (1), 51 (2002).

[10] W. N. Sharpe, *Murray lecture - Tensile testing at the micrometer scale: Opportunities in experimental mechanics*, Experimental Mechanics **43** (3), 228 (2003).

[11] H. Kahn, R. Ballarini, R. L. Mullen and A. H. Heuer, *Electrostatically actuated failure of microfabricated polysilicon fracture mechanics specimens*, Proc. Roy. Soc. Lond. A. **455** (1990), 3807 (1999).

[12] M. A. Haque and M. T. A. Saif, *Microscale materials testing using MEMS actuators*, J. Microelectromech. Syst. **10** (1), 146 (2001).

[13] C. L. Muhlstein, S. B. Brown and R. O. Ritchie, *High-cycle fatigue of single-crystal silicon thin films*, J. Microelectromech. Syst. **10** (4), 593 (2001).

[14] T. Y. Zhang, Y. J. Su, C. F. Qian, M. H. Zhao and L. Q. Chen, *Microbridge testing of silicon nitride thin films deposited on silicon wafers*, Acta Mater. **48** (11), 2843 (2000).

[15] H. D. Espinosa, B. C. Prorok and M. Fischer, *A methodology for determining mechanical properties of freestanding thin films and MEMS materials*, J. Mech. Phys. Sol. **51**, 47 (2003).

[16] H. D. Espinosa, B. C. Prorok and B. Peng, *Plasticity size effects in free-standing submicron polycrystalline FCC -films subjected to pure tension*, J. Mech. Phys. Sol. **52**, 667 (2004).

[17] J. J. Sniegowski and M. P. de Boer, *IC-compatible polysilicon surface micromachining*, Annu. Rev. Mater. Sci. **30**, 297 (2000).

[18] M. B. Sinclair, M. P. de Boer and A. D. Corwin, *Long working-distance, incoherent light interference microscope*, Opt. Lett. **in press** (2005).

[19] J. E. Greivenkamp and J. H. Bruning, *Phase Shifting Interferometry,* in Optical Shop Testing; *Vol. Chapter 14 of* Second ed., edited by D. Malacara (J. Wiley & Sons, New York, 1992), pp. 501-598.

[20] R. P. Goehner and J. R. Michael, *Phase identification in a scanning electron microscope using backscattered electron Kikuchi patterns.*, J. Res. NIST **101** (3), 301 (1996).

[21] L. A. Giannuzzi and F. A. Stevie, *A review of focused ion beam milling techniques for TEM specimen preparation*, Micron **30**, 197 (1999).

[22] P. G. Kotula, M. R. Keenan and J. R. Michael, *Automated analysis of SEM X-ray spectral images: a powerful new microanalysis tool.*, Microscopy and Microanalysis **9** (1), 1 (2003).

[23] B. D. Jensen, M. P. de Boer, N. D. Masters, F. Bitsie and D. A. LaVan, *Interferometry of actuated cantilevers to determine material properties and test structure non-idealities in MEMS*, J. Microelectromech. Syst. **10** (3), 336 (2001).

[24] J. M. Gere and S. P. Timoshenko, *Mechanics of Materials*, 3rd ed. (PWS, Boston, 1990).

[25] M. S. Baker, M. P. de Boer, N. F. Smith, L. K. Warne and M. B. Sinclair, *Integrated measurement-modeling approaches for evaluating residual stress using micromachined fixed-fixed beams*, J. Microelectromech. Syst. **11** (6), 743 (2002).

[26] P. A. Flinn, D. S. Gardner and W. D. Nix, *Measurement and interpretation of stress in aluminum-based metallization as a function of thermal history*, IEEE Trans. Elec. Dev. **34** (3), 689 (1987).

[27] D. S. Gardner and P. A. Flinn, *Mechanical stress as a function of temperature in aluminum films*, IEEE Trans. Elec. Dev. **35** (12), 2160 (1988).

[28] R. Venkatraman, J. C. Bravman, W. D. Nix, P. W. Davies, P. A. Flinn and D. B. Fraser, *Mechanical properties and microstructural characterization of Al-0.5% Cu thin films*, J. Elec. Matls. **19** (11), 1231 (1990).

[29] S. P. Baker, R. P. Vinci and T. Arias, *Elastic and anelastic behavior of materials in small dimensions*, MRS Bull. **27** (1), 26 (2001).

[30] V. Gerold, B. A. Lerch and D. Steiner, *Fatigue behaviour of age-hardened alloy single crystals*, Zeitschrift fur Metallkunde **75** (7), 546 (1984).

[31] H. Kahn, R. Ballarini, J. J. Bellante and A. H. Heuer, *Fatigue failure in polysilicon not due to simple stress corrosion cracking*, Science **298** (5596), 1215 (2002).

3. STRESS DURING ISLAND COALESCENCE

3.1 Introduction

The effective mechanical properties of a material are highly dependent upon the residual stress state introduced during fabrication. This is particularly true for thin films where the residual stress can be a significant portion of the yield strength. Unfortunately, the evolution of intrinsic stress during deposition of Volmer-Weber thin films is quite complex and still highly debated [1,2,3]. The only growth regime where there is a consensus as to the mechanism is during island coalescence in the initial stages of film formation, where tensile stresses have been observed to exceed one gigapascal [4]. Conceptually, tensile stress is generated when adjacent islands initially touch one another, and then elastically deform to contact over a finite area in order to reduce the overall surface energy. Existing theoretical models for coalescence stress all

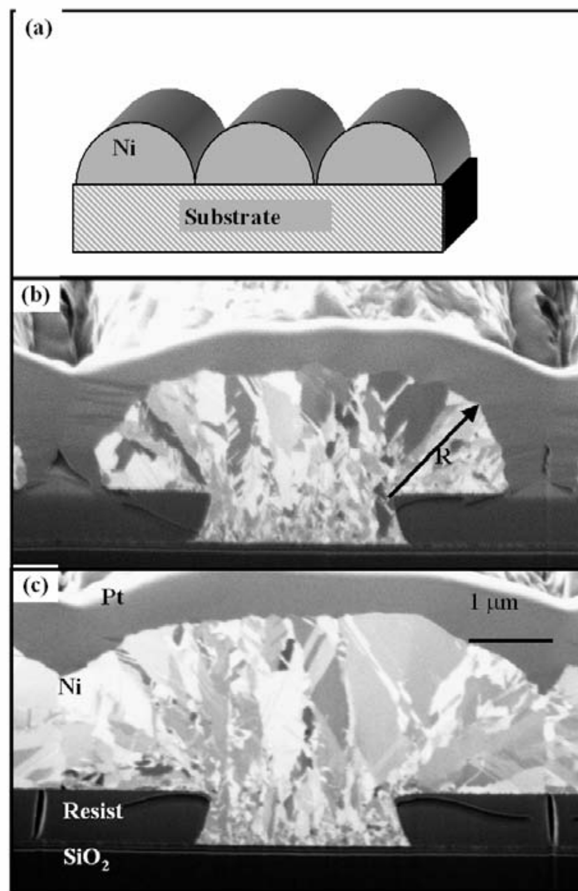

Figure 3.1 - (a) Schematic of an idealized cylindrical structure, (b) ion channeling focused ion beam (ICFIB) cross-section image of actual structure prior to coalescence, and (c) ICFIB image of the actual structure after coalescence. Note, the islands were coated after electrodeposition with Pt for processing in the FIB.

determine the mean tensile stress in mechanical equilibrium, as a function of island size and geometry at the moment of coalescence [1,4,5-8]. However, computational necessity requires use of highly simplified island geometries with uniform sizes and simultaneous coalescence. In real films, coalescence events are stochastically distributed in time and occur among islands with a broad range of sizes and shapes. Furthermore, multiple mechanisms for stress generation can be operating at the same time. As a result, it is not possible to quantitatively equate theoretical predictions for the tensile coalescence stress with existing measurements in stochastically nucleated films and a meaningful comparison is only obtainable when island geometries are systematically controlled.

3.2 Background and Experiment

In this section, we obtain both the functional dependence of mean tensile stress on island radius, and the absolute magnitude of the stress, by measuring stress changes during electrodeposition of Ni islands where the coalescence process was constrained via lithographically-defined island nucleation sites and selective-area growth (Fig. 3.1). We demonstrate that the experimentally measured coalescence stress is in good agreement with the predictions from the Hertzian contact model of Freund and Chason [7] and with two-dimensional finite element (FE) analysis. We have also determined that the initial coalescence stress was the minority component of the total stress created during the coalescence and planarization of the film. This determination lays the groundwork for future analysis of the post-contact stress generation process, which is considerably more complex (and beyond the scope of this paper).

Motivated by recent models for coalescence stress by Freund and Chason [7] and by Nix and Clemens [6], we chose to experimentally evaluate the “2-dimensional” coalescence geometry, where the islands were idealized as an array of parallel half-cylinders, as shown in Fig. 3.1a. In order to accomplish this, periodic trench arrays were patterned into a photoresist layer to expose a 1500 Å thick Au nucleation layer. This Au film was grown on a Ti adhesion layer on a thermally oxidized Si (001) substrate. Island size was controlled by varying the spacing of the trenches, while keeping the nominal trench pitch-to-width ratio (d_{pitch}/d_{trench}) = 2.65. The effective cylinder radii, R, ranged from 0.3 μm to 26 μm. Ni films were potentiostatically electroplated from an additive-free Ni-sulfamate bath at 40°C. Prior to electrodeposition of the coalescence samples, the bath was conditioned at 10mA/cm^2 for 4 hours to remove trace ionic contaminants such as Fe and Co. Additionally, ultra-high purity N_2 was bubbled through the bath for a minimum of 24 hours, which increased run-to-run reproducibility. The plating efficiency was determined by comparing the Faradic current to thicknesses measured using Rutherford backscattering spectrometry. During deposition, the substrate curvature induced by thin-film stress was measured using laser deflectometry [3], with the wafer clamped in a cantilever configuration. Because film thicknesses were often an appreciable fraction of the substrate thickness, the usual Stoney’s equation did not hold, and the following relation for curvature (κ) was used [9]:

$$\kappa = \frac{6h_f\sigma}{h_s^2}\left[\frac{1+H}{1+HY\left(4+6H+4H^2\right)+H^4Y^2}\right], \qquad \text{(eq. 3.1)}$$

where H is the ratio of the film thickness (h_f), to the substrate thickness (h_s), σ is the mean film stress, and Y is the ratio of the film modulus to the substrate modulus. Young’s modulus was used rather than the biaxial modulus due to the uniaxial loading geometry used here.

Figures 3.1b and 3.1c demonstrate the selective lateral growth that can be obtained using electrodeposition. At coalescence, the islands were not true half-cylinders, as shown in Fig. 1b-c, and we will account for this in our analysis. Figure 3.2 shows the measured evolution of "stress-thickness", σh_f, calculated from curvature using eq. 3.1. In the figure, Ni was electrodeposited into an array of trenches that yielded nominally 4.2 μm radius cylinders (with the radius as defined in Fig. 3.1b). The first rise in the tensile stress was the result of random Ni nucleation and coalescence within the trenches themselves to form the Ni lines. The second tensile rise was due to the coalescence of adjacent cylindrical islands, and was the stress change that we analyzed. In order to do this, we found it necessary to differentiate between the stress created during the initial coalescence event and the subsequent stress created as the film evolved from cylinders towards a planar surface. The challenge is to determine which part of the curvature change is associated with the first contact of the half-cylinder array. To accomplish this, we examine the behavior of the plating current in further detail.

During potentiostatic deposition, plating current is linearly proportional to the surface area. Therefore, since the surface roughness of a film is maximum at moment of coalescence the must be a corresponding maximum in the plating current at the same moment. To quantify this we developed a simplified geometric model that predicts the evolution of the surface area and in turn, the deposition current of a cylindrical geometry. Referring to the geometry shown in Fig. 3.3, the surface area prior to coalescence is given by the sum of the areas of two quarter cylinders and the trench region. Enlargement of the structure is always radially outwards since the growth

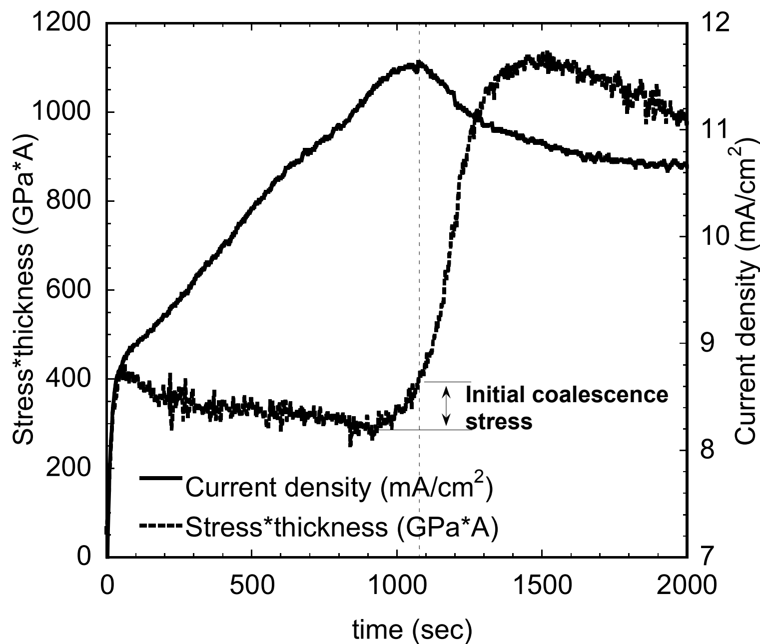

Figure 3.2 - Stress-thickness vs. time plot for a 4.2 μm radius coalescence sample showing a measured change in stress*thickness during coalescence of 96 GPa*Å.

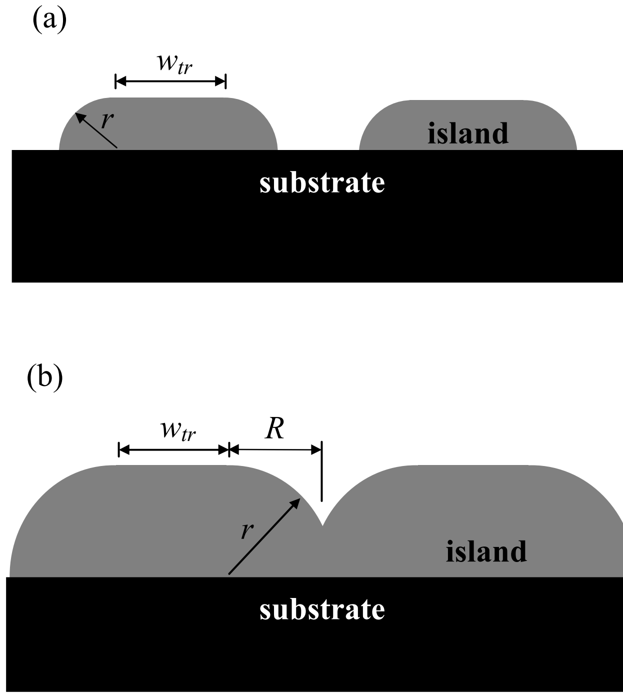

Figure 3.3 - Idealized cross-sectional geometry used in current evolution model, (a) prior to coalescence, (b) post-coalescence.

direction is normal to the free surface during electrodeposition (Fig 3.3a). The total plating current (I_{tot}) into the sample prior to coalescence is then give by:

$$I_{tot} = (\pi r + w_{tr})\frac{dr}{dt}\frac{dq}{dV}n_{tr}w_s\,, \qquad \text{(eq. 3.2)}$$

where r is the island radius, n_{tr} is the number of trenches across the sample, w_s width of the sample in the direction orthogonal to the lines, w_{tr} is the width of the trench, $\frac{dr}{dt}$ is the deposition rate, and $\frac{dq}{dV}$ is the plating efficiency, measured to be 3.7x10^7 mC/cm^3 from RBS thickness measurement of unpatterned films. After contact, the islands asymptotically approached a planar surface as the half-cylinder surfaces overlap (see Fig. 3b), with the total current being equal to:

$$I_{tot} = \left[2r\cdot\arcsin\left(\frac{R}{r}\right) + w_{tr}\right]\frac{dr}{dt}\frac{dq}{dV}n_{tr}w_s\,, \qquad \text{(eq. 3.3)}$$

where, R is the radius of the islands when they coalesced.

Figure 3.4 is an overlay of the predicted (dashed line) and measured (solid line) currents for a single representative experiment. The only fitting parameter was the position of the maximum current, which was required because the initial plating rate is larger than the steady-state value while the diffusion zone is being established. This initial super-linear increase in deposition rate causes the current peak to occur earlier than is predicted using a constant deposition rate. In

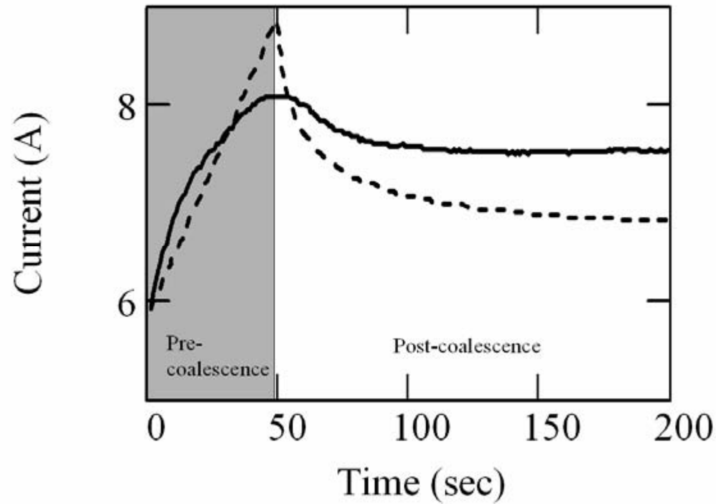

Figure 3.4 - Overlay of current predicted from geometric model (dashed line) with the current measured during deposition (solid line).

comparing the predicted and measured current behavior, two main features are apparent: (1) rounding of the measured peak current and (2) a higher asymptotic current. Rounding of the peak in the measured current likely results from a combination of effects, including variation in the thickness of the photoresist, variation in the trench width across the samples, and surface roughness. The difference between the measured and predicted asymptotic currents is most likely the result of the increased surface area due to surface roughness. For the sample used in Fig. 4 the difference between the asymptotic currents was ~12% where as AFM measurements of the surfaces indicate the surface area was ~6% larger then a planar film, which is reasonable considering the reduction in the measures surface roughness due to the finite radius of curvature of the AFM tip.

Based on the foregoing analysis leading to Fig. 3.4, we assign the maximum in the plating current to the point of maximum surface area of the film, and therefore to the moment of initial contact and coalescence. Thus, as shown in Fig. 3.2, we extract the stress change associated with initial coalescence by taking the deviation in σh_f from the background level to the point of maximum current. Surprisingly, this only accounts for a small fraction of the total tensile rise observed in the data of Fig. 3.2, and this is true for all the growth experiments we have performed. We believe that the remainder of the tensile rise was the result of continual coalescence of the islands during subsequent deposition and planarization of the film. Our data clearly demonstrates that the majority of the tensile stress was actually the result of post-contact coalescence processes. Similar behavior has been observed by Sheldon et al. during chemical vapor deposition of unpatterned diamond films and was attributed to the continual coalescence of faceted grains [10]. Our results suggest that this behavior is more general in as much as we observe continual coalescence occurring in non-faceted metal islands across a range of length scales. One common aspect may be the relatively low mobility growth conditions in both the

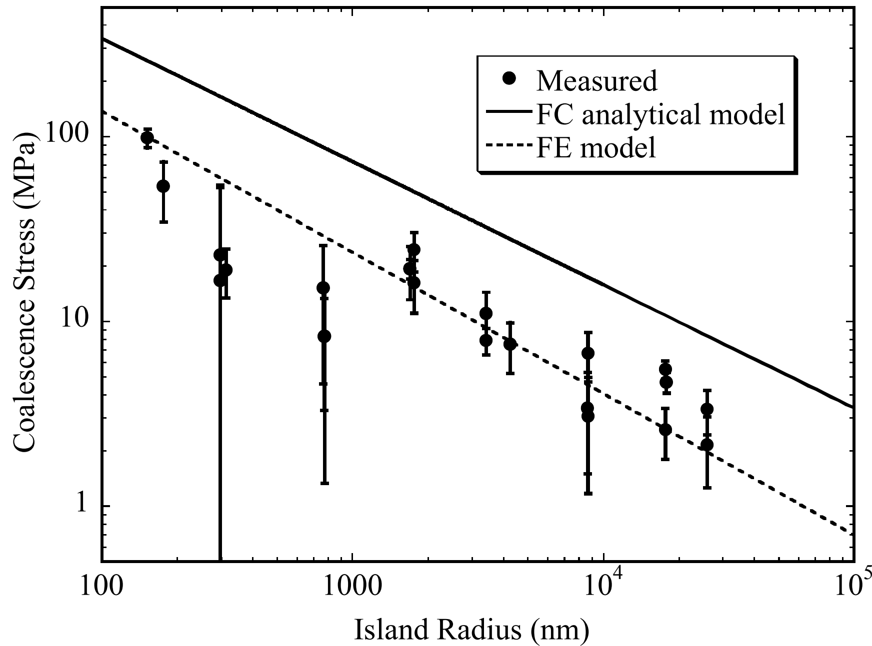

Figure 3.5 - Plot of measured, FC, and FE calculated island coalescence stress as a function of radius. Both models assume perfect cylinders coalescing and therefore should overestimate the coalescence stress.

diamond CVD case and in our room-temperature Ni growth. The detailed understanding of continual coalescence requires significant additional experimentation and analysis, which will be the subject of future work.

Figure 3.5 summarizes our key results where we have obtained for the first time the measured stress associated with initial island coalescence as a function of the island contact radius. This volume-average stress was obtained by dividing the total change in stress-thickness due to coalescence, as defined above and in Fig. 3.2, by the mean thickness determined from the plating current [8,11]. On a log-log plot the data exhibits a roughly linear increase in mean stress with decreasing island radius. There is some negative deviation from linear behavior at smaller radii, which was typically associated with depositions where the very poor signal-to-noise ratio created unacceptably large error in the measured stress. Additionally, AFM measurements indicate that the *relative* roughness on surfaces of the half-cylinders was significantly larger for cylinder radii below 1 μm (Fig. 3.6). Surface roughness decreases the contact area between islands, which reduces the measured stress. Therefore, in the following analysis we shall only consider samples with radii larger than 1 μm for quantitative comparison with the analytical and FE models. Clearly, it would have been better if we could directly compare theory and experiment down to at least the 0.1 μm island sizes available using holographic lithography, and this will be addressed in future work by using materials other than Ni. We nonetheless emphasize that there is no

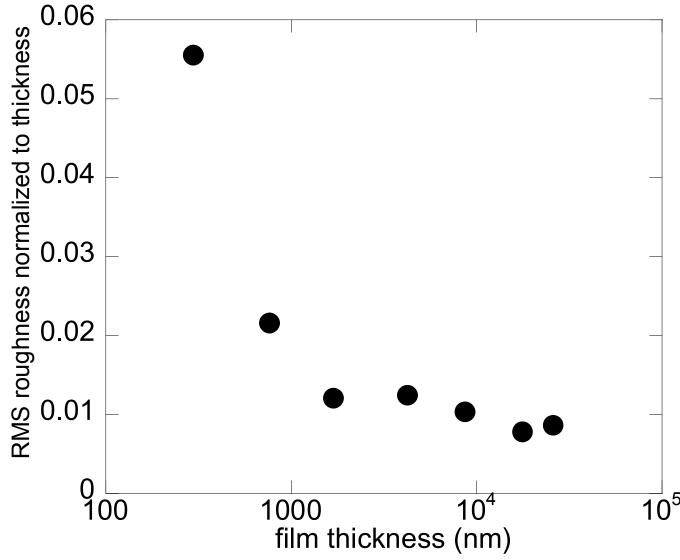

Figure 3.6 - RMS roughness surface roughness of planar films measured using *ex-situ* AFM. The % RMS roughness decreased significantly and stabilized at ~ 1 micron of thickness.

inherent limit to extrapolating our comparison of theory and data to at least an order of magnitude smaller length scales. Even at 0.1 μm, the number of atoms per unit cross-sectional area is large enough that both continuum mechanics and continuum descriptions of surface energy remain valid.

The Freund and Chason model (FC) [7] uses Hertzian contact theory to determine the volume average stress (σ_{avg}) created within the islands as a function of the initial coalescence geometry of the island, e.g. blocks, cylinders, or hemispheres. Our experiments used cylinders with their axes parallel to the substrate, whereas FC used cylinders with their axis of symmetry normal to the substrate. This required a slight modification to the FC model as follows.

According to FC the total contact force per unit length (P) for the general case for cylinder contacting under plane strain along their axis of symmetry is given by:

$$P = p(\pi R\bar{E})(\zeta / R)^{2/3}, \qquad \text{(eq. 3.4)}$$

where p is the normalized contact force for cylinders and was determined by FC to equal 0.3, $\bar{E}$ is the plane strain modulus, $\zeta \equiv \frac{2\gamma}{\pi\bar{E}}$, and γ is the difference between the surface energy and half the grain boundary energy, i.e. the energy of the interface between the coalesced islands. The volume average stress is found by dividing the contact force per unit area by the mean film height for the modified geometry, which for a half cylinder is given by $\pi R/4$. Therefore, the volume average stress for a cylinder with its axis parallel to the substrate is:

$$\sigma_{avg} = 1.2\bar{E}\left(\frac{2\gamma}{\pi\bar{E}R}\right)^{2/3} = 0.888\bar{E}^{1/3}\left(\frac{\gamma}{R}\right)^{2/3}. \qquad \text{(eq. 3.5)}$$

This volume average stress, for half cylinders coalescing with their axis of symmetry parallel to the substrate, is twice that of cylinders with their axis perpendicular to the substrate. However, the power-law dependence of the predicted stress with island radius is the same for both geometries and equal to –2/3.

As shown in Fig. 3.1, the true geometry of the coalescing islands used in these experiments was more complex than the idealized analytical model due to the additional block of material in and above the trench. This had two effects on the volume average stress: First, it decreased the number of boundaries formed per unit area causing an overall decrease in the magnitude of the volume average stress. Second, the material above the trench acted as a "shear-lag zone" that transmitted the stress to the substrate, which acted to increase the volume average stress. 2-D FE modeling was used to quantify the effect of the material in and above the trench on the functional dependence of the volume average stress on island radius. The details of using FE to model island coalescence have been presented elsewhere [12]. Two geometries were compared using FE modeling: ideal half cylinders (Fig. 3.1a) and the actual island structure (Fig. 3.7). We found no significant variation in the functional dependence of stress on island radius (slope of -0.76 to –0.74) as a result of the different geometries and only a slight decrease in the magnitude of the stress with the addition of the trench and photo-resist. This result supports the use of a simplified geometry (pure cylinders) in the FC model. In calculating the theoretical stress shown in Fig. 3.5 no fitting parameters were used and both the FE and FC models were calculated assuming γ =1.85J/m^2 [13], and $\bar{E}$=200 GPa (the value measured in our films using nanoindentation). It should be noted that both the FE and the analytical models predict the maximum possible stress created during initial coalescence and any error in γ or $\bar{E}$ would result in a shift in the magnitude of both curves and can not be used to explain the difference between the results. Mechanisms such as incomplete coalescence due to surface roughness or localized yielding will always act to reduce the observed stress. Additionally, the slight difference in the

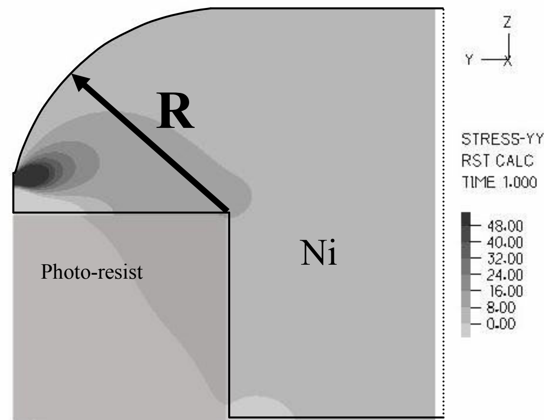

Figure 3.7 - In-plane stress (σ_{yy}) fields in the full structure as calculated from FE model. Darker color indicates stronger tensile stress.

exponents between the FE (-3/4) and the Hertzian models (-2/3) was likely the result of the lack of an exact solution for the force distribution in contacting cylinders used in the Hertzian model [7,14].

Figure 3.5 compares the calculated coalescence stress for the FE (dashed line) and the FC (solid line) models with the experimentally measured initial coalescence stress. In comparing theory vs. data, we consider the power-law behavior and the absolute stress magnitudes independently, because the magnitude depends on materials properties whereas the power-law behavior is solely a function of geometry. The observation that the stress magnitudes of the measured data and FE results are similar is fortuitous, because there is considerable uncertainty in the surface and grain-boundary energies used in the models and because of potential surface roughness effects. However, since the observed stress was of a similar magnitude to the predicted stress, which is an upper bound, it is reasonable to conclude that any reduction in the initial coalescence area by surface roughness was minimal over the range of radii considered. More definitively, Fig. 3.5 shows that the power-law behavior predicted by both the FE and the FC models is within the experimental variation of the measured coalescence stress versus island radius for samples larger than 1μm (-0.70 ± 0.25). Furthermore, the data lie outside the predicted behavior for both slope and magnitude for the 1D and 3D coalescence geometries in the FC model. *Therefore, the analytical models capture the dominant physical mechanisms underlying the generation of tensile stress during island coalescence.*

3.3 Conclusion

In conclusion, using lithographically defined nucleation and selective area growth via electrodeposition, we have obtained the first meaningful comparison of experimentally measured stresses due to island coalescence with the stresses predicted by theory. These experiments yielded two main results: First, the measured initial coalescence stress had a functional behavior similar to that of the FC and FE models for coalescence stress. From this we conclude that both models correctly account for all of the dominant physical mechanisms active during the initial coalescence of islands. Second, the majority of the stress associated with island coalescence occurred during planarization of the films, not during the initial contact of the islands. This striking result had not been previously recognized in unpatterned metal films due to the inability to differentiate the stress created at the initial contact from that created during planarization.

3.4 References for Section 3

[1] R. Koch, J. Condens. Matter 6, 9519 (1994).

[2] J. A. Floro, S. J. Hearne, J. A. Hunter, P Kotula, E. Chason, S. C. Seel, and C. V. Thompson, J. Appl. Phys. 89, 4886 (2001).

[3] J. A. Floro, E. Chason, and S. R. Lee, Materials Research Society Symposium Proceedings, 405, 1996, (381).

[4] R. Abermann and P. Martinz, Thin Solid Films 115, 185 (1984).

[5] R. W. Hoffman, Thin Solid Films 34, 185 (1976).

[6] W. D. Nix and B. M. Clemens, J. Mater. Res. 14, 3467 (1999).

[7] L. B. Freund and E. Chason, J. Appl. Phys. 89, 4866 (2001).

[8] Allison Suh, Ning Yu, Ki Myung Lee, Andreas A. Polycarpou, and H. T. Johnson, J. Appl. Phys. 96, 1 (2004).

[9] L. B. Freund, J. A. Floro, and E. Chason, Appl. Phys. Lett 74, 1987 (1999).

[10] B. W. Sheldon, K. H. A. Lau, and A. Rajamani, J. Appl. Phys. 90, 5097 (2001).

[11] L. B. Freund and S. Suresh, Thin Film Materials (Cambridge University Press, Cambridge, 2003), Vol. 1, p.206.

[12] S. C. Seel, C. V. C.V. Thompson, S. J. Hearne, and J. A. Floro, J. Appl. Phys. 88, 7079 (2000).

[13] J. P. Hirth and J. Lothe, Theory of Dislocations , 2nd edition (Wiley, New York, 1975), p.839.

[14] K. L. Johnson, Contact Mechanics, 1st edition (Cambridge University Press, Cambridge, 1985), Chap. 4.2, p.99.

4. STRESS DURING ELECTRODEPOSITION

4.1 Stress during Ni electrodeposition

4.1.1 Introduction

Thin films typically grow under non-equilibrium conditions, which often result in significant levels of intrinsic stress. For over a century, the deleterious effects caused by these stresses have sparked both scientific interest in the mechanisms that induce stress, and engineering efforts to control stress. The earliest published work on stress evolution during thin film growth was by Mills in 1877 [1]. Mills used a glass thermometer bulb coated with chrome to act as a cathode for electrodeposition. The recorded change in the height of the mercury in the thermometer was attributed to eletrostriction, i.e. stress. This pioneering work demonstrated that stress evolution was measurable in real-time during thin film growth and that the resultant stresses were non-trivial. Since then, there has been considerable work on characterizing different electroplating solutions with the intent of producing low stress deposits. However, in most electroplating systems the fundamental mechanism(s) inducing intrinsic stress have not been identified. One such system is electrodeposited Ni, where it has been empirically determined that electrodeposition from bath chemistries based on Ni sulfamate induces compression, whereas Ni sulfate-based baths require the addition of "stress-reducers" to induce compression [2].

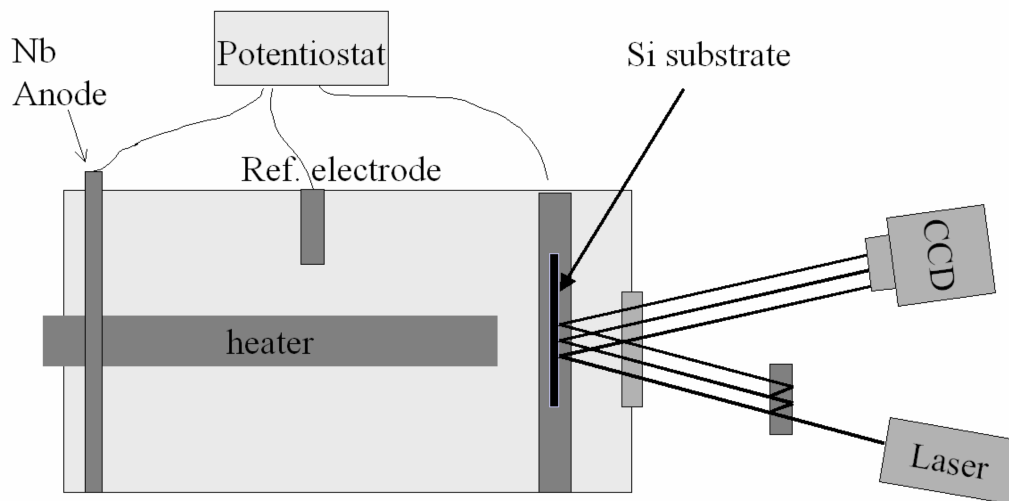

Figure 4.1 - Schematic of electroplating cell with *in situ* MOSS system.

This section focuses on the stress generation mechanism(s) that produce compressive stress during electrodeposition of Ni from additive-free sulfamate-based baths. We investigated three sources for the compressive stress that could be active during electrodeposition of Ni: hydrogen

or other impurity incorporation, capillarity stress, and a chemical potential gradient driven atom incorporation model. Of these, only the last could not be discounted as the dominant mechanism creating the observed compressive stress.

4.1.2 In-situ stress measurements

Stress measurements were taken during electrodeposition by incorporating a multi-beam optical stress sensor (MOSS) into an electroplating cell, schematically shown in Figure 4.1. MOSS determines the stress-thickness product of a film by measuring the change in curvature of a substrate, which is obtained from the relative change in spacing between multiple laser beams reflected from a film / substrate composite. This technique has been described in detail elsewhere [3]. Due to the requirement of electrical contact to the wafer for electroplating, the sample was clamped on a single side to form a cantilever. Curvature data was converted to stress-thickness using Stoney's equation [4]:

$$\kappa = \frac{6\sigma_f h_f}{M_s h_s^2}, \qquad \text{(eq. 4.1)}$$

where σ_f is the stress of the film, $h_{f(s)}$ is the film thickness (substrate), κ is the curvature of the substrate, and $M_{f(s)}$ is the bi-axial modulus of the film (substrate). When the stress-thickness product is plotted versus thickness, the slope gives the instantaneous stress in the monolayer of film being deposited, plus the incremental relaxation in the existing layer [5]. We have adopted the convention that a positive slope is tension and negative slope is compression.

All Ni films were electrodeposited on substrates cleaved from a thermally oxidized Si(100) wafer capped with electron-beam deposited Ti/Au films, 25 nm and 150 nm thickness, respectively. The substrates were cleaned prior to being placed into the electrodeposition-stress cell by rinsing the Au surface with H_2SO_4:H_2O_2 (4:1) for 10 seconds followed by rinsing in de-ionized water for 1 minute. This procedure was repeated until the Au was hydrophilic, indicating a clean surface. The electrodeposition-stress system contained nominally 1.5 liters of plating solution and was fabricated from polyvinyl-difluoride to prevent contamination of the solution at the elevated temperature (40°C to 55°C) required for Ni electrodeposition. When the plating system was not in use, the bath was continuously filtered through a 0.5 μm filter and ultra-high purity nitrogen was bubbled though the plating solution to remove oxygen.

The Ni was electrodeposited using a surfactant-free sulfamate bath (1.36 M/L Ni sulfamate, 0.72 M/L boric acid, 17.5 MΩ DI water @ a pH of 3.8). Prior to the initial use of the bath, the bath was run at 10mA/cm^2 with a 10cm^2 cathode for 4 hours to remove trace ionic contaminants such as Fe and Co. Additionally, we determined that it was necessary to de-aerate the bath by bubbling ultra-high purity N_2 through it for a minimum of 24 hours in order to obtain repeatable stress profiles. Finally, all Ni films were electrodeposited using a three-probe technique with a saturated Hg/Hg sulfate reference electrode (0.64 V versus a standard hydrogen electrode) and a non-soluble Nb grid as the anode. Unless otherwise stated, all potentials quoted in the remainder of this work will be with respect to a standard hydrogen electrode using the aforementioned conversion.

Figure 4.2 is a series of stress-thickness plots taken during galvanostatic electrodeposition of Ni from the sulfamate bath. The stress during the first 100 nm of film growth was found to be independent of deposition rate and temperature, with a tensile stress of nominally ~1 GPa. This behavior was likely the result of lattice mismatch between the Ni film and the Au substrate. Similar behavior has been previously reported by Möller *et.al* [6]. Möller used an *in-situ* scanning tunneling microscopy (STM) to study the nucleation of Ni onto Au (111) during

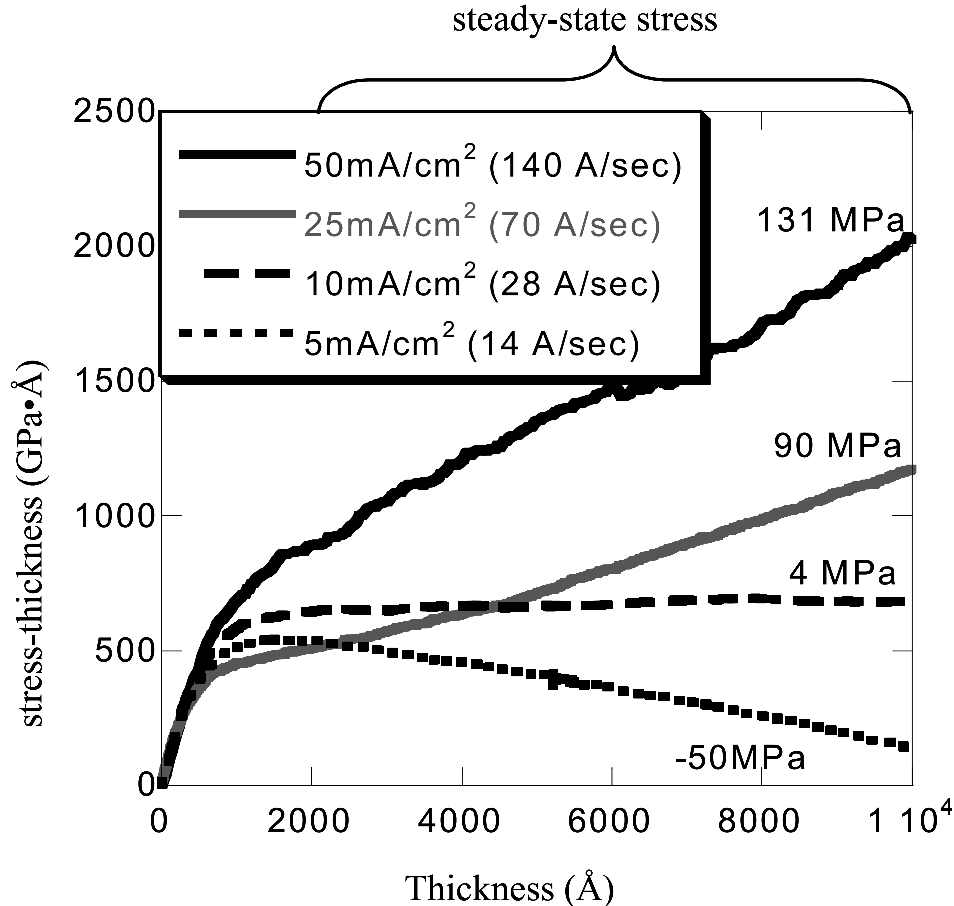

Figure 4.2 - Overlay of stress-thickness versus thickness plots taken during electrodeposition of Ni onto a Au substrate using a Ni sulfamate-based electroplating bath @ 40°C.

electrodeposition and determined that during the initial stages of growth the Ni was semi-coherent with the to Au substrate.

For films thicker than 100 nm we observed that the instantaneous stress became more compressive with decreasing current density. We determined that, provided the critical thickness for relaxation was not exceeded, the instantaneous stress level remained constant to thicknesses in excess of 50 μm. Fig. 4.3 is a plot of the steady-state instantaneous stress, σ_s, for a set of samples thicker than 1000 Å. It was found, that σ_s exhibited a remarkably consistent dependence on deposition rate, varying from –500 MPa to +500 MPa as deposition rate increased.

Additionally, the change from tension to compression during deposition (see Fig. 4.2) was the result of a compressive stress generation mechanism rather than a relaxation process, since relaxation should always reduce the magnitude of the volume average stress towards zero, i.e. zero net curvature. Another observation from Fig. 4.3 is that there was no significant dependence of the steady-state stress on the temperature, ranging of 40°C to 55°C in the sulfamate bath used in our experiments. This result differs from those in the literature, where the stress in Ni deposited from sulfamate baths was shown to have temperature dependence [7-12]. This difference is likely the result of the presence of Cl^- in all of the baths used in these references, because Cl^- induces significant stress into Ni and may result in the previously observed temperature dependence [11, 12]. Further investigation is required to elucidate the mechanism(s) that induce the temperature dependence to the steady-state stress when Cl^- is present in a sulfamate-based bath.

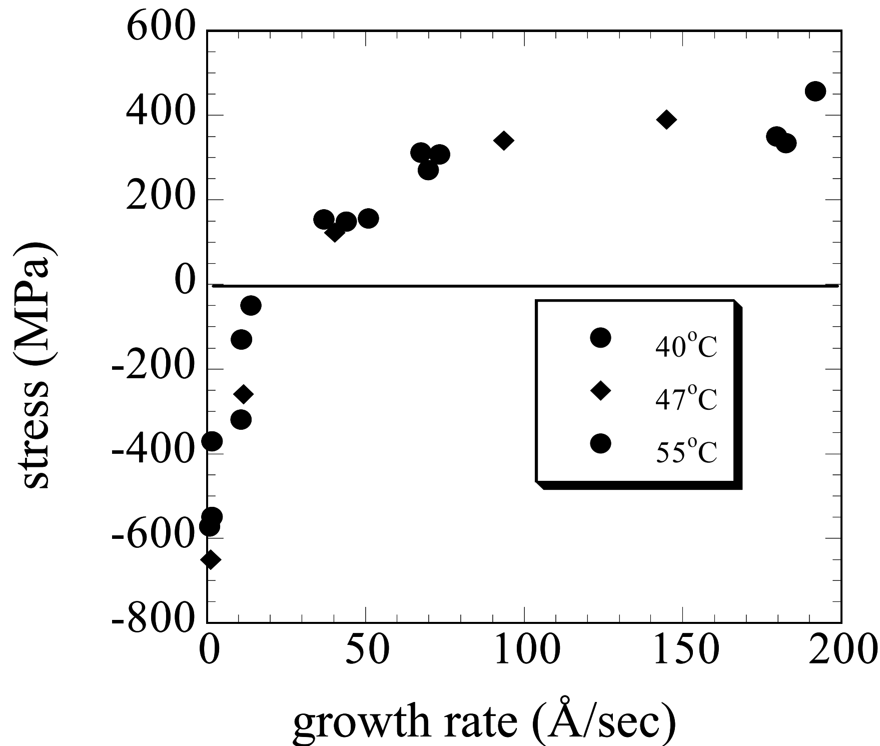

Figure 4.3 - Instantaneous stress during the steady-state stress versus deposition rate for Ni sulfamate-bath plated at 40°C, 47°C, 55°C.

The effect of deposition rate on steady-state stress can also be demonstrated by changing the rate dynamically during a single electrodeposition. Figure 4.4 shows real-time curvature data where the deposition rate was cyclically varied from 140 Å/s to 2.65 Å/s. At the higher rate, σ_s was tensile, while at the lower rate σ_s was compressive. The magnitude of the stress is clearly

repeatable across cycles. The result that the stress was reversibly dependent on deposition rate across multiple cycles implies that the mechanisms generating both the tensile stress and the compressive stress were acting continuously throughout the deposition process.

From cross-section, focused ion beam (FIB) analyses (Fig. 4.5a-c) it was determined that all films had a similar grain structure and there was no measurable change in grain size with deposition rate within the first two microns of film thickness. Additionally, x-ray diffraction pole figure analysis determined that the films were highly (111) fiber textured, with no change in the texture except for the lowest deposition currents (~1 mA/cm^2), where the texture became mixed (111) / (100). Therefore, since the compressive stress was a function of deposition rate, but the grain structure was not, it is unlikely that changes in grain structure are the source of the compressive steady-state stress observed in our experiments.

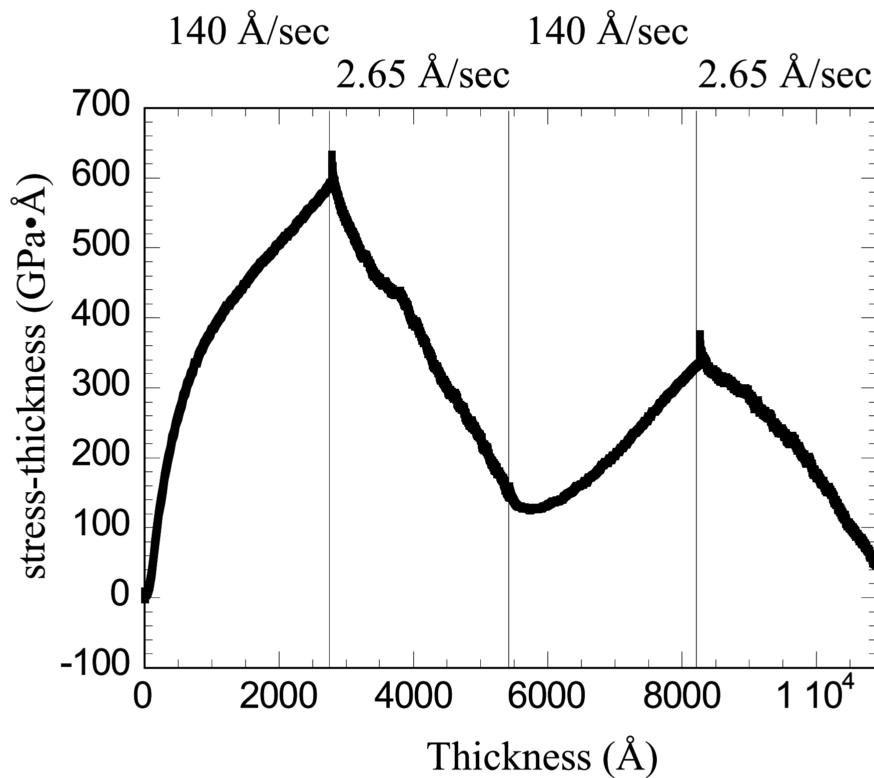

Figure 4.4 - Stress evolution for a sample where the deposition rate was dynamically varied during the deposition.

4.1.3 Compressive stress generation mechanism / discussion

In this section, we discuss mechanisms for stress generation during Ni electrodeposition. Although our focus is on mechanisms for generating compressive stress, a few general comments are in order. Our data clearly demonstrates that the sign and magnitude of the steady-state stress was strongly dependent on deposition rate, as demonstrated in Figs 4.2-4.4. Low rates produce

compression, while at high rates tensile stress dominates. The data of Figure 4.4 strongly suggest that there were two competing stress generation mechanisms, one for tension and one for compression, that acted continuously and simultaneously, but which have different functional dependencies on deposition rate. The most likely mechanism for generating tensile stress at high deposition rates is the formation of nanoscale, high aspect ratio surface roughness. The increase in surface roughness could lead to a process where neighboring grains continually coalesce together during deposition leading to continual "zipping" processes, as has been observed during amorphous film growth [13, 14]. Unfortunately, we lack high resolution, *in-situ* surface characterization such as STM in order to verify this. In what follows, we focus on examining four competing mechanisms for generation of compressive stress. Three of the mechanisms can be eliminated from quantitative comparison to the data.

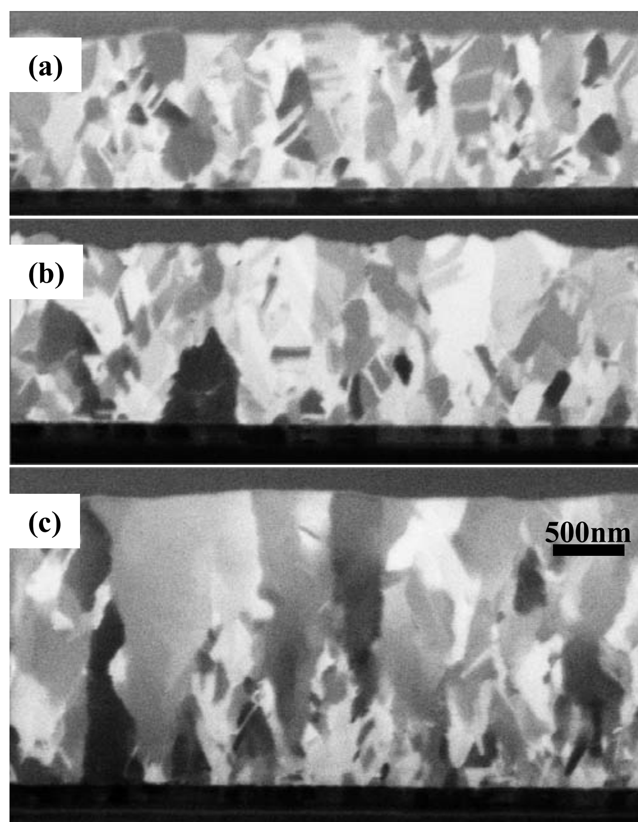

Figure 4.5 - FIB channeling cross-sectional images of Ni samples electrodeposited at different rates: (a) 180 Å/sec, (b) 50 Å/sec, and (c) 1.6 Å/sec.

4.1.3.1 Hydrogen incorporation

Electrodeposition of Ni from an acidic bath is accompanied by the reduction of H_3O at the cathode into atomic hydrogen and H_2O, which results in diffusion of hydrogen into the nickel [15]. The absorbed hydrogen causes the lattice to expand and has been linked to compressive stresses [16-18]. Additionally, based on the observed tensile rise that occurs during interruption of electrodeposition, it has been postulated that a portion of the hydrogen in the Ni diffuses out into the solution during the interrupt [17, 18]. To quantify this, Armyanov *et. al.* derived an

expression for the concentration of the desorbed hydrogen (or other interstitial species) as a function of the measured change in stress (Eq. 2) [18]

$$C_H(t) = \frac{3}{\Delta\Omega / \Omega} \frac{\Delta\sigma_f(t)}{M_f}, \qquad \text{(eq. 4.2)}$$

where, $C_H(t)$ is the concentration of hydrogen that diffused in or out of the Ni film as a function of time, Ω is the atomic volume of the film material, and is $\Delta\Omega$ the change in the atomic volume due to the addition of hydrogen, and $\Delta\sigma_f(t)$ is the change in stress from the end of deposition until a time, t. For hydrogen in Ni, it has been experimentally determined by Peisl that $\Delta\Omega/\Omega$ =0.28 [19].

We performed Elastic recoil detection (ERD) to directly measure the concentration of hydrogen remaining within eight samples where the steady-state stress ranged from -0.46 to +0.26 GPa. ERD is an ion beam technique where a heavy ion (Si^{+4} in these experiments) are used to forward scatter lighter elements out of a sample into a Si detector. Based on the energy and flux of the scattered ions, a concentration profile of the light element in the sample can be determined. For a complete description of the technique, its applications and limitations refer to the review presented by Barbour in ref. 20. The areal resolution for hydrogen in our samples was calculated

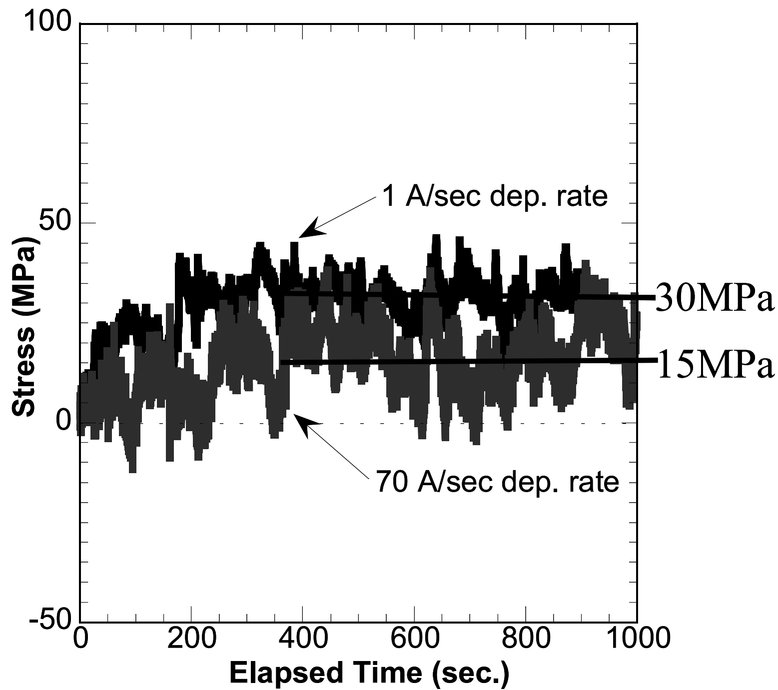

Figure 4.6 - Change in stress as a function of time after deposition was interrupted for two Ni samples deposited at different rates, 1 Å/sec (-570 MPa steady-state stress) – black line, and 70 Å/sec (+156 MPa steady-state stress) – gray line.

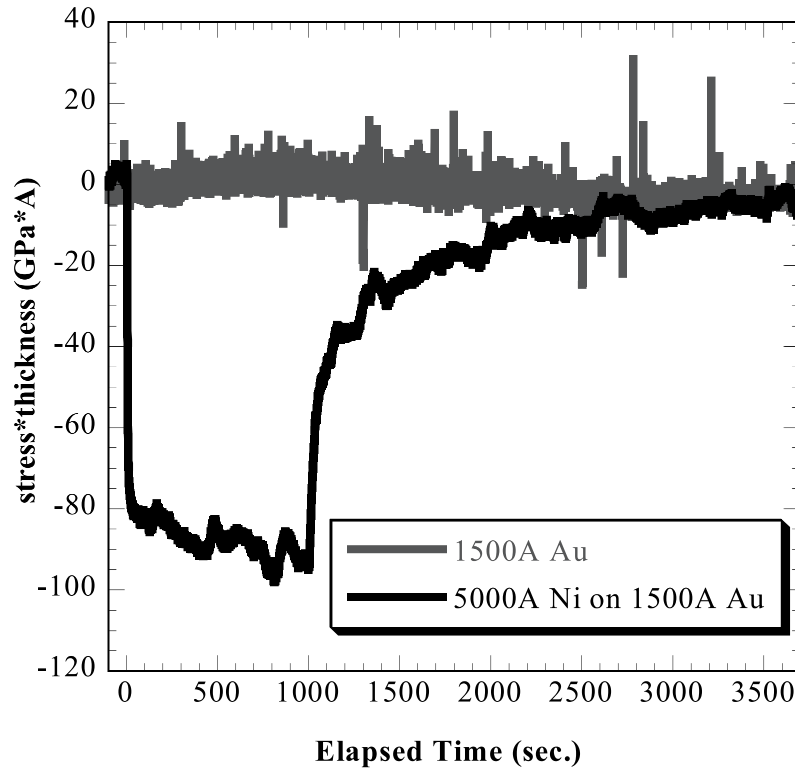

Figure 4.7 - Stress-thickness plot of two samples cycled between open circuit and -1.30 V in a 1.356 M sodium sulfate / 0.5 M Boric Acid solution. The gray line is Au/Ti/Si and black line is 5000 Å Ni on Au/Ti/Si. Note, similar results were observed with the ammonium sulfamate based bath.

using the technique described in ref 21 and determined to be 2.1×10^{15} atoms/cm^2, which for a 4000 Å thick Ni film equates to a concentration resolution of better then 0.1 atomic% hydrogen. ERD discerned no measurable hydrogen in any of the Ni films within two hours of deposition, whereas based on eq. 4.2 (with $\Delta\sigma_f = 0.726$ GPa, and $M_f = 389$ GPa [21]), if hydrogen was the source of the compressive stress there should have been ~1.9 at% contained within in the compressively stressed sample.

The next question we addressed was what quantity of hydrogen diffused out of the samples during the growth interrupt. To determine this, we measured the stress evolution during a series of growth interrupts where σ_s was varied. Figure 4.6 is a plot of the change in stress during a deposition interrupt for two samples, one with a compressive $\sigma_s = -0.57$ GPa (deposition rate = 1 Å/sec) and one with a tensile σ_s, =+0.156 GPa (deposition rate = 70 Å/sec). In the samples, the change in stress during the deposition interrupt was 15-30 MPa. Using eq. 4.2, the quantity of hydrogen that diffused out of the samples during the interrupt was ~0.01 at%, which is consistent with the observations of Armyanov *et. al.* [18]. *Therefore, since only ~0.01 at% hydrogen diffused out of the samples and ~1.9 at% hydrogen is required to induce the observed*

compressive stress but none was seen at a detectable level of 0.1 at%., it must be concluded that hydrogen was not responsible for the majority of the steady-state compressive stress.

To further support this conclusion, several deliberate hydration experiments were performed. First, a sample with tensile σ_s was subjected to hydration in a 1.0M ammonium sulfamate / 0.5 M boric acid bath at -1.30 V for 36000 sec @ 50°C. Two hours after removing the sample from the bath, ERD found no hydrogen in the sample. To confirm that hydrogen in-diffusion can be detected in real-time, during hydration, a 5000 Å thick electroplated Ni film was placed into a bath consisting of 1.356 M sodium sulfate, and 0.5 M Boric Acid. The potential of the Ni cathode was stepped between open circuit potential and -1.30 V and held for 1000 sec. Figure 4.7, a plot of the sample stress during this procedure, clearly demonstrates a fully reversible change in stress. A similar effect was observed with an ammonium sulfamate bath. The data confirms the presence of a fully reversible compressive stress (16 MPa) during the hydration process only when a Ni film was present. When a bare gold substrate was subjected to the same procedure, no compressive stress was observed. These results are consistent with the high hydrogen solubility of Ni compared with Au. From the combination of this result with the ERD data we draw two conclusions: (1) hydrogen incorporation into Ni occurs at levels of order 0.01 at.%, and results in compressive stresses of order 10^1 MPa and (2) the majority of the hydrogen incorporated during electrodeposition of Ni films diffuses back out of the films during the deposition interrupt. Therefore, to reiterate: interstitial hydrogen simply cannot account for the large steady-state compressive stresses (>100 MPa) observed during electrodeposition at low currents/rates.

It should be noted that ERD analysis found hydrogen in the Ti adhesion layer with concentrations that ranged from 0-10 atomic%. However, there was no correlation between σ_s in the Ni film and the quantity of hydrogen found in the Ti adhesion layer.

4.1.3.2 Impurity incorporation

Similar to the effect previously discussed with hydrogen, other impurities can induce a compressive stress when incorporated into Ni [22]. The most prevalent impurities in electrodeposited Ni are carbon, sulfur, and oxygen [2], the concentrations of which vary with the Ni deposition rate. This variation is the result of the competition between the Ni deposition current, which is kinetically limited, and the impurity deposition current, which is diffusion limited. Thus, the deposition rate of bath impurities is independent of over-potential, whereas the deposition rate of Ni depends exponentially on over-potential. This results in the impurity concentration decreasing as the Ni deposition rate increases, which would cause the magnitude of the impurity-related compressive stress to decrease with increasing deposition rate, as we observe in Figs. 4.2 and 4.3. Secondary ion mass spectroscopy (SIMS) analysis of a set of samples of varied deposition rate confirmed that the level of C, S, and O decreased as the deposition rate was increased, see Fig 4.8 [23]. Furthermore, the concentration of impurities, of order 50 ppm each for C, S, and O, was consistent with previous reports for electrodeposited Ni [24]. Using eq. 4.2 an effective value $\Delta\Omega/\Omega$ for the sum of the three concentrations of the impurities was calculated to be ~48, where it was assumed that C, O, and S all have similar $\Delta\Omega/\Omega$'s, (111) bi-axial modulus of the Ni was 389 GPa [20], and from our data, the measured change in σ_s was –625 MPa. The value of $\Delta\Omega/\Omega$ was significantly larger then the value 1.5 calculated for the results of Alexander and Hoffmann for oxygen incorporation into Ni [22].

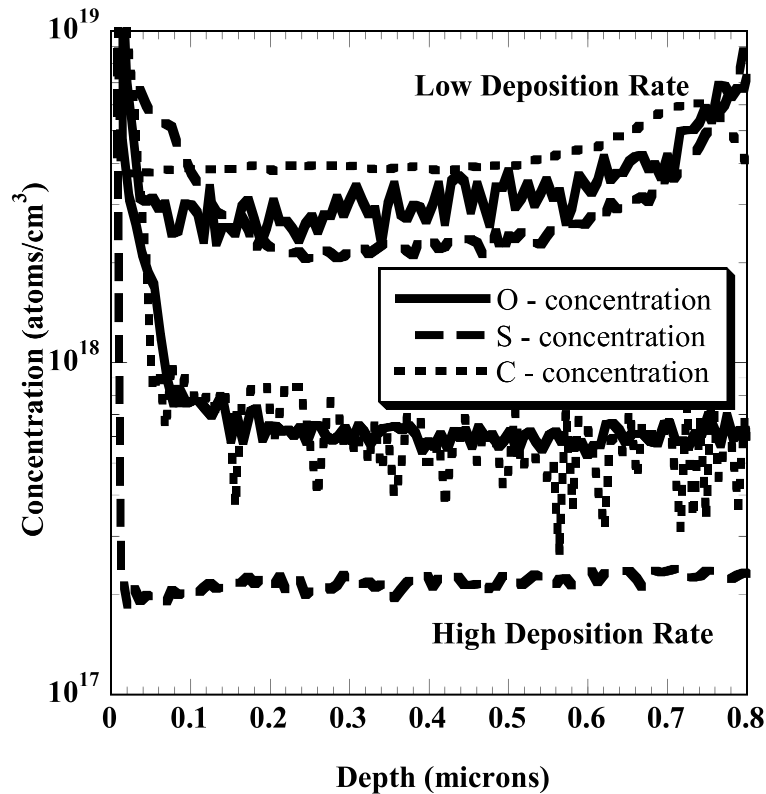

Figure 4.8 - Concentration profiles of C, S, and O in electrodeposited Ni at 110 Å/sec (35 mA/cm^2, lower data set) and 3.6 Å/sec (2.5 mA/cm^2 – upper data set) deposition rate samples.

Therefore, though impurities can induce a compressive stress, it is likely that it was at least an order of magnitude smaller then the observed change in the steady-state stress.

4.1.3.3 Capillarity stress

X-ray diffraction studies have shown that during the early stages of thin film growth, small islands exhibit reduced lattice parameters relative to bulk due to the effect of surface stress [25,26]. It has also been shown how this process might induce the compressive stresses often observed during thin film deposition after island coalescence has occurred [27-30]. Cammarata derived a simple analytical expression for this process that predicts that the asymptotic limit for the measured film stress at infinite thickness is inversely proportional to the island's width (d) when the island first becomes constrained against lateral expansion or contraction, which we take here simply to be the observed mean grain size (since grain growth is not expected under these conditions) [31]. The asymptotic stress can be written simply as $\sigma = F/d_{obs}$, where F is the surface stress (of order 1 J/m^2) and d_{obs} is the observed grain size in the first micron of film thickness.

Although this mechanism is almost certainly operating in our films, we argue that it is not the predominant source of compressive stress. First, the large magnitude of compression that we observe at low deposition rates (up to -600 MPa) requires a much smaller grain size (of order 2

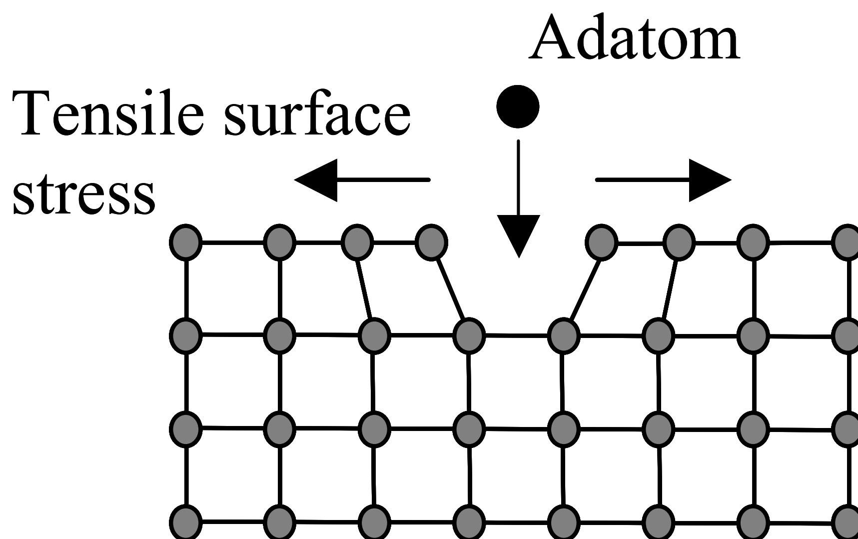

Figure 4.9 - Schematic of atom becoming trapped at the coalescence point of two opposite polarity atomic steps.

nm) than is observed here. Also, the Cammarata model predicts that the stress should increase in magnitude to its final asymptotic value over a range of film thickness $\Delta h \approx 10d_{obs} \approx 1$ μm in our experiments. However, our compressive stress reaches steady-state for $h \approx d_{obs}$. Finally, we observe a range of compressive stress magnitudes as a function of deposition rate, while the microstructure is almost rate invariant, which is inconsistent with the basic premise of the capillarity model.

4.1.3.4 Chemical potential gradient driven atom incorporation

As was previously discussed, the presence of interstitial impurities results in the creation of compressive stress due to the localized expansion of the lattice. A similar process occurs when Ni atoms are trapped interstitially, or at low coordination sites such as a grain boundary or interstitially in a Ni film. The literature has established two possible mechanisms by which the incorporation of atoms into low coordination sites creating compressive stress is possible: kinetic trapping [32] and adatom trapping at grain-boundaries [33]. Though there is currently no definitive evidence that these mechanisms are active during thin film growth, there is evidence that indicates that they are highly plausible [33, 34]. Therefore, we believe that it is beneficial to evaluate them as possible sources for the steady-state stress observed during electrodeposition of Ni from a sulfamate-based bath.

The kinetic trapping model proposes that during deposition atoms occasionally become trapped as excess surface interstitials at the coalescence point of two opposite-signed atomic steps (Fig. 4.9). When the next layer of material overgrows the trapped atom, it then essentially becomes a

bulk interstitial that can induce a compressive stress [32]. This process is enhanced when a tensile surface stress, which common in metals, causes surface steps to become splayed away from each other. Based on this simple model, the steady-state trapping only needs to occur approximately once per 1000 surface lattice sites to reach the 100 MPa compressive stresses observed in typical metal films.

Trapping of atoms at grain-boundaries was proposed by Chason *et. al* [33]. The initial work examined the case where diffusion of the adatoms was allowed within the grain boundary, which was predicted to cause a compressive growth stress that was reversed during an interruption of the deposition [33]. More recently, this work was expanded by Sheldon, *et. al.* to include the case of zero mobility of the atoms in grain-boundaries [34], which due to the low homologous temperature of Ni during electrodeposition, is the most relevant scenario. In the Sheldon model, excess atoms are captured only at the points where the grain boundary intersects the free surface, and do not diffuse further. The capture of the atoms in the grain boundary is still energetically favorable, but the important role of diffusion kinetics is acknowledged explicitly.

In both the kinetic trapping and the grain-boundary trapping model a difference in the chemical potential between the free-surface and the trapping site, i.e. coalescing steps edges or grain boundary, can result in a driving force for diffusion of adatoms into the trapping site [34]. Chason *et al.* [33] proposed that such a driving force results from the presence of adatoms on the free-surface during deposition and that the super-saturation induced by the presence of these adatoms is only weakly dependent on deposition. As a result, increasing the deposition rate causes the grain boundary area to increase faster than the adatom supply, so that higher rates lead to lower compressive stress. A similar effect can be envisioned for the kinetic trapping model where increases in deposition rate yield less compressive stress. This behavior is qualitatively consistent with our observation of a decrease in the compressive stress with increasing deposition rate. However, the atomistics of electrodeposition are significantly more complex then the models presented above, where vacuum deposition was assumed. Further investigation is required to elucidate the exact nature of these differences though some conclusions can be drawn from the work of Dona and Gonzalez-Velasco [35]. Dona and Gonzalez-Velasco observed that during electrodeposition of Ag, decreasing the overpotential results in an increase in the surface diffusivity of up to 2 orders of magnitude. Electrodeposition of Ni should behave similarly. Since atom diffusion into trapping sites is a thermodynamically-driven process, a decrease in the surface diffusivity results in a corresponding decrease in the number of adatoms reaching the grain-boundary. The result is that decreasing the overpotential induces more compressive stress created due to more atoms reaching the trapping sites, which is also consistent with our observations.

4.1.4 Conclusions

We have examined three likely sources for the compressive stress observed during electrodeposition of Ni from a sulfamate-based electroplating bath and determined that atom diffusion into trapping sites is the only mechanism that could not be discounted outright. The other two likely mechanisms: hydrogen / impurity incorporation, and capillarity stress, were determined not to be dominant mechanisms, although they could contribute some minor component of the compressive stress. However, further study is still required to conclusively determine if atom diffusion into trapping sites is inducing the observed compressive stress.

4.1.5 References for Section 4.1

[1] E. J. Mills, J. Proc. Roy. Soc. **26**, 504 (1877).

[2] J. W. Dini, *Electrodeposition, the Materials Science of Coating and Substrates* (Noyes publications, Norwich, 1993), p.126.

[3] J. A. Floro, E. Chason, and S. R. Lee, Materials Research Society Symposium Proceedings **405**, 381 (1996).

[4] G. G. Stoney, Proc. R. Soc. London, Ser. **A82**, 172 (1909).

[5] J. A. Floro and E. Chason, *In Situ Real-Time Characterization of Thin Films*, Orlando Auciello and Alan R. Krauss, eds.(Wiley, NY, 2001), pp. 191-216.

[6] F A Möller, J Kintrup, A Lachenwitzer, and O M Magnussen, Physical Review B. **56**, 12506 (1997).

[7] J W Dini and H R Johnson, Thin Solid Films **54**, 183 (1978).

[8] C S Lin, P C Hsu, L Chang, and C H Chen, J. Appl. Electrochemistry **31**, 925 (2001).

[9] S W Banovic, K Barmak, and A R Marder, J. Materials Science **33**, 639 (1998).

[10] C S Lin, K C Peng, P C Hsu, L Chang, and C H Chen, Materials Transactions, JIM **41**, 777 (2000).

[11] N V Mandich and D W Baudrand, Plating and Surface Finishing **89**, 68 (2002).

[12] S Basrour and L Robert, Materials Sci. and Engineering **A288**, 270 (2000).

[13] J. A. Floro, P. G. Kotula, S. C. Seel, and D. J. Srolovitz, Phys. Rev. Lett. **91**, 096101/1-4 (2003).

[14] S. G. Mayr and K. Samwer, Phys. Rev. Lett. **87**, 036105/1-4 (2001).

[15] R. K. Dorsch, Electroanalytical Chemistry and Interfacial Electrochemistry **21**, 495 (1969).

[16] E. A. Vuilleumier, Trans. Electrochem. Soc. **42**, 99 (1922).

[17] V. Kohlschutter and E. A. Vuilleumier, Electrochem. Soc. **24**, 300 (1918).

[18] S. Armyanov and G. Sotirova, Surface and Coating Technology **34**, 411 (1988).

[19] H. Peisl, in *Hydrogen in Metals 1, Basic Properties*, edited by G. Alefeld, Berlin, 1978

[20] J. C. Barbour, in *Handbook of Modern ion beam materials analysis*, **1**st edition, edited by J. R. Tesmer, M. Nastasi, J. C. Barbour, C. J. Maggiore, J. W. Mayer (Materials Research Society, Pittsburgh, 1996), Vol. **1**, Chap. 5

[21] John P. Hurth and Jens Loath, *Theory of Dislocations*, **2**nd edition (Krieger, Malabar, 1992), Vol. **1**, appendix.

[22] P. M. Alexander and R. W. Hofflman, J.Vac. Sci. Technol. **13**, 96 (1976).

[23] SIMS performed by Charles Evans & Associates

[24] J. W. Dini and H. R. Johnson, Thin Solid Films **54**, 183 (1978).

[25] A Krost, A Dadgar, J Bläsing, A Diez, T. Hempel, S Petzold, J Christen, and R Clos, Applied Phys. Lett. **Oct**, xxx (2004).

[26] A Debelle, G Abadias, A Michel, and C Jauen, Applied Phys Lett. **84**, 5034 (2004).

[27] R. C. Cammarata, Prog. Surf. Sci. **46**, 1 (1994).

[28] R. C. Cammarata, T. M. Trimble, and D. J. Srolovitz, J. Material Research **15**, 246B (2000).

[29] R. J. Koch, Phys.: Condensed Matter **6**, 9519 (1972).

[30] R. Abermann, R. Kramer, and J. Maser, Thin Solid Films **52**, 215 (1978).

[31] F. Spaepen, *Acta Mater.* **48**, 31 (2000).

[32] E. Chason, B. W. Sheldon, L. B. Freund, J. A. Floro, and S. J. Hearne, Physical Review Letters **88**, 156103-1 (2002).

[33] B. W. Sheldon, A. Ditkowski, R. Beresford, E. Chason, and J. Rankin, J. Appl. Phys. **94**, 948 (2003).

[34] Sheldon, B. - Private communication.

[35] J. M. Dona and J. Gonzalez-Velasco, Surface Sci. **274**, 205 (1992).

4.2 Stress during NiMn electrodeposition

4.2.1 Introduction

Stress creation during thin film deposition has been a concern for over a century due to the limits it places on applications [1,2]. This is particularly true for electrodeposited films such as Ni and its alloys, for which stresses range from 10^2 MPa compression to tension depending on the bath chemistry and growth conditions [3,4]. Recent efforts to increase the high-temperature (~600°C) strength of Ni have utilized co-deposition of 1 to 2 at% Mn during plating, but the resultant alloy possesses a significantly higher tensile stress [5-7]. To overcome this, pulse plating procedures were developed that reduce the mean film stress [6]. However, in these studies, there were no investigations into the actual stress evolution during deposition or the possible sources of these stresses. In this article, we have correlated the stress evolution during electrodeposition of NiMn with *ex-situ* microstructural measurements to examine the source of stress active during electrodeposition.

4.2.2 Experimental set-up

Stress evolution during electrodeposition was obtained from real-time wafer curvature measurements that were described in section 4.1.2. All Ni and NiMn films were nominally 1 μm thick and electrodeposited onto substrates cleaved from a thermally oxidized Si(100) wafer capped with electron-beam deposited Ti/Au films, 150 Å and 1500 Å thick, respectively. Immediately prior to electrodeposition, the substrates were cleaned with a 10 minute exposure to UV/ozone in a Novascan PSD-UVT system. The actual film and substrate thicknesses were determined from SEM imaging of cleaved cross-sections. All Ni and NiMn films were electrodeposited using the same 2 L surfactant-free sulfamate bath composed of 1.35 M/L Ni sulfamate, 0 - 5.0 g/L Mn from $MnCl_2{\cdot}4H_2O$, 30 g/L boric acid, and 18.2 MΩ DI water. The samples were electroplated consecutively with the current density (deposition rate) varied from run-to-run over a range of 1 to 20 mA/cm^2. The Mn content was then increased stepwise from 0 g/L to 5.0 g/L by adding 2.5 g/L Mn to the bath and the range of current densities was re-run at each new Mn content. The depletion of Mn and Ni in the bath was less then 1% over the set of samples. The plating system used a standard three-probe technique with a saturated Hg/Hg-sulfate reference electrode (0.64 V versus a standard hydrogen electrode) and soluble Ni s-rounds (Inco, Canada) in a titanium basket as the anode.

Mn concentrations in the films were determined using quantitative wavelength dispersive spectroscopy (WDS) analyses on a JEOL 8600 Electron Microprobe X-ray Analyzer and compared against a pure Ni standard. Phi-rho-Z matrix corrections were used to transform the raw data (K-values) into quantitative, weight percent values. Fig. 4.10 is a plot of the Mn concentration as a function of plating current from a 2.5 g/L Mn and a 5.0 g/L Mn bath. These results are consistent with previous observations of the plating behavior of this bath, where the Mn concentration scales with current density [7].

X-ray diffraction (XRD) pole figures were collected on a Scintag X1 diffractometer using a sealed-tube copper K-α radiation source and a Peltier-cooled solid-state detector. The X-ray generator settings were 40mA and 45kV. The incident-beam was collimated using a 1mm

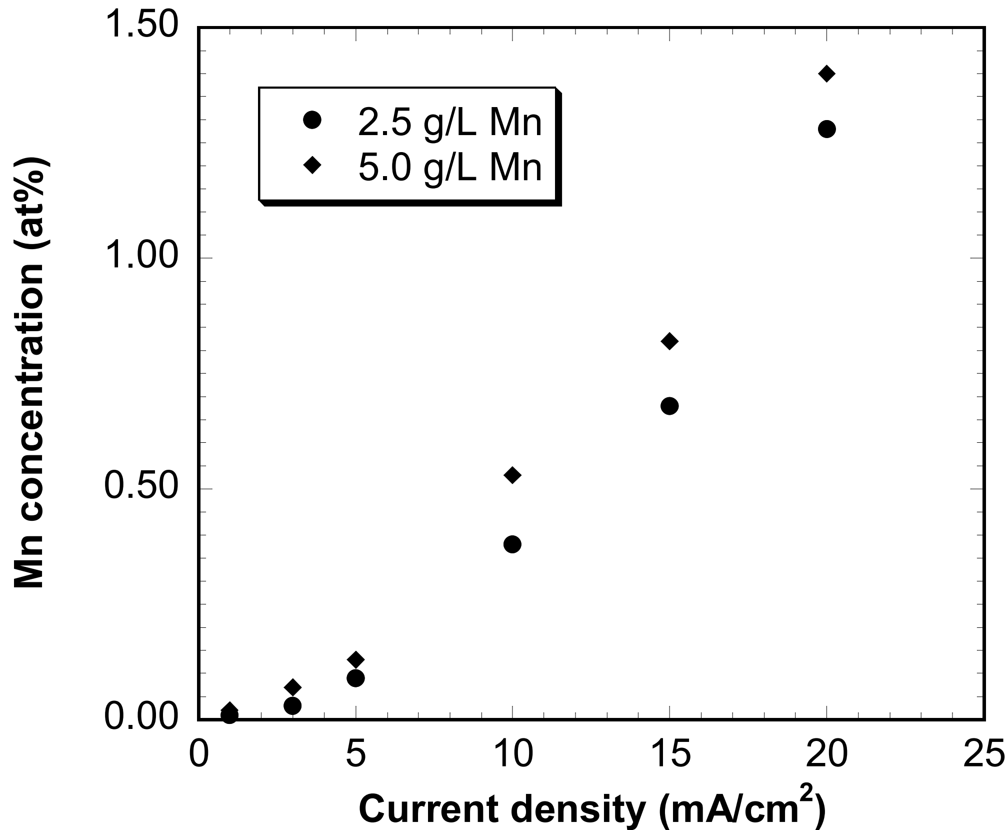

Figure 4.10 - Measured Mn concentration versus deposition rate for the 2.5 g/L Mn and 5.0 g/L Mn baths.

diameter pinhole aperture. Pole figures were measured using 5 degree steps in X and Φ angles, each position being counted for 0.5 seconds. Micro-strain measurements were derived via Williamson-Hall analysis of full width at half max values for the Ni (111), (200), and (311) reflections, where the specimens were assumed not to have significant crystallite size broadening. Peak broadening is negligible for crystallite sizes greater that 0.1 micron and the estimated Ni grain size was 150 nm as measured by AFM surface topology.

4.2.3 Results / Discussion

4.2.3.1 Transition stress

The stress evolution in NiMn was similar to that previously reported for Ni electrodeposited from a sulfamate bath at elevated temperatures[4]. In both cases, the films' stress displayed two regions of behavior: a transition stress (σ_t) region followed by a steady-state stress (σ_s) region (Fig. 4.11). The σ_t region, from 0 to about 1000 Å film thickness, consisted of a large tensile

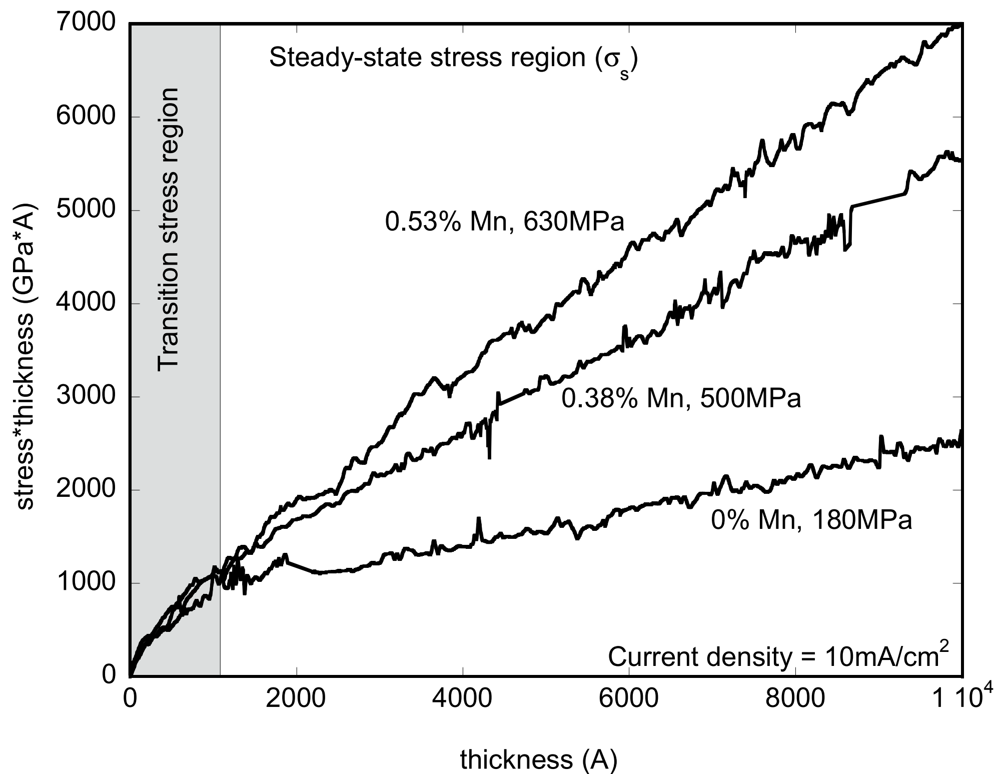

Figure 4.11 - Stress-thickness versus thickness plot for three samples all grown at 10mA/cm^2, where the Mn concentration was varied in the bath from 0 g/L to 2.5 g/l to 5.0 g/L.

stress that ranged from 0.6 to 1.0 GPa. Previous *in-situ* STM studies found that the first few monolayers of Ni deposited on the (111) surface of Au were semi-coherent, which resulted in a tensile strain due to the 16% lattice mismatch between Ni and Au [8]. To determine if σ_t could be related to coherency stress in this case, we performed dark-field cross-section transmission electron microscope imaging of Ni electrodeposited on Au. In the 1 μm thick films a significant fraction of the Ni grains grew epitaxially oriented with the underlying Au (111) grains, which is consistent with the Ni being semi-coherent with the Au substrate. The maximum observed stress is about 1.5 GPa in the early stages of NiMn growth. Using a biaxial modulus of 389 GPa for Ni (111) [9], this corresponds to a strain of 0.004. We note that while the lattice mismatch is 16%, the expected magnitude of the misfit strain is better characterized by the strain associated with the "near coincidence site lattice", which is of order 0.006 for 46/36 alignment [10]. The lower measured value could either be due to relaxation, or to the fact that not all NiMn grains were epitaxial to begin with.

In addition to the coherency stress, σ_t was observed to increase slightly with current density for both the Ni and the NiMn films, indicating that another stress generation mechanism was active during this region. However, the variations were at the detection limit of our apparatus, so no definitive conclusion could be drawn.

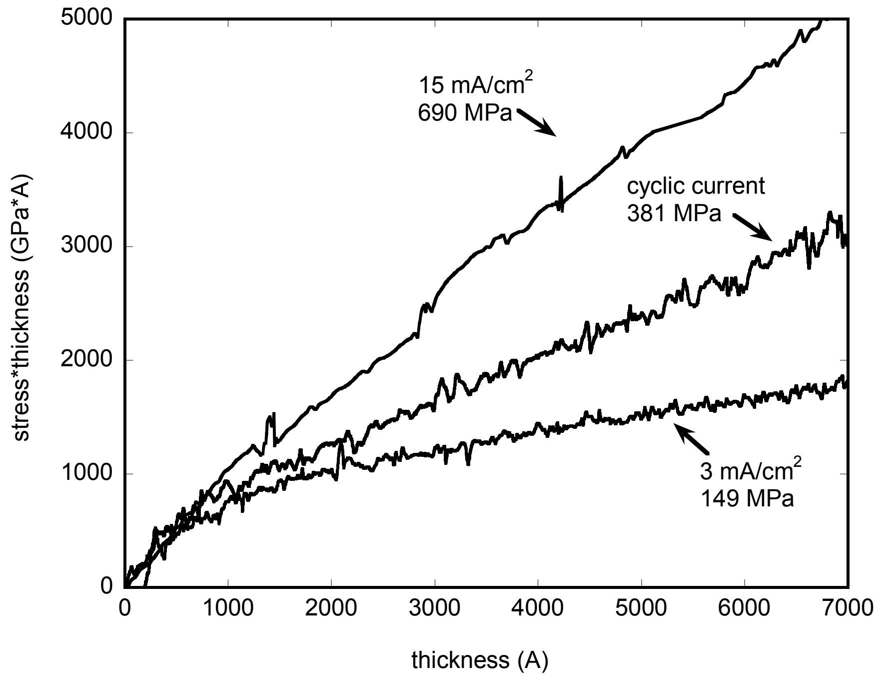

Figure 4.12 - Stress-thickness versus thickness plot for three samples grown using the 5.0 g/L Mn bath. The upper and lower curves were deposed at constant rates of 15 mA/cm^2 and 3 mA/cm^2 respectively and the current density in the middle curve was cycled between 15 mA/cm^2 and 3 mA/cm^2, for 0.67 sec. and 4.4 sec. respectively.

It should also be noted that density functional theory (DFT) modeling predicts an increase in the lattice parameter of 0.04% per at% Mn for substitutional incorporation of low concentrations of Mn into Ni. Hence, for NiMn(0.53%), the coherency stress on Au should be about 35 MPa less tensile than pure Ni, [11]. However, this effect is within the noise of our measurements and was not clearly detected.

4.2.3.2 Steady-state stress

As was previously observed for pure Ni, the magnitude of σ_s was strongly dependent on current density, with higher densities (or deposition rates) resulting in increased tensile stress [4]. *The addition of Mn resulted in an additional increase in σ_s for a given current density*, as shown in Fig. 4.11. Fig. 4.11 shows that σ_s is always less than σ_t. An obvious explanation for this stress reduction is via bulk relaxation of σ_t, e.g., by misfit dislocation formation. However, we can

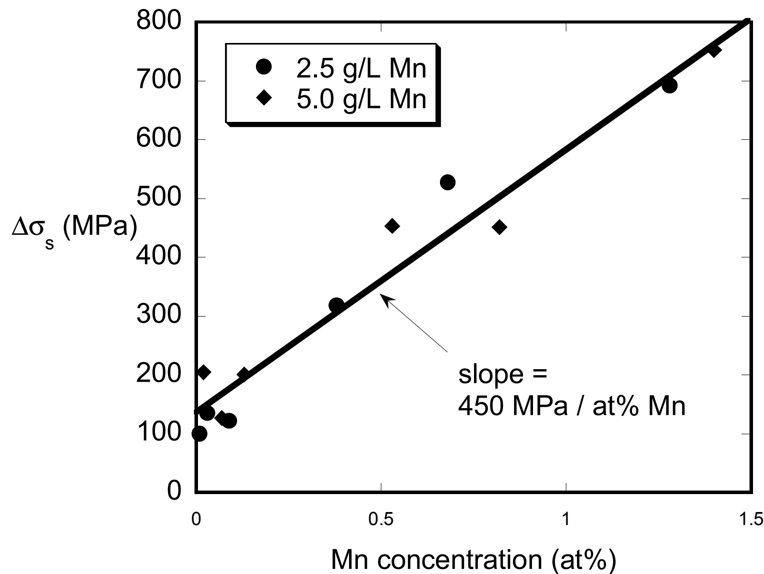

Figure 4.13 - Difference between the σ_S-stress as function of Mn concentration at constant current density for the three baths, 0 g/L Mn, 2.5 g/L Mn, and 5.0 g/L Mn.

demonstrate that this is not the predominant mechanism that determines the magnitude of σ_s., We performed dynamic variations in the current density (i.e., changing the current density within a single growth run) and measured the corresponding film stress. We found that the stress magnitude dynamically responded to the changes in current density. In Fig. 4.12 the middle curve is the stress evolution measured for a sample where the current density was cycled between 15 mA/cm^2 and 3 mA/cm^2, for 0.67 sec. and 4.4 sec. respectively. Note that the film thickness changes associated with these parameters are only 28 Å and 36 Å, respectively, which is sufficiently small that the individual oscillations are not discernible in Fig. 4.12. However, the mean stress in this sample was 381 MPa, which is reasonably close to the average stress of 417 MPa predicted from the thickness- weighted average of the high (upper curve) and low (lower curve) current density samples. This demonstrates that the magnitude of σ_s was established by processes associated with film growth, and not bulk relaxation.

Fig. 4.13 is a plot of the *difference* in σ_s between pure Ni and NiMn samples deposited at the same current density plotted against the measured Mn content in the samples, e.g. $\Delta\sigma_s = 320$ MPa for the 0.38 at% Mn sample in Fig. 4.11. The slope of this plot is the change in σ_s per at% Mn added and equals 450 MPa per at% Mn. Interestingly, the extrapolated change in stress for 0 % Mn intersects the stress axis at 135 MPa rather than zero. This was likely the result of the addition of Cl^-, a known stress inducing agent in Ni electrodeposition [3], which was added

along with Mn in the form of $MnCl_2 \cdot 4H_2O$. However, it is unlikely that Cl^- was responsible for the positive slope of $\Delta\sigma_s$, because the incorporation of cathodic impurities typically decreases with increased current density, which would result in a decrease in σ_s with increased current density [3]. To verify this, we are currently conducting further experiments with Cl^--free sources of Mn.

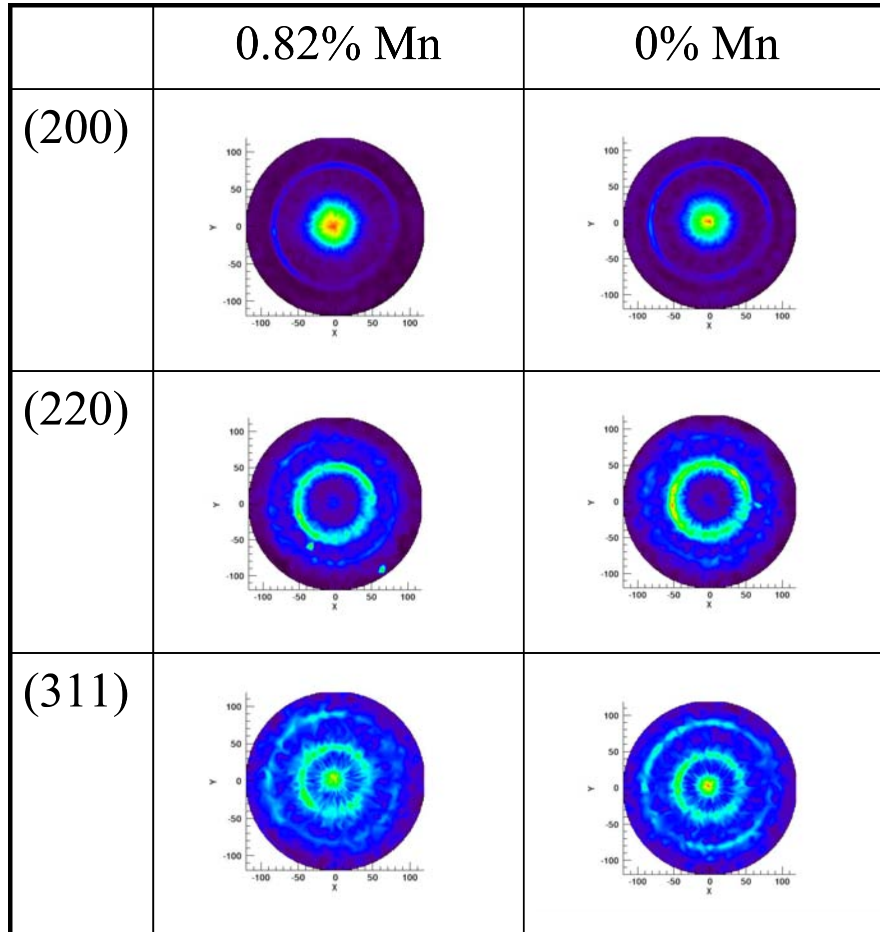

Figure 4.14 - XRD pole figures showing similar texture for two samples (0 and 0.82 at % Mn) both deposited at $15 mA/cm^2$.

Large stress changes, such as those seen in Fig. 4.13, are typically the result of dramatic changes in the microstructure. However, texture measurement from XRD pole figures, Fig. 4.14, and grain size measured with atomic force microscopy, did not show significant variation with the changes in Mn concentration. The only microstructural parameter that we found to track with the change in Mn content was the micro-strain measured from X-ray peak broadening analysis, Fig. 4.15. This micro-strain likely has contributions from both the substitutional Mn atoms, and

possibly from twins. Previous studies of the microstructure of NiMn have observed an increased density of twins that correspond to an increased Mn content [14], and high densities of twins are know to contribute to microstrain However, it is important to realize that for either a constant Mn content or a constant twin density (as a function of film thickness), no macro-strain is expected. Therefore, the observed variation in σ_s as a function of current density and Mn content must have resulted from another source.

A clearly-established source of tensile stress in continuous films is the process of "grain boundary coalescence", in which neighboring grains pull towards one another at the growth surface inducing a tensile stress [15]. This process is a continuation of the well-documented island coalescence process, where tensile stress is induced by discrete islands laterally deforming upon contact to minimize surface energy [16,17]. Steady state is reached when the reduction in surface energy is balanced by the change in the volume average energy due to stress. In a previous study, we demonstrated that during electrodeposition of litho-graphically defined Ni islands the majority of the coalescence stress was the result of grain boundary coalescence rather than island coalescence [18]. This process has been observed in a number of materials systems [16,19,20] and has been modeled by Sheldon, *et. al.* [16]. Sheldon predicts that the maximum coalescence stress (σ_{max}) is reached when a film with no active relaxation mechanisms is planar, i.e. there are no grain-boundary groves. The expression derived by Sheldon is as follows:

$$\sigma_{\max} = \left[\frac{2M_f \Delta\gamma}{L} \right]^{1/2}, \qquad \text{(eq. 4.3)}$$

where L is the in-plane grain size, and $\Delta\gamma$ is the difference in surface energy between a free surface and half the grain-boundary interfacial energy. Assuming a (111) textured Ni film, $\Delta\gamma$ = 1.85 J/m^2, M_f = 389 GPa [17], and L = 150 nm, then σ_{max} = 3.09 GPa, which is significantly larger then the σ_s in Ni and NiMn. Sheldon predicts that variation in the contact surface angle between grains will cause a decrease in the stress from σ_{max}. However, our AFM scans of the

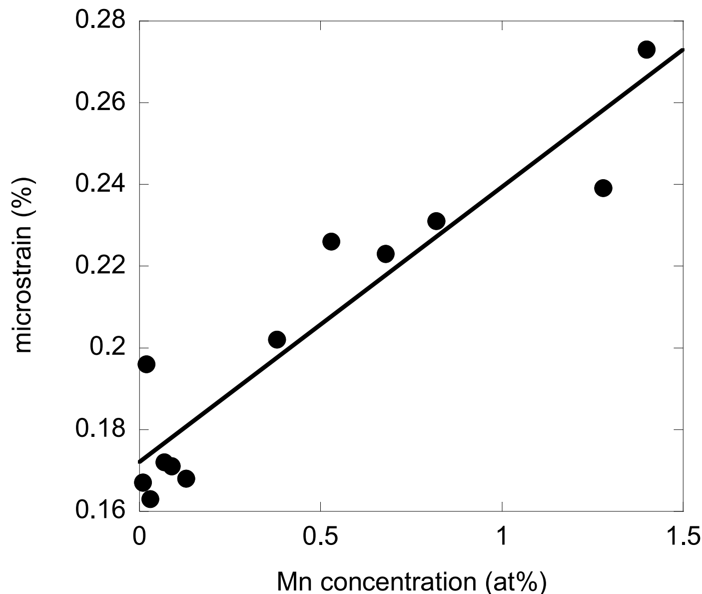

Figure 4.15 - XRD measured % micro-strain as a function of Mn concentration.

surface found that the maximum surface angle and overall surface roughness at the grain-boundaries did not vary with Mn content, where as there was a strong change in σ_s with Mn content. Therefore, we speculate that the effect of Mn/current density was not on the overall surface roughness, but rather on the partial relaxation of tensile stresses due to local surface diffusion, such as that observed in vacuum deposited materials [21].

It is not unreasonable to expect that there would be significant surface mobility of the Ni atoms during electrodeposition, despite the low homologous temperature of Ni at room temperature. Previous works have found that the surface mobility of Ag increased by up to two orders of magnitude during electrodeposition [22]. Therefore, if a similar process were active during electrodeposition of Ni the stress would be reduced from σ_{max}. Additionally, we propose that the Mn acts to reduce the surface diffusion of Ni, which results in less relaxation of the σ_s with increased Mn concentration. However, further study is required to determine the validity of this hypothesis.

4.2.4 Conclusions

We have measured the stress evolution during electrodeposition of NiMn thin films and found that there are two regions of stress evolution behavior that are similar to those previously observed for Ni electrodeposition. The stress in the initial transition region is consistent with semicoherent epitaxial growth of Ni (111) grains on the underlying Au (111) grains. The stress in the final steady-state region was found to strongly depend on current density and Mn content, and could be changed dynamically during film deposition by changing the current density. The origins of the steady-state stress are more difficult to identify, but we propose that this tensile stress is the result of grain boundary coalescence.

4.2.5 References for Section 4.2

[1] E. J. Mills, J. Proc. Roy. Soc. **26**, 504 (1877).

[2] G. G. Stoney, Proc. R. Soc. London, Ser. **A82**, 172 (1909).

[3] J. W. Dini, *Electrodeposition, the Materials Science of Coating and Substrates* (Noyes publications, Norwich, 1993), p.126.

[4] Sean J. Hearne and Jerry A. Floro, J. Appl. Physics **97**, 014901-1 (2005).

[5] S. H. Goods, J. J. Kelly, and N. Y. C. Yang, Microsystem Technologies **10**, 498 (2004).

[6] J. J. Kelly, S. H. Goods, and N. Y. C. Yang, Electrochemical and Solid-State Lett. **6**, C88 (2003).

[7] S. Graham, J. Kelly, N. Yang, and T. Borca-Tasciuc, Microsystem Technologies **10**, 510 (2004).

[8] G. G. Stoney, Proc. R. Soc. London, Ser. **A82**, 172 (1909).

[9] J. A. Floro and E. Chason, *In Situ Real-Time Characterization of Thin Films*, Orlando Auciello and Alan R. Krauss, eds.(Wiley, NY, 2001), pp. 191-216.

[10] F A Möller, J Kintrup, A Lachenwitzer, and O M Magnussen, Physical Review B. **56**, 12506 (1997).

[11] John P. Hurth and Jens Loath, *Theory of Dislocations*, **2**nd edition (Krieger, Malabar, 1992), Vol. **1**, Chap. Appendix.

[12] Y. Gao, P. G. Shewmon, and S. A. Dregia, Acta Metall. **37**, 3165 (1989).

[13] Steven Foiles, to be published.

[14] N. Y. C. Yang, T.Y. Headley, J.J. Kelly, and J.M. Hruby, Scripta Materialia **51**, 761 (2004).

[15] B.W. Sheldon, K.H.A. Lua, and A. Rajamani, J. Appl. Physics **90**, 5097 (2001).

[16] W. D. Nix and B. M. Clemens, J. Mater. Res. **14**, 3467 (1999).

[17] R. W. Hoffman, Thin Solid Films **34**, 185 (1976).

[18] S.J. Hearne, S.C. Seel, J.A. Floro, C.W. Dyck, W. Fan, and S.R.J. Brueck, J. Appl. Physics **97**, 083530 1 (2005).

[19] A Rajamani, R Beresford, and B.W. Sheldon, Applied Physics Letters **79**, 3776 (2001).

[20] S.C. Seel, C.V. Thompson, S.J. Hearne, and J.A. Floro, J. Appl. Physics **88**, 7079 (2000).

[21] M.D Thouless, Acta Metall **41**, 1057 (1993).

[22] J.M. Dona and J. Gonzalez-Velasco, Surf. Science **274**, 205 (1992).

5. ATOMISTIC SIMULATIONS

5.1 Mechanical response of thin film nanoscale materials

Atomistic molecular dynamics simulations were used to understand the mechanical response under deformation of the thin film nanoscale materials studied experimentally. The simulations use interatomic potentials for Al of the embedded atom form. Two types of results will be presented. First, the defects generated during the deformation process will be visualized. This will gain insight into the mechanisms that operate in the thin flm. This work differs from previous work in two ways. First, the samples are thin films, as opposed to bulk samples, and the role of film thickness will be examined. Second, the methods of defect identification used here have not been applied in the other studies. The second type of results are predictions of the macroscopic stress-strain response of the film as well as the stored energy of the film.

The identification of atomic level defects is a challenging aspect of the atomistic computer simulations of deformation. Many of the traditional methods of defect identification do not differentiate between elastic strain and structural defects. For example, a commonly used approach looks at the potential energy associated with each atom. This will be elevated both for the vicinity of defects as well as for regions of large strain. In this work, two types of defect identification will be employed. The first is the centrosymmetry parameter first introduced by Kelchner, et al. [1]. This method utilizes the fact that each atom in an fcc lattice is a local point of inversion symmetry. Therefore, if an atom has a neighbor at r, it also has a neighbor at $-r$. In this approach, the deviation from this condition for the neighbors of a given atom is determined. A small value indicates atoms in a locally defect free environment while a large value indicates a local structural defect. The second approach that will be utilized is the slip-vector introduced by Zimmerman et al. [2]. This approach relies on a reference lattice. The reference lattice is typically the starting atomic configuration. The slip vector is defined such that it corresponds to the local slip that has occurred in the current configuration compared to the reference lattice. The slip vector is a natural way to identify dislocation activity since this activity corresponds to local slip.

The first step of the simulations is to obtain an initial structure. Polycrystal films with a (111) texture and columnar grains are produced. This is accomplished as follows. Periodic boundary conditions will be applied in the plane of the film. Within the periodic cell, a set of points is distributed randomly. These points will be the centers of the grains. Each grain will have a [111] direction normal to the film and the other directions are rotated by a randomly chosen amount about this axis. Within the Voronoi cell associated with each point, atoms are placed in accord with the fcc structure with this rotation. The resulting structure is annealed using Monte Carlo simulations to produce a dense film. The result of such a growth process is shown in Figure 5.1, which is displayed using the centrosymmetry parameter. The shaded regions represent grain boundaries and/or dislocations. Note that in various places that there are series of dots. These correspond to the dislocations in low angle grain boundaries.

The mechanical response is computed in a quasi-static manner. The atomic positions in the initial configuration are optimized to minimize the energy. A small strain is applied to the cell and the positions are optimized again. The strain applied in each step is 0.5% along one

direction of the sample. This process is repeated until the desired level of strain is attained. In this case, total strain of 10% was reached. The atomic configurations and macroscopic stresses can then be determined at the intermediate levels of strain.

Snapshots of the center slice of the nanograined film are shown in Figure 5.1 at increments of 2% strain. Examination of these figures and similar ones based on the slip vector indicate that there are two types of deformation occurring. First, as the strain proceeds, several of the grain boundaries move in response to the strain. This can be seen, for example, in the upper right corner of the large central grain. There is also clear evidence of dislocation motion during the deformation. Note that the straight planar structures that appear are stacking fault planes. It is interesting to notice that the dislocation motion often occurs in two steps corresponding to the passage of the two partial dislocations. For example in c), there is a stacking fault that crosses the large central grain. It has disappeared in d). Based on the slip vector pictures, it is clear that the first partial dislocation left a grain boundary and crossed the grain, leaving a stacking fault that transverses the grain. At higher strain, the trailing partial dislocation leaves the grain boundary and removes the stacking fault plane. There is also an example of a grain being eliminated by coherent dislocation motion. Note the grain on the lower right side of the large central grain. At the end of the deformation this grain is no longer present. The slip vector plots show that there is a series of 11 parallel slip planes that go from the original location of the boundary with the central grain to the new boundary location. This indicates that the original boundary moved by the motion of the individual dislocations that comprised the boundary.

The macroscopic stress-strain curves can be evaluated from these simulations. Three different variations of the simulation were performed to examine the role of film thickness on the mechanical response. The original simulation, denoted thin, has a thickness of 100 Å. Repeating the original film before three times created a film that was about 300 Å thick that is denoted thick. Finally, a third film was created by periodically repeating the original film. This film is denoted z periodic and roughly corresponds to an infinitely thick material with columnar grains. The stress-strain curves for these three simulations are shown in Figure 5.2. It is interesting to note that the gross behavior of the stress-strain curves does not appear to depend on the thickness. In all cases there is an initial increase in stress followed by an approximate plateau at similar stress levels. The large fractional variation in the stress-strain curves is to be expected for the small sample size where individual deformation events will have a significant impact.

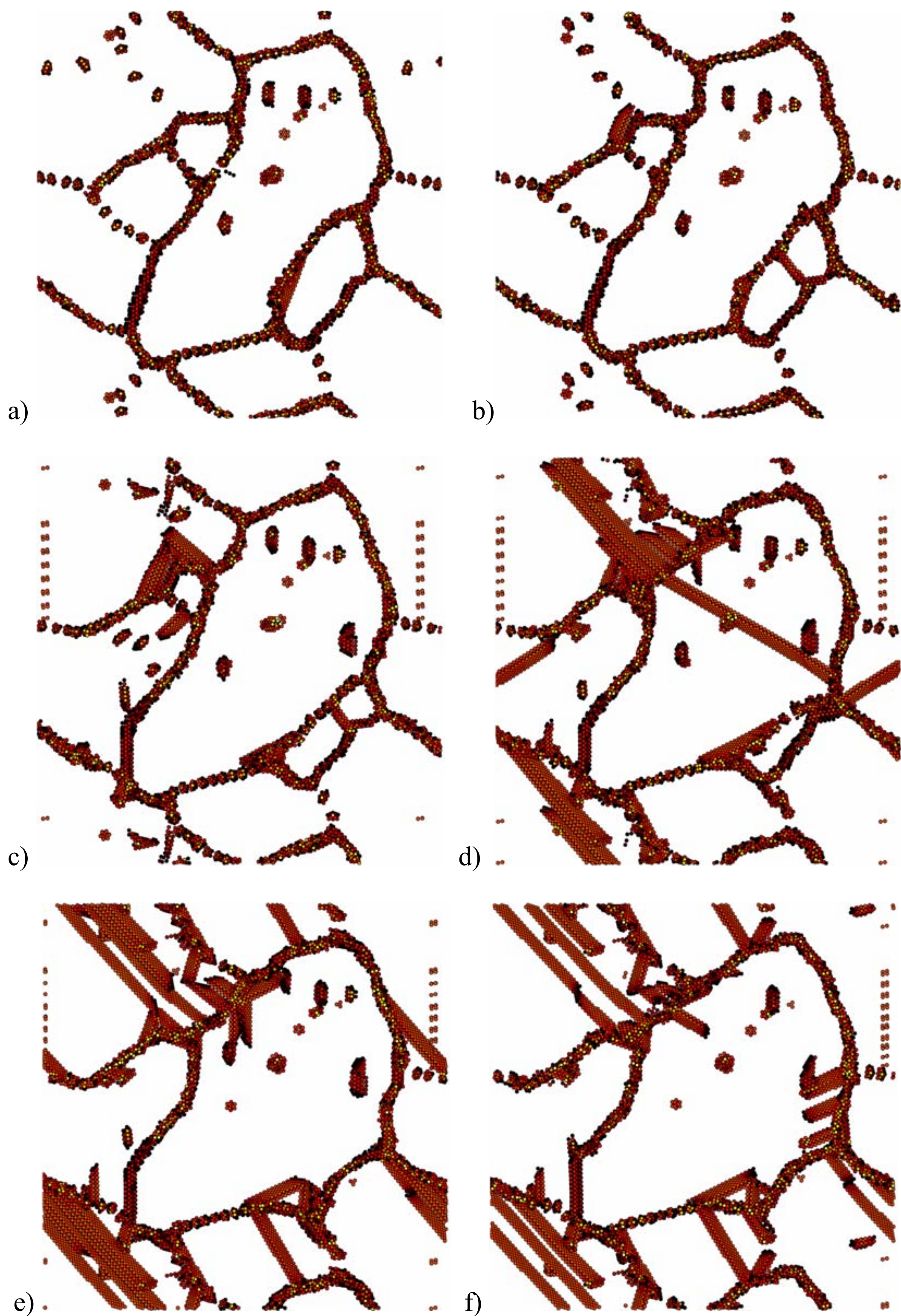

Figure 5.1 - Snapshots of the deformation of a nanograined thin film. The shading is based on the centrosymmetry parameter with atoms with small values not displayed. The cell is periodic in the plane of the film with initial dimensions of 215 x 215 Å and about 100 Å thick. The figure shows a slice of the center of the slab. The strain levels are 0 (a), 2% (b), 4% (c), 6% (d), 8% (e) and 10% (f).

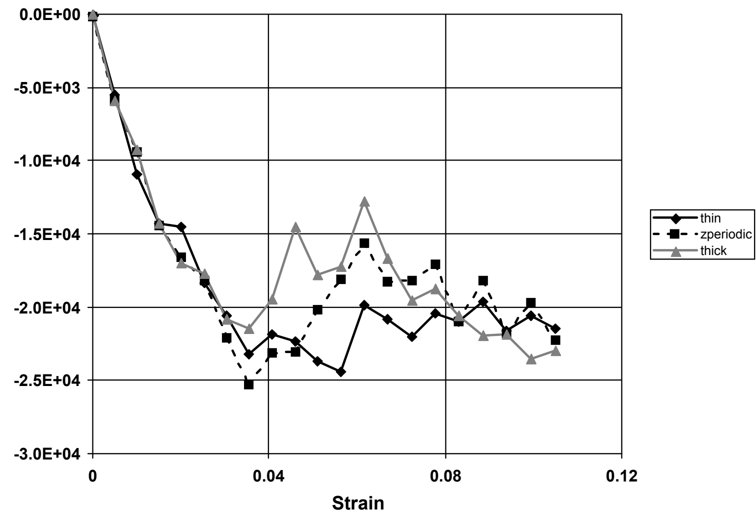

Figure 5.2 - The computed stress-strain curves for film thicknesses of 100 Å (thin), 300 Å (thick) and periodically repeated (z-periodic).

5.2 Atomistic simulations of stress in NiMn

The properties of Mn substitutional impurities in bulk Ni were computed based on first-principles density functional calculations. The calculations were performed using the Vienna Ab-Initio Simulation Package (VASP). These are plane-wave pseudopotential calculations using the density functional theory treatment of the quantum mechanics of the electrons. The exchange-correlation was treated in the generalized gradient approximation (GGA) using the Perdew-Wang'91 parametrization. The calculations were spin-polarized so that magnetic effects are included. Most of the calculations were performed for 27 atom cells. One calculation with a

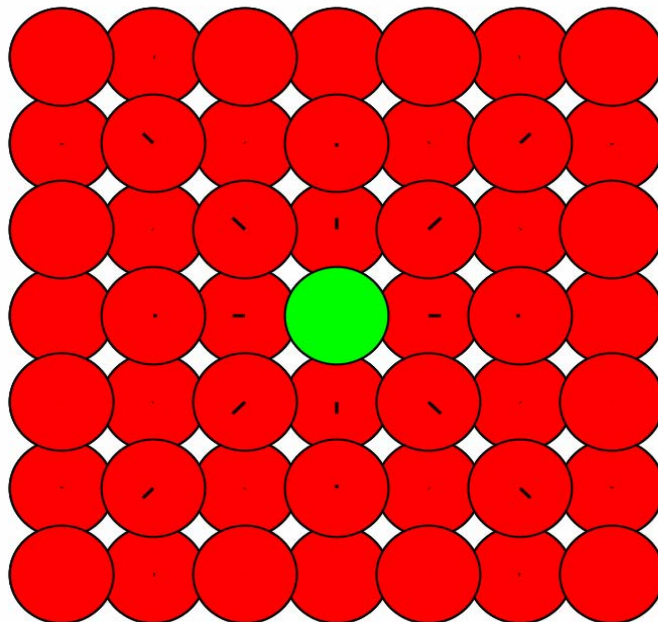

Figure 5.3 - The displacements of the atoms around the Mn substitutional atom. The lines indicate the motion of the atoms from their ideal fcc positions magnified by a factor of 20.

108 atom cell was performed to determine the atomic relaxations in the vicinity of the impurity.

The energy versus value was determined for the 27 atom cell both with and without a Mn substitutional impurity in Ni. From the difference in the equilibrium volume of the two cells, the excess volume associated with an Mn substitutional impurity is determined to be $\Delta V = 1.4$ Å^3. This value is consistent with simple estimates based on the volume per atom of elemental Ni in the fcc structure and Mn in the A12 structure. This simple estimate yields a volume difference of 1.25 Å^3.

The effect of Mn substitutional impurities on the elastic constants was also determined. The bulk modulus for the 27 atom cells is determined from the curvature of the energy versus volume

curve at equilibrium. The shear moduli are determined by applying uniform strains to the cells that correspond to the C_{44} and C' = $(C_{11} - C_{12})/2$. The curvature of the energy versus strain then yields the shear modulus. For the case of pure Ni, these calculations yield B = 2.02 Mbar, C_{44} = 1.25 Mbar and C' = 0.59 Mbar. The corresponding experimental values are 1.80, 1.25 and 0.50 Mbar, respectively. This level of agreement is typical for density functional calculations of elastic constants. From the elastic constants deduced for the cell containing a Mn impurity, the rate of change of the elastic constants with composition can be determined. These calculations yield $\frac{\partial B}{\partial c} = -0.82 Mbar$, $\frac{\partial C_{44}}{\partial c} = -0.35 Mbar$, and $\frac{\partial C'}{\partial c} = 0.15 Mbar$. This indicates that the addition of Mn substitutionals will lead to a modest softening.

In order to address the variation in bond lengths introduced by a Mn substitutional atom, a 108 atom cell was considered. In this calculation both the cell volume and the atomic positions were optimized. Figure 5.3 shows the displacements of the atoms around the Mn substitutional atom. The lines indicate the motion of the atoms from their ideal fcc positions magnified by a factor of 20. It is seen that the main effect of the Mn substitutional is to move the surrounding Ni atoms away from the Mn atom. The Ni-Mn nearest neighbor distance was computed as 2.518 Å compared to the computed nearest neighbor distance in pure Ni of 2.494 Å. The distribution of nearest neighbor distances in the 108 atom cell is shown in Figure 5.4. The distances just under 2.52 Å result from the Ni-Mn pairs as well as pairs of Ni atoms in the first neighbor shell of the Mn. For the average lattice constant of this cell, the nearest neighbor distance should be 2.498 Å. Thus these results show that there is a distribution of nearest neighbor distances around this value, which is consistent with the x-ray diffraction measurements of the lattice parameter of NiMn.

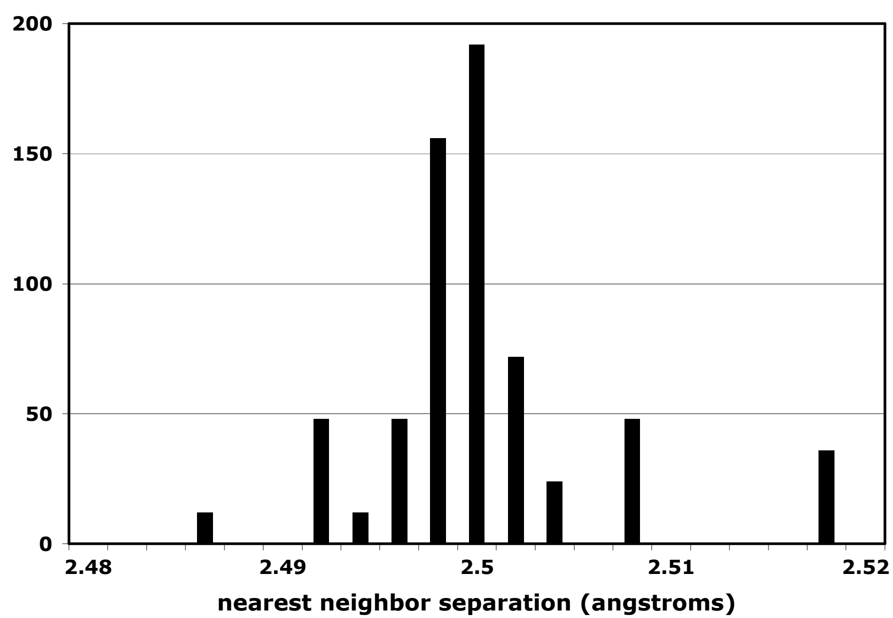

Figure 5.4 - Distribution of nearest neighbor distances in the 108 atom cell.

5.3 References for section 5

[1] C.L. Kelchner, S.J. Plimpton, and J.C. Hamilton, Phys. Rev. B58, 11085 (1998).

[2] J.A. Zimmerman, C. L. Kelchner, P.A. Klein, J.C. Hamilton and S.M. Foiles, Phys. Rev. Lett. 87 (2001).

6. CONCLUSIONS

We have successfully developed multiple MEMS based devices that were used to measure the stress-strain and fatigue properties of AlCu thin films. Based on this work, FE models were developed to elucidate the mechanical response of the system. Using a wafer curvature based stress sensor we directly measured the stress created during island coalescence and found that the Friend-Chason model accounted for the initial coalescence stress. However, the majority of the coalescence stress was the result of the post-initial contact of the islands. Additionally, we used this system to explore the fundamental sources of stress active during electrodeposition of Ni and NiMn. It was determined that in both systems there were multiple mechanisms (one tensile and one compressive) actively creating stress that were functions of the deposition rate. The tensile stress mechanism was concluded to be continual coalescence of grains, where as the compressive mechanism was not conclusively identified. Atomistic molecular dynamics simulations were used to understand the mechanical response under deformation of the thin film nanoscale materials studied experimentally. It was determined that the gross behavior of the stress-strain curves did not depend on the thickness, when multiple grains through the thickness of the films were present. Finally, atomistic simulations of the incorporation of Mn into a Ni lattice confirmed the x-ray diffraction observed increase in micro-strain along with a slight increase in the mean lattice parameter.

7. APPENDIX

7.1 Appendix A

The two-dimensional thermoelastic stress-strain relationships for an isotropic material in plane stress are given by

$$\begin{bmatrix} \sigma_x \\ \sigma_y \\ \tau_{xy} \end{bmatrix} = \begin{bmatrix} Q_{11} & Q_{12} & 0 \\ Q_{12} & Q_{11} & 0 \\ 0 & 0 & Q_{66} \end{bmatrix} \begin{bmatrix} \varepsilon_x - \alpha\Delta T \\ \varepsilon_y - \alpha\Delta T \\ \gamma_{xy} \end{bmatrix} \tag{A1}$$

where Q represents the reduced stiffness matrix for the plane stress case, α is the coefficient of thermal expansion, and ΔT is the temperature difference. The individual components of the stiffness matrix Q can be expressed in terms of material properties as shown by

$$Q_{11} = \frac{E}{1-\nu^2} \qquad Q_{12} = \frac{\nu E}{1-\nu^2} \qquad Q_{66} = \frac{E}{2(1+\nu)} \tag{A2}$$

where E is Young's modulus and ν is Poisson's ratio. We now obtain an expression for σ_x by substituting the reduced stiffness components from Eq. (A2) into the stress-strain relationships in Eq. (A1)

$$\sigma_x = \frac{F}{wt} = \frac{E}{1-\nu^2}\left(\varepsilon_x + \nu\varepsilon_y - (1+\upsilon)\alpha\Delta T\right) \tag{A3}$$

where F is the axial force applied to the plate, w is the width, and t is the thickness. To find the stiffness ratio SR, we evaluate Eq. (A3) for the plate (w=W_{max} and F=F_{plate}) and the notched structure (w=W_{min} and F=F_{notch}) and take the ratio of the two expressions using SR=F_{notch}/F_{plate}

$$\left(\varepsilon_x + \nu\varepsilon_y - (1+\upsilon)\alpha\Delta T\right)_{notch} = (SR)WR\left(\varepsilon_x + \nu\varepsilon_y - (1+\upsilon)\alpha\Delta T\right)_{plate} \tag{A4}$$

where WR= W_{max}/W_{min} is the width ratio. This expression can be further simplified using ε_{gage}=$(\varepsilon_x+\nu\varepsilon_y-(1+\nu)\alpha\Delta T)_{notch}$ and ε_R=$(\varepsilon_x+\nu\varepsilon_y-(1+\nu)\alpha\Delta T)_{plate}$ to

$$\overline{\varepsilon_{gage}} = (SR)WR\varepsilon_R \tag{A5}$$

which is equivalent to Eq. (2.1) in the main text.

7.2 Appendix B - Progress toward tuning the residual stress

As seen in Fig. A1, the sputter deposition of the Al/0.5% Cu film can be tuned to deliver a stress near 0 MPa. This was accomplished by keeping the chuck below room temperature and waiting for 10 minutes between depositions to assure any heating of the chuck had subsided. This experiment was done because the analysis of Part I suggests that Device 1 will display a very

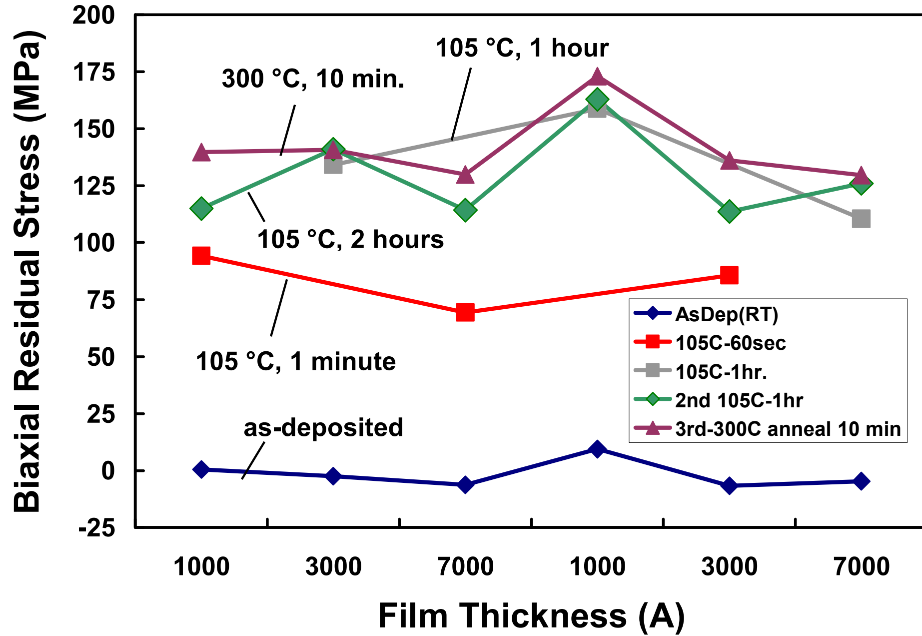

Figure A1 - Biaxial residual stress as a function of temperature and subsequent annealing. After a photolith bake (105 °C, 60 seconds), the residual stress increases from 0 to 70 MPa (biaxial).

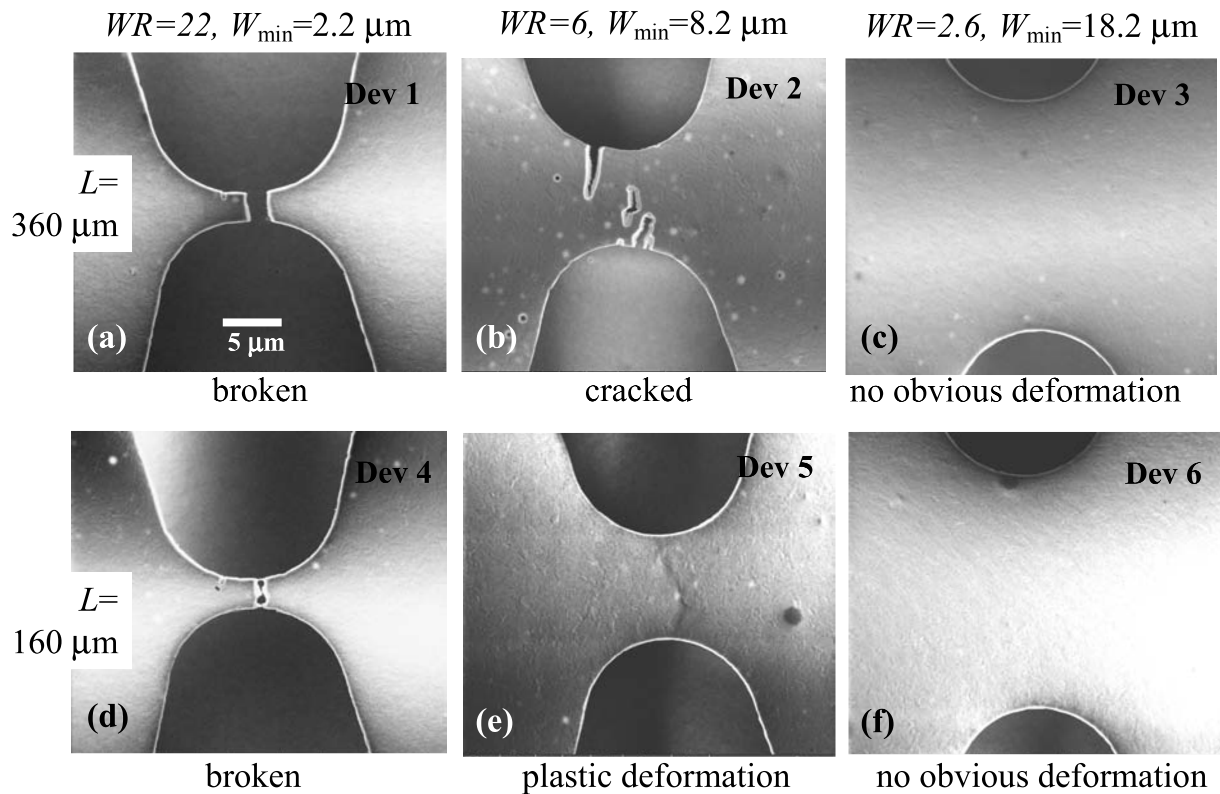

Figure A2 - Deformation due to residual stress only (SEM images). Here, σ_R =50 MPa. In these images, the fixed ends of the notched structures are on the left and the right.

wide useful range if the residual stress can be kept low. In fact, Fig.A1 shows that the as-deposited stress is near 0 MPa, independent of thickness and reproducible over two attempts. However, a one minute anneal at 105 °C, which is the thermal cycle required to bake the photoresist, increased the biaxial stress from 0 to 80 MPa independent of film thickness. Multiplying by (1- υ), the uniaxial value is 54 MPa. To avoid this significant change in σ_R, a liftoff technique could be used to define the Al/0.5% Cu film in future efforts. It should be noted that even when it is difficult to obtain zero residual stress, other devices besides the narrowest remain useful for obtaining mechanical properties.

7.3 Appendix C - Actuation of cracked structures

Upon release in some areas, Devices 1 & 4 (with WR=22) were completely separated, while those Devices 2 & 5 (with WR=5.9) showed severe damage. Figs. A2(a)-(c) and Figs. A2(d)-(f) show SEM top views of the notched structure damage for Devices 1-6. On fixed-fixed beams adjacent to the notched structures in Fig. A2, σ_R was 51 MPa. These samples were checked before release but after etching, and no cracking was observed. At that time, the film is still in the biaxial stress state because it is well adhered to the underlying oxide. During the release, the underlying oxide is removed and hence the stress redistributes and concentrates in the notched region. Therefore, cracking occurred while the devices were being released. For the same WR, the damage is greater when L=360 μm than when L=160 μm. For example, the separation is greater in Fig. A2(a) than in Fig. A2(d). In Fig. A2(b) there is cracking while in Fig. A2(e) there appears to be plastic deformation. This greater damage can be attributed to the larger strain energy in the notched structures for L=360 μm compared to L=160 μm.

Structures with pre-existing cracks such as in Fig. A2(b) were actuated and exhibited strong hysteresis, as shown in Fig. A3. Fig. A3(a) shows the full deflection curves, where the solid lines are upon loading and the dotted lines are during unloading. The apparent noise at x=180 μm is due to the obvious difficulty in gaining valid interferometry data across a crack or a rapid change in step height. The remaining deflection data is valid. It is clear from the data that unloading curves show more deflection than loading curves. A more subtle point is that at 0 V, these structures are slightly buckled, and the buckling increases after loading at a given voltage.

In Fig. A3(b), the maximum deflection of a given curve is plotted versus loading and unloading voltage. For these pre-cracked structures, the loading curves depended strongly on the previous loading history. The difference in loading versus unloading curve is shown in Fig. A3(c), which has a characteristic shape that we routinely observed. The hysteresis for these samples was much larger than those in the Section IV of the main body, where the gage section was plastically deformed, but not cracked. Beginning near the maximum voltage, the deflection difference is zero. As V_a decreases, the difference is negative and tends to become more negative. Then as V_a approaches zero, the difference tends towards zero and even becomes positive. We interpret this data as follows. As the sample is loaded, there is enhanced gage section stretching due to crack extension each time V_a is incremented. As V_a is decreased from its maximum value, the cumulative stretching is larger the more that V_a decreases. This explains why the difference curve first decreases as V_a is lowered. For a small enough value of V_a, the bending stiffness

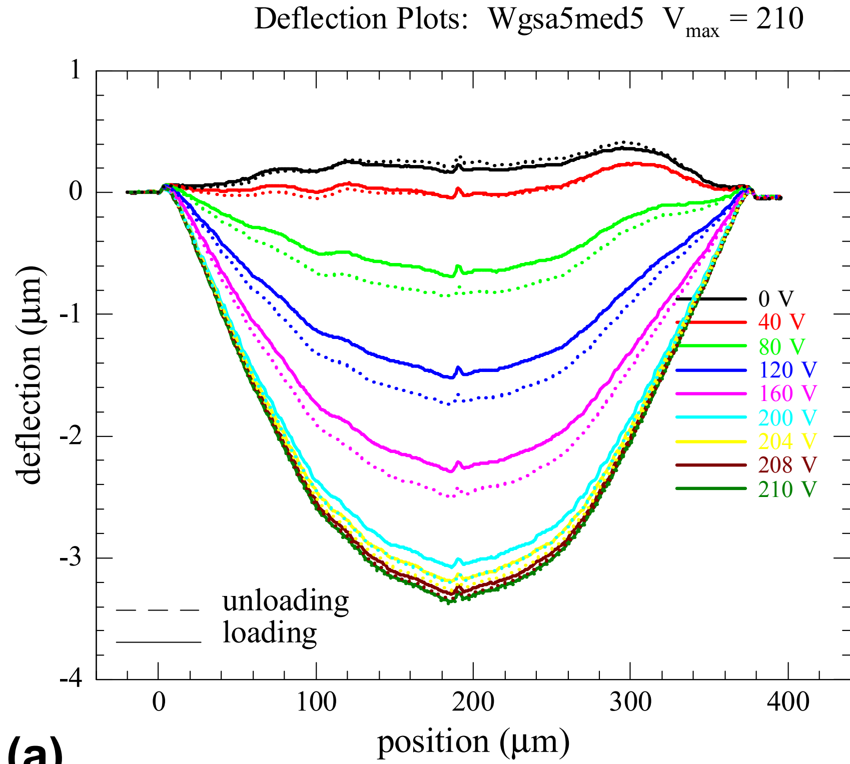

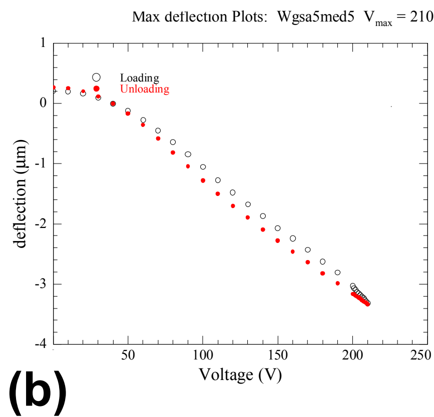

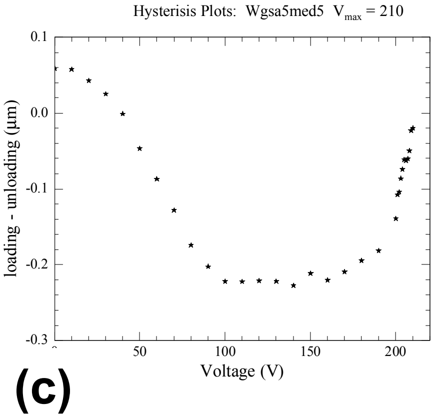

Figure A3 - Partly fractured devices exhibit large hysteresis σ_R=50 MPa, L=360 μm, WR=6 μm. (a) Full deflection curves. (b) Maximum deflection upon loading and unloading. (c) Difference plot in unloading versus loading.

more strongly affects the deflection curve than does the tension in the beam. Therefore, the difference tends toward zero. The fact that the difference becomes positive must be because there is net compression in the structure (after severe stretching, amplitudes as large as 2 μm were observed). This is because the material around the crack tip acts as a hinge that can no longer fully close.

DISTRIBUTION

5	MS1415	Sean Hearne	01112
5	MS1310	Maartin de Boar	01769
1	MS9161	D. Dibble	08761
1	MS9403	N. Yang	08773
1	MS9409	S. Goods	08754
1	MS9401	M. Losey	08753
1	MS1415	D. Peebles	01112
1	MS1415	C. Barbour	01110
1	MS1427	J. Phillips	01100
1	MS0889	B. L. Boyce	01851
1	MS1415	J. Floro	01114
1	MS1415	S. Seel	01114
2	MS9018	Central Technical Files	8945-1
2	MS0899	Technical Library	4536
2	MS0123	D. Chavez, LDRD Office	1011

Sandia National Laboratories